Kristoffer Johansen

Comparative characterization of biotechnologically modified xanthan

Master's thesis in MSBIOTECH
Supervisor: Dr. Gaston Courtade
Co-supervisor: Prof. Bjørn E. Christensen
May 2023

◻ NTNU
Norwegian University of
Science and Technology

Kristoffer Johansen

Comparative characterization of biotechnologically modified xanthan

NTNU
Norwegian University of
Science and Technology

ABSTRACT

Xanthan is a versatile bacterial extracellular polysaccharide (EPS) that is widely used in various industries for its unique physical properties. New applications of xanthan will be made possible by controlling its properties, but chemical or enzymatical modification could lead to costly downstream processing. Thus, biotechnological tailoring of xanthan properties could be the solution. To achieve sufficient control, it is necessary to confirm how modifications influence the properties of the biopolymer.

In this thesis, xanthan material from different gene-knockout mutants of *Xanthomonas campestris spp.* was produced by fermentation, mechanically degraded, and characterized using SEC-MALS and NMR spectroscopy. This was done to gain more knowledge about biotechnologically modified xanthan material, investigate how the chemical composition of the side chain affects its properties and simultaneously evaluate the use of these techniques for characterization of biotechnologically modified xanthan.

The results from the fermentation showed that there were variations in yield and acetate- and pyruvate content compared to the wild type. The variations in yield indicated either reduced xanthan production or an altered low M_w repeating unit (RU) composition in the mutant strains compared to the wild type. The variations in acetate- and pyruvate content were explained by either increased or reduced competition on the β-mannose or variations in RU composition.

SEC-MALS analysis showed that 10 cycles of mechanical degradation by Wet Mill Jet Star Burst Mini homogenizer consistently decreased the weight average molecular weight (M_w) from approx. 3500-6700 kDa (at 0 cycles) to approx. 280-610 kDa (after 10 cycles).

Using 1H-NMR, the temperature of the order-disorder transition midpoint or melting temperature (T_m) was estimated and was found to be influenced by the acetate and pyruvate content. It was concluded that 1H-NMR was a useful tool to probe the stability of different xanthan variants given that the T_m was below the boiling temperature of D_2O.

2D-NMR was used to assign the T_m reporters, and to partially assign the rest of the xanthan spectrum of the wild type. Three complete monosaccharide residues were assigned: the non-substituted α- and β-mannose and the pyruvylated β-mannose. The H6-C6 peaks of the acetylated α- and β-mannose and glucose residue were also identified and assigned. In addition to this, six peaks were identified as either glucose or glucuronic acid residues. Based on the results it was concluded that using NMR spectroscopy and biotechnologically modified variants of xanthan was a feasible strategy for improving the existing NMR assignments of wild type xanthan.

Overall, this thesis showed some of the potential and limitations of using biotechnological tools to gain more knowledge of how modifications influence the properties of polymers such as xanthan.

SAMMENDRAG

Xanthan er et allsidig bakterielt ekstracellulært polysakkarid (EPS) som brukes i mange ulike bransjer på grunn av sine unike fysiske egenskaper. Modifisering av egenskapene til xanthan kan føre til nye bruksområder av materialet, men kjemisk eller enzymatisk modifisering kan føre til kostbar nedstrøms prosessering. Dette kan unngås med bruk av bioteknologiske verktøy, men for å oppnå tilstrekkelig kontroll, trenger man metoder for å bekrefte hvordan modifikasjonene som er utført påvirker egenskapene til biopolymeret.

I denne avhandlingen ble xanthanmateriale fra forskjellige *Xanthomonas campestris spp.* knockout-mutanter produsert ved fermentering. Xanthanmaterialet ble mekanisk degradert før det ble karakterisert ved hjelp av SEC-MALS og NMR-spektroskopi. Dette ble gjort for å få mer kunnskap om bioteknologisk modifisert xanthanmateriale, undersøke hvordan den kjemiske sammensetningen av sidekjeden påvirker egenskapene og samtidig evaluere bruken av disse teknikkene for karakterisering av bioteknologisk modifisert xanthan.

Resultatene fra fermenteringen viste at det var variasjoner i utbytte og innhold av acetat og pyruvat sammenlignet med villtypen. Variasjonene i utbytte indikerte enten redusert xanthanproduksjon eller en repeterende enhet (RU)-sammensetning med lavere vektgjennomsnittlig molekylvekt (M_w) i mutantstammene sammenlignet med villtypen. Variasjonene i innholdet av acetat og pyruvat ble forklart enten ved økt eller redusert konkurranse på β-mannosen eller variasjoner i RU-sammensetning.

SEC-MALS-analyse viste at 10 sykluser med mekanisk nedbrytning i en Wet Mill Jet Star Burst Mini homogenisator konsekvent reduserte M_w fra ca. 3500-6700 kDa (ved 0 sykluser) til ca. 280-610 kDa (etter 10 sykluser).

Ved hjelp av 1H-NMR ble temperaturen for midtpunktet for orden-uordenovergangen eller smeltetemperaturen (T_m) estimert og ble funnet å bli påvirket av innholdet av acetat og pyruvat. Det ble konkludert med at 1H-NMR var et nyttig verktøy for å undersøke stabiliteten til forskjellige xanthanvarianter gitt at smeltepunktet var under kokepunktet til D_2O. 2D-NMR ble brukt til å identifisere T_m-reportere og delvis identifisere resten av xanthan-spekteret til villtypen. Tre komplette monosakkariddeler ble identifisert: den ikke-substituerte α- og β-mannosen og den pyruvylerte β-mannosen. H6-C6-topper av acetylert α- og β-mannose og glukose ble også identifisert. I tillegg ble seks topper identifisert som enten glukose eller glukuronsyre-rester. Basert på resultatene ble det foreslått at bruk av moderne NMR-spektroskopi og bioteknologisk modifiserte varianter av xanthan var en potensiell strategi for å forbedre de eksisterende oversiktene av kjemiske skift i NMR av villtypexanthan.

Alt i alt viser denne oppgaven noe av potensialet og begrensningene ved å bruke bioteknologiske verktøy til å få mer kunnskap om hvordan modifikasjoner påvirker egenskapene til polymerer som xanthan.

PREFACE

The work described in this master's thesis was carried out at the Department of Biotechnology and Food Science at the Faculty of Natural Sciences at the Norwegian University of Science and Technology (NTNU) and the research laboratory of Prof. Dr. -Ing. Jochen Schmid at the University of Münster.

I would like to express my gratitude to my supervisor Dr. Gaston Courtade for providing me great support throughout the project. Thank you for giving me the opportunity to study the interesting topic of polysaccharide engineering and for being such a good role model for me and all biotechnology students at NTNU. Your dedication and love for science have been highly motivating and shown me what an honest, kind, and hard-working academic should look like. Also great thanks to my co-supervisor Prof. Bjørn E. Christensen for providing guidance and interesting insight to the project.

I would also like to express sincere thanks to the research group Biopolymers and biomaterials at NTNU and the members of the Courtade Lab for interesting and informative group meetings and presentations. Thanks to Dr. Olav Andreas Aarstad for providing me guidance and supervision with SEC-MALS.

Special thanks to Prof. Dr. Ing.- Jochen Schmid and Dr. Moritz Gansbiller for welcoming me and providing guidance with my experiments at the University of Münster.

Thanks to Asle Hammer Berget and Alexander Mika Hannasvik for helping with interpreting my NMR-results and for all the sparring meetings. Huge thanks to my classmates of MSBIOTECH 2021/23 for showing me that master is lættis.

Finally, I wish to thank my partner Lena Døsvik for doing all the housekeeping the last months.

CONTENTS

LIST OF SYMBOLS AND ABBREVIATIONS

^{13}C	Carbon 13
^{1}H	Protium
A.C	Active Carbon
A_2	Second virial coefficient
AFM	Atomic Force Microscope
AM	α-Mannose
AMA	α-Mannose Acetylated
AMNS	α-Mannose Non-Substituted
B0	External magnetic field
BM	β-Mannose
BMA	β-Mannose Acetylated
BMNS	β-Mannose Non-Substituted
BMP	β-Mannose Pyruvylated
COSY	COrrelation SpectroscopY
dn/dc	Differential refractive index increment
dRI	Differential refractive index
DS	Degree of Substitution
EDTA	EthyleneDiamineTetraacetic Acid
EPS	Extracellular PolySaccharide
FDA	Food and Drug Administration
G/GA	Glucose or Glucuronic Acid
Glc	D-Glucose
GlcA	D-Glucuronic Acid
h	Planck's constant
HMBC	Heteronuclear Multiple Bond Correlations
HSQC	Heteronuclear Single Quantum Coherence
Hz	Hertz
I_0	Intensity of the incident radiation
I_{max}	Fitted parameters describing the top of the sigmoidal curve
I_{min}	Fitted parameters describing the bottom of the sigmoidal curve
I_θ	Scattered light intensity of the solution
$I_{\theta,solvent}$	Scattered light intensity of the solvent
J	Coupling constant
K^*	Optical constant
M	Molar mass
M_{ac}	Molecular weight of an acetate
Man	D-Mannose
M_i	Molecular weight of i
M_n	Number-average molecular weight
M_{pyr}	Molecular weight of a pyruvate
M_{RU}	Molecular weight of a repeating unit
M_w	Weight-average molecular weight
MQ	MilliQ water

N_A	Avogadro's number
N_i	Number of units i
NMR	Nuclear Magnetic Resonance
n_o^2	Refractive index of the sample solvent
NOESY	Nuclear Overhauser Effect SpectroscopY
pK_a	Acid dissociation constant
R_G	Radius of Gyration
$R_{G,z}$	Z-average Radius of Gyration
RT	Room Temperature
RU	Repeating Unit
R_θ	Rayleigh ratio
SEC-MALS	Size Exclusion Chromatography – Multi Angle Light Scattering
SLS	Static Light Scattering
T_m	Melting Temperature (i.e., temperature of the order-disorder transition midpoint)
TOCSY	TOtal Correlated SpectroscopY
UDP	Uridine DiPhosphate
V_θ	Detector signal voltages of the solution
$V_{\theta,laser}$	Detector signal voltages of the laser
$V_{\theta, solvent}$	Detector signal voltages of the solvent
WS	Wild type strain
WTAC	Wild Type Active Carbon
WTS	Wild Type Standard
X. campestris	*Xanthomonas campestris*
γ	Gyromagnetic ratio
μ	Magnetic moment
I	Spin quantum number
$P(\theta)$	Particle scattering function
δE	The energy difference between two states

1 INTRODUCTION

1.1 Xanthan

Xanthan is a versatile bacterial extracellular polysaccharide (EPS) that is widely used in various industries for its unique physical properties. After its recognition as a potentially useful material in the 1950s and early 1960s, xanthan was approved as a food additive by the Food and Drug Administration (FDA) in 1969. It has since been found in many food products like dairy, bakery goods and beverages as a thickener or stabilizer. Xanthan gum has also been used in non-food applications such as oil drilling fluids, cosmetics, personal care products, pharmaceuticals, and biotechnology. In oil drilling fluids, xanthan can improve the suspension of solids, reduce friction losses, and withstand high temperatures and salinities. In cosmetics and personal care products, xanthan can provide moisturization, emulsification, and rheology modification. In pharmaceuticals and biotechnology, xanthan can be used as a drug delivery vehicle, a tissue engineering scaffold, a bio-adhesive agent, and a biofilm inhibitor. (Chaturvedi et al., 2021, Christensen, 2021)

It is produced by the fermentation of *Xanthomonas* spp. where *X. campestris* is the most commonly used species in industrial production (Petri, 2015). As a plant-pathogenic bacterium, *X. campestris* forms biofilms on the surfaces of plants (Guerra et al., 2018). The biofilm it produces is composed of an extracellular matrix that contains xanthan and other polysaccharides, which help the bacteria adhere to the host and resist environmental stresses and antimicrobial agents (Sena-Vélez et al., 2015).

1.2 Chemical properties and synthesis

The chemical structure of the polysaccharide is composed of a repeating saccharide pentamer (Figure 1-1). This repeating unit (RU) consist of two D-glucose residues (Glc), two D-mannose residues (Man) and one D-glucuronic acid residue (GlcA). The two Glc residues are β-(1,4)-linked creating a cellobiose backbone that is connected to a trimeric side chain of Man and GlcA. The innermost residue of the side chain is a α-D-Mannose attached through a β-(1,3)-link to the backbone, followed by the GlcA via an α-(1,2)-link. The last β-Man residue is attached to the GlcA through a β-(1,4)-link. The α-Man can be O-6 acetylated (hereby called "internal acetylation"), while the β-Man can have either an O-6 acetylation (hereby called "terminal acetylation") or a O-6/O-4 pyruvate diketal linkage. The degree of substitution varies depending on several factors like fermentation conditions and what *Xanthomonas* strain is used for production. (Flores Candia and Deckwer, 1999, Peters et al., 1993, Sutherland, 1981)

Xanthan is commonly recognized as existing in an ordered double helix structure in solutions of a sufficient concentration of counterions. This ordered double helix structure is polyanionic for a large pH interval, which enables many of the applications and properties of xanthan. Solutions of xanthan are highly viscous at low concentrations and are stable at a large pH and ionic strength interval. The viscosity is a result of its high molecular weight, while its ordered structure and polyelectrolyte properties contribute to the stability of xanthan. The double helix conformation improves the polysaccharide's resilience against changes in ionic strength and makes it stiff, with a persistence length of 120 nm. Due to this stiffness, low molecular weight xanthan can behave like rigid rods. (Christensen, 2021)

The variations in degree of substitution lead to there being six variations of the RU, with different molecular weights. The molecular weight contribution of a pyruvate is M_{pyr} = 87.05 Da (National Center for Biotechnology Information, 2023b) while the acetate is M_{ac} = 59.04 Da (National Center for Biotechnology Information, 2023a). This causes the theoretical average M_{RU} to be somewhere between 848 Da and 994 Da (Christensen, 2021). Since the pyruvate has a carboxyl group, its presence will affect the pK_a of the RU as well. The RU usually has a net negative charge above pH 4.6, making it an anionic polyelectrolyte in aqueous solutions at both high and moderate pH. (Kool et al., 2014)
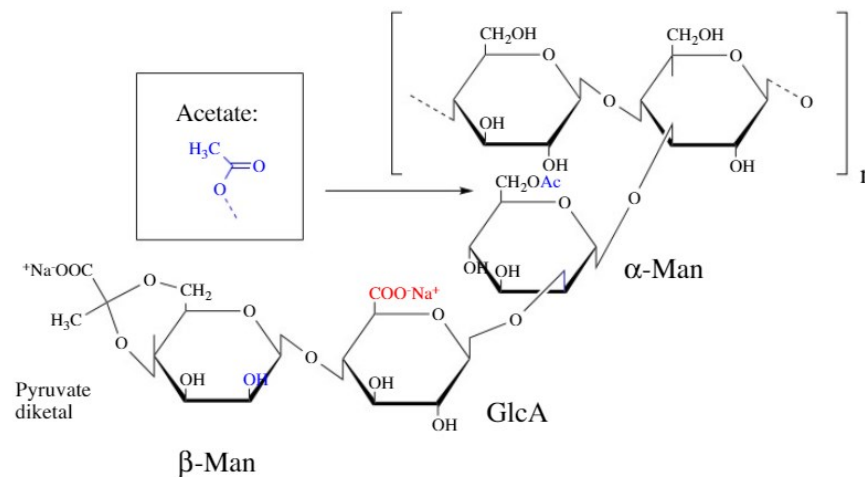

Figure 1-1 The chemical structure of one of the possible repeating units (RU) of xanthan where the terminal mannose (β-mannose) is pyruvylated. This RU consists of two D-glucose residues (Glc), two D-mannose residues (Man), and one D-glucuronic acid residue (GlcA). The two Glc residues are linked together in a β-(1,4) configuration to form a cellobiose backbone that is connected to a trimeric side chain of Man and GlcA. The innermost residue of the side chain is an α-D-Mannose attached through a β-(1,3) linkage to the backbone, followed by the GlcA via an α-(1,2) linkage. The last β-Man residue is attached to the GlcA through a β-(1,4) linkage. The α-Man of this specific RU is O-6 acetylated while the β-Man an O-6/O-4 pyruvate diketal linkage.

The biosynthesis of xanthan is similar to the general process of EPS biosynthesis where the process is comprised of multiple syntheses and assembly processes. Firstly, the sugar nucleotide precursors are synthesized to make oligosaccharides that are finally assembled and exported as the polysaccharide. In biosynthesis of xanthan, the sugar nucleotide precursors UDP-mannose, UDP-glucose, and UDP-glucuronic acid are assembled into RUs in the cytoplasmic face. In addition to the assembly of the saccharides, non-carbohydrate residues such as pyruvate and acetate may be attached to the mannose residues before it is exported as mature RUs. The mature RU is then transported into the periplasmic face where it is polymerized into polysaccharides similar to the WZY-synthesis found in Enterobacteriaceae. (Rashidi et al., 2023, Vorhölter et al., 2008) An overview of this process is presented in Figure 1-2.
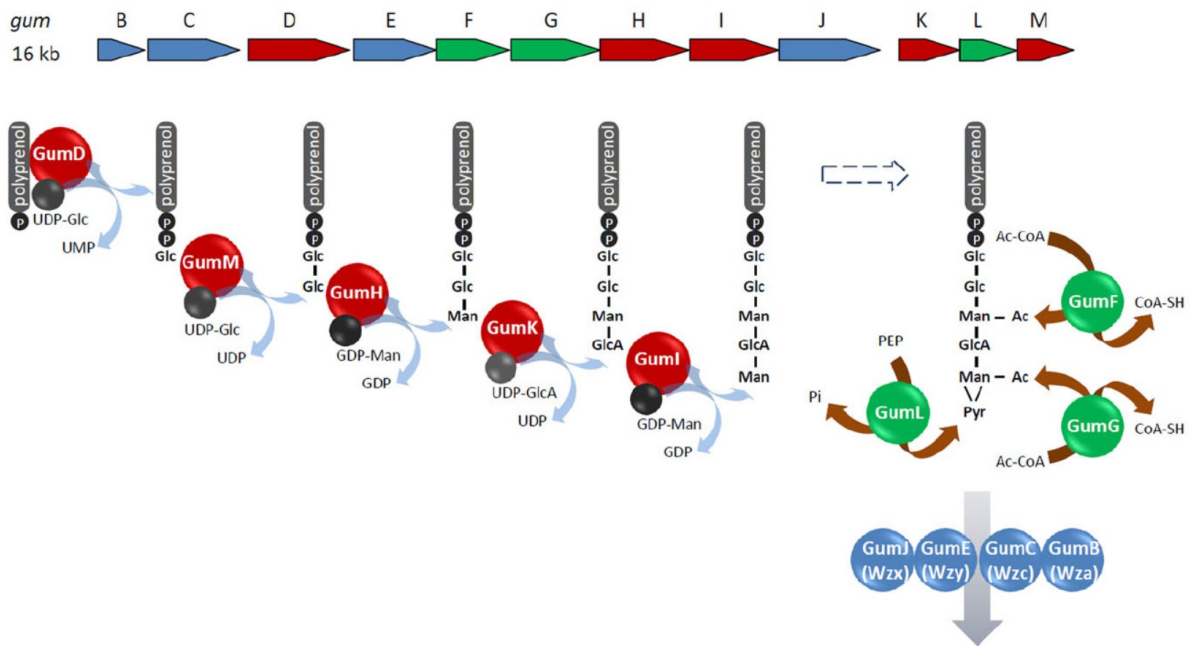
Figure 1-2 Biosynthesis of xanthan retrieved from a review article by Anke Becker (Becker, 2015). The gum cluster is shown on top, with each gene represented by a letter from B to M. The corresponding enzymes are shown as spheres (red: glycosyltransferases, green: acetyltransferases or pyruvate ketalase, blue: flippase/polymerase). The reactions catalyzed by each enzyme are shown.

The *gum* gene cluster, which consists of 12 genes (gumB-gumM), is responsible for encoding the enzymes that catalyze xanthan biosynthesis: the assembly of the RUs and polymerization. The *gum* gene cluster is highly conserved among different xanthan-producing bacteria and is regulated by various environmental factors (Lee et al., 2005). The genes *gum*D, -H, -I, -K and -M are involved in assembling the saccharide units, while *gum*B, -C, -E and -J code for enzymes that polymerize and export the polysaccharide. The remaining genes in the gene cluster are responsible for attaching the non-carbohydrate residues to mannose units. Amongst the three remaining genes, *gum*F and -G produce the acetyltransferases GumF and GumG, while *gum*L produces the pyruvate ketalase GumL. The α-D-mannose is acetylated by GumF and the β-D-mannose is acetylated by GumG and pyruvylated by GumL. (Becker et al., 1998)

By producing *X. campestris* mutants lacking either GumF, -G or -L or mutants where a combination of the three are deleted, it is possible to create xanthan with specific acetylation and pyruvylation patterns (Gansbiller et al., 2019). This has opened new ways of investigating the native structure and composition of xanthan. For example, until now, only limited NMR-assignments of native xanthan have been published due to the complexity of the wild-type structure. Using multiple variants of xanthan with defined substitution patterns could help elucidate the structural composition.

1.3 Order-disorder transition

The native form of xanthan was debated for many years as it appeared to be either a single or double helix while some argued it could be both. Edwin R. Morris wrote an article in 2019 reviewing this controversy. Although his work needs recognition, he reviewed and compared the research done by many other great biopolymer researchers who are acknowledged in the article. This section will use said article to explain the debate and other resources to explain the order-disorder transition of xanthan.

Years of contradicting results simultaneously proved that xanthan could be either a single helix or a double helix. After high resolution atomic force microscope (AFM) imagery was analyzed, the debate was somewhat settled as the imagery showed both the unwinding of a double helix and the formation of hairpin loops at the ends of ordered regions. This confirmed that, at least, xanthan was an ordered double helix in solutions containing sufficient concentrations of counterions. However, this contradicted previous research that had proved the existence of the single helix. Edwin R. Morris proposed an explanation that he suggested allowed for both phenomena to be true. His explanation consisted of a two-step process where disordered strands formed single intramolecular helices before a dimerization of single helices form 5_1 anti-parallel double helices. (Morris, 2019)
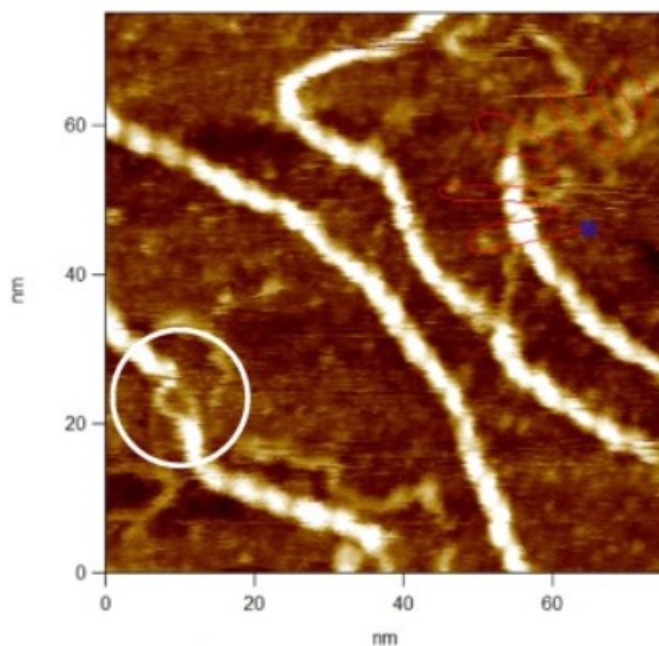
Figure 1-3 AFM image of xanthan recorded by (Moffat et al., 2016). The white circle shows the disassociation of the ordered structure into two distinctive strands. There is also evidence of separation of the double stranded structure into two strands in the top right-hand corner of the image. Moffat et al. (2016) also produced images of hairpin loops.

Xanthan can undergo a conformational change where the double helix dissociates at certain temperatures (Morris, 2019). This is dependent on the molecular weight, solvent conditions, and degree of substitution (Lee and Brant, 2002). The temperature-induced conformational change can be measured in many ways including viscometry, light scattering, and NMR spectroscopy. It is generally accepted that the dimeric double helix denatures into single stranded coils under the order-disorder transition, which changes its rheology and applications. During de- and renaturation, the transition follows a sigmoidal curve which can be used to estimate the transition mid-point or the melting temperature, T_m. Xanthan seems to have a thermal memory after an order-disorder transition and

forms a new ordered conformation including new multimeric clusters after renaturing. This makes the first transition of a native sample non-reversible. However, renatured xanthan seem to have a semi-reversible order-disorder transition. (Washington and Brant, 2021)

The melting curves of the different xanthan types are heavily influenced by their substitution patterns due to the side chains contribution to the stability of the ordered conformation. It is generally thought that pyruvylation destabilizes, while acetylation stabilizes the ordered conformation. Studies on the subject traditionally have been made on chemically modified variants and can therefore not relate the effect of deacetylation to the position of the acetyl (internal or terminal). Studies using genome editing tools to control the substitution pattern have shown that for dilute solutions the position of the acetyl, which was used as an indication of the stability of the conformation, does not affect the rheological properties (Hassler and Doherty, 1990). In high concentrations, the acetyl position seems to be more important where α-acetylation seem to decrease the viscosity more than β-acetylation, indicating a better stabilizing effect of acetate at the internal α-mannose (Gansbiller et al., 2019).

Structural variation in xanthan side chains caused by different substitution patterns (Section 2.1.1) in the wild type results in different physicochemical properties of xanthan, which contributes to it being a complicated material to research. (Kool et al., 2013)

2 THE AIM OF THE THESIS

The aim of this thesis can be divided into a main objective and several sub-objectives. New applications of xanthan will be made possible by controlling its properties, but chemical or enzymatical modification could lead to costly downstream processing or an impure product. Thus, biotechnological tailoring of xanthan properties could be the solution.

To achieve sufficient control, it is necessary to confirm how modifications influence the properties of the biopolymer. A hypothesis in this thesis is that this understanding can be achieved by doing a comparative characterization of different xanthan variants derived from biotechnologically modified *Xanthomonas campestris spp*. mutants using SEC-MALS and NMR spectroscopy.

2.1 Main objective:

The main objective was to characterize xanthan material produced from different gene-knockout mutants of *X. campestris spp*. using SEC-MALS and NMR spectroscopy. This was done to gain more knowledge about biotechnologically modified xanthan material, investigate how the chemical composition of the side chain affects its properties and simultaneously evaluate the use of these techniques for xanthan characterization. Ultimately, this would lead to a better understanding of how biotechnological tools can be used to engineer new polysaccharides with specific chemical compositions and properties.

2.1.1 Sub-objective production:

Produce xanthan material by fermenting mutant strains of *X. campestris ssp.* in a bioreactor and extract the xanthan material from the fermentation broth using centrifugation, filtration, and isopropanol precipitation.

2.1.2 Sub-objective preparation:

Mechanically degrade the material down to lower molecular weight using Wet Mill Jet Star Burst Mini homogenizer to homogenize the samples and improve readability of NMR-spectra.

2.1.3 Sub-objective characterization:

Measure the weight-average molecular weights, radii of gyration and mass distributions using SEC-MALS, find the temperature of the midpoint of the order-disorder transition by using a series of different temperature ^{1}H-NMR experiments and attempt to assign chemical shifts using 2D-NMR.

3 EXPERIMENTAL THEORY

3.1 Metabolic engineering of exopolysaccharide producing bacteria

Researchers use biotechnology to purposefully modify the cellular metabolic networks of exopolysaccharide producing bacteria. This branch of biotechnology aims to create novel polysaccharides with enhanced or novel properties and functions. Polysaccharide engineering involves modifying the structure, composition, and interactions of natural polysaccharides using chemicals or enzymes, or synthesizing new ones from scratch using genetic tools. By using genetic tools, polysaccharide engineers can modify EPS by removing, adding, or changing genes that are important in the biosynthesis of the polymers. These new EPSs can have potential applications in various fields, such as medicine, agriculture, food, and material science. (Schilling et al., 2020)

An example of how this can be seen in Figure 3-1, where two different approaches of removing the acetate and pyruvate substitutions of xanthan is shown. The first approach is based on either chemically or enzymatically removing the substituents of xanthan from a non-modified variant of *X. campestris*. The second approach is to remove the genes that produce acetyltransferases and pyruvate ketalase, thereby preventing the synthesis of xanthan with acetate and pyruvate. The second approach also attempts to do modifications at the highest possible level and avoid down-stream actions and processing.
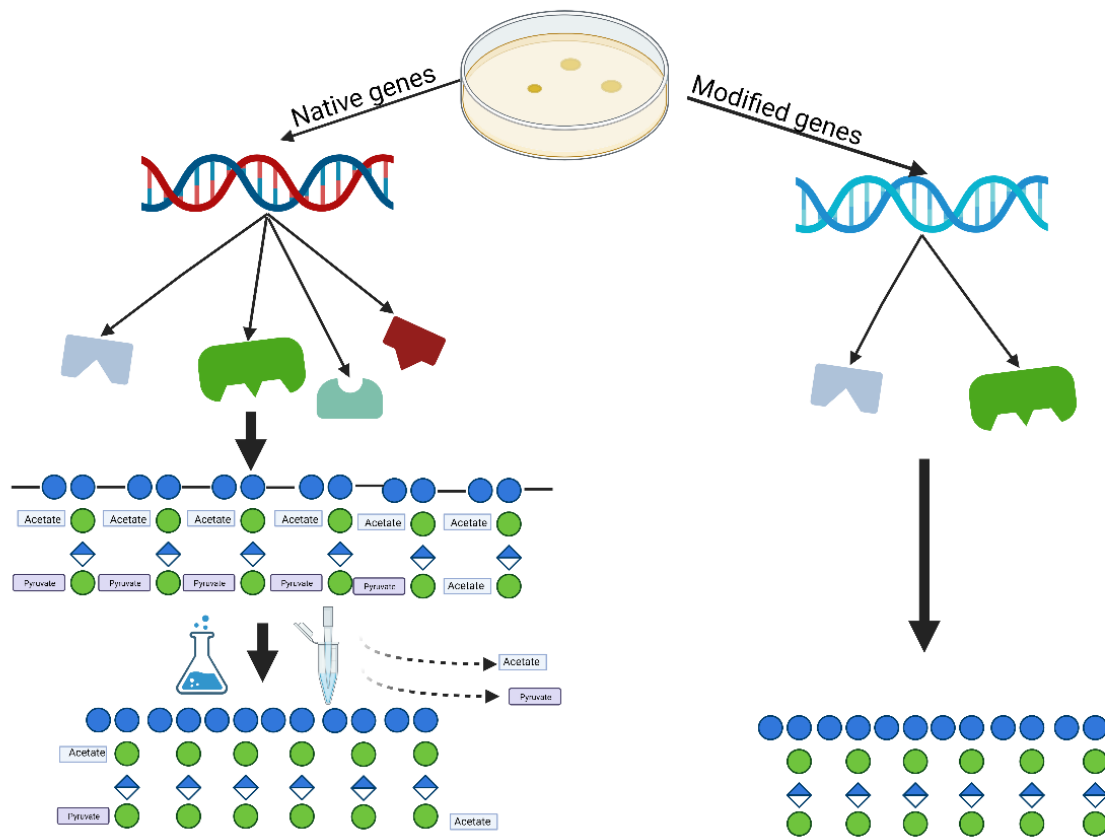
Figure 3-1 Two different approaches to engineer new polysaccharides. The process stream to the left uses chemicals or enzymes to remove the acetate and pyruvate from wild type xanthan post-production while the process stream to the right avoids acetate and pyruvate attachment during biosynthesis by genetic modifications.

3.2 Mechanical degradation of polymers using high shear forces

In some cases, it is desirable to reduce the viscosity of highly viscous polysaccharides. Since viscosity is highly linked to the molecular weight of the polysaccharide, viscosity reduction can be accomplished by depolymerization. Early methods of polysaccharide depolymerization like chemical hydrolysis or ultrasonication were not suited for all purposes. In the case of polysaccharides that have a multi-stranded helical structure, a new method was designed that was more suited for industrial and large-scale use. This method involved forcing a solution of a rod-like polysaccharide to flow at a high shear rate through a capillary. (Takemasa Kojima, 1983)

There are multiple manufacturers of high-pressure homogenizers that use this principle, and some of these designs are based on colliding the particles either with themselves or other objects like decentered ceramic balls. A ball type chamber loads a sample into a pressurizer and forces it through a slit to collide with a ceramic ball where it is pulverized and dispersed. An overview of this principle and how it could be performed can be found in Figure 3-2. (SUGINO MACHINE LIMITED)

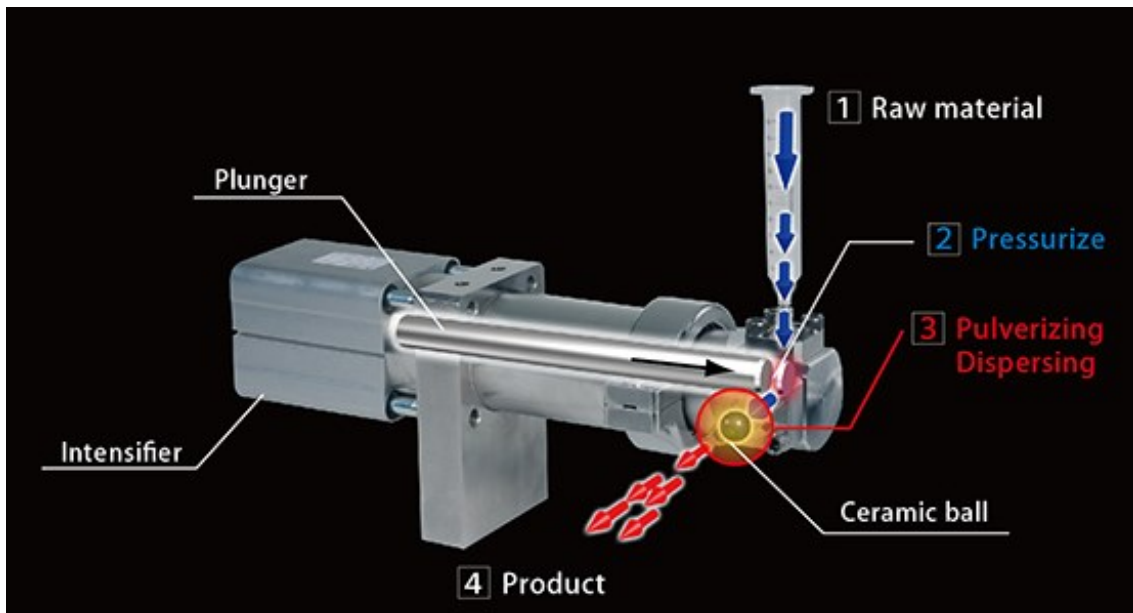*Figure 3-2 A schematic of the Wet Mill Jet Star Burst Mini homogenizer, providing an overview of the principle behind mechanical shear degradation of a raw material. A sample (1) is sucked into a pressure chamber where it is pressurized (2) and forced through a nozzle that increases the shear rate. The pulverization and dispersion happen when the sample collides with the ceramic ball at high pressure (3).*

3.3 SEC-MALS

This section will provide an explanation of the theory behind the concepts of size-exclusion chromatography combined with multi-angle laser light scattering (SEC-MALLS). It will also explain how this experimental method can be used to measure the weight-average molecular weight (M_w) of a disperse polymer sample. Other types of light scattering like dynamic light scattering exist, only static light scattering will be discussed further in this chapter.

3.3.1 Size exclusion chromatography

The basic principle of size exclusion chromatography (SEC) can be explained as using chromatographic columns that are packed with small particles of porous material for separating fragments by size. Both the pores and the space between the particles are filled with a mobile phase. The column is connected to a sampler and a concentration detector. The sampler injects a dilute sample of particles, dissolved or dispersed in the same mobile phase as the column, into the column along with a continuous addition of more mobile phase or solvent. Particles of smaller hydrodynamic volume from the injected sample can permeate the pores and be retarded in the column, while the particles of bigger hydrodynamic volume can pass the porous material and elute faster. Consequently, the particles are separated based on hydrodynamic volume and the concentration detector will detect bigger particles earlier in the elution volume. (Podzimek, 2011c)

The concentration sensitive detector, either a refractive index or UV-detector, measures the concentration and molecular weight distribution of the sample solution. This data provides information about the dispersity of the sample and can be used to calculate different molecular weight averages when combined with light scattering data. (2011c)

3.3.2 Static light scattering

In general, light scattering analysis uses a phenomenon where light is scattered in dilute solutions or dispersions of macromolecules/particles to characterize and elucidate the intrinsic properties of a sample. The light scattering phenomenon is a result of the interaction between oscillating electromagnetic fields, like light, and matter. When a neutral molecule is opposed to an oscillating electromagnetic field, the "electron cloud" surrounding the molecule is affected and displaced by the radiation and turns into an oscillating dipole. Consequently, this oscillating dipole becomes a new source of radiation that can be detected as a voltage and is recorded as intensity. The tendency of the polarizability of a molecule will determine its ability to scatter light and is directly proportional to the specific refractive index increment (*dn/dc*). If the electron cloud is smaller than λ/20 (λ = wavelength) the entire cloud is in the same identical phase and will scatter light independent of the angle. However, if the "electron cloud" is greater than λ/20, the entire electron cloud is not in the same phase and will create intramolecular phase interference that creates angle dependent light scattering. (Podzimek, 2011b)

Static light scattering (SLS) is a popular type of light scattering that yields the weight-average molecular weight (M_w), molecular size expressed as the radius of gyration (R_G), and the second virial coefficient (A_2). It measures the intensity *I* of the scattered light at different angles over a longer time-period and creates an average intensity per angle θ. This intensity is then converted to the Rayleigh ratio R_θ from the voltage measured by photodiodes through Equation 1. (Podzimek, 2011b)

Equation 1

$$R_\theta = \frac{(I_\theta - I_{\theta,solvent})r^2}{I_0 V} = f\frac{V_\theta - V_{\theta,solvent}}{V_{laser}}$$

In Equation 1, I_θ is the scattered light intensity of the solution; $I_{\theta,\text{solvent}}$, is the scattered light intensity of the solvent; I_0 is the intensity of the incident radiation; V is the volume of the scattering function; r is the distance between the scattering volume and detector; V_θ, $V_{\theta,solvent}$, and $V_{\theta,laser}$ are detector signal voltages of the solution, solvent, and laser, respectively; and f is an instrumental constant. As one might realize, this equation gives an excess Rayleigh ratio, which is the difference between the solution and the solvent. (Podzimek, 2011b)

The R_θ relates to the properties of the macromolecule through Equation 2 where c is the concentration of the polymer, M is the molar mass, A_2 is the second virial coefficient, $K*$ is the optical constant and $P(\theta)$ is particle scattering function. (Podzimek, 2011b)

Equation 2

$$\frac{R(\theta)}{K^*c} = \text{MP}(\theta) - 2A_2cM^2P^2(\theta) + \cdots$$

K* is defined for the vertically incident light as:

Equation 3

$$K^* = \frac{4\pi^2 n_0^2}{\lambda_0^4 N_A}\left(\frac{dn}{dc}\right)^2$$

Where n_o^2 reflects the refractive index of the sample solvent, N_A is Avogadro's number, and $(dn/dc)^2$ is the specific refractive index increment of scattering macromolecules. Meaning that the $K*$ depends on the square of the (dn/dc) of the solution, which can be calculated using refractometry. (Podzimek, 2011b)

The second virial coefficient relates to the interaction between the solvent and the solute. Positive values of A_2 indicates good solvent conditions, while the opposite is true for negative values of A_2. (Podzimek, 2011b)

The particle scattering function $P(\theta)$ describes how the intensity of the scattered light depends on the angle. This can be used as a measure of the intramolecular phase interference of the particles and can be used to calculate the radius of gyration. (Podzimek, 2011b)

Based on all these dependencies, weight-average molecular weight (M_w) and the z-average radius of gyration ($R_{G,z}$) can be determined as shown in Equation 4. (Christensen, 2021)

Equation 4

$$\frac{K^*c}{R_\theta} = \left(1 + \frac{16\pi^2 R_{G,z}^2}{3\lambda^2} sin^2\left(\frac{\Theta}{2}\right)\right)\left(\frac{1}{Mw} + 2A2c\right)$$

3.3.3   Weight averages of the molecular weight and radius of gyration

Different averages might be obtained depending on how the molecular weight of a polymer in the solution is measured. Two common averages are number-average and weight-average molecular weights. To find the number average molecular weight, the sum of number of units *i* (N_i) times the molecular weight of *i* (M_i), is divided by the sum of N_i. (Christensen, 2021)

Equation 5

$$M_n = \frac{\sum_i N_i M_i}{\sum_i N_i}$$

The weight-average molecular weight is found by taking the sum of number of units *i* (N_i) times the molecular weight of *i* to the power of two (M_i^2), and divide it by the sum of N_i times M_i. (Christensen, 2021)

Equation 6

$$M_w = \frac{\sum_i N_i M_i^2}{\sum_i N_i M_i}$$

The number-average molecular weight (M_n) is simply the normal average molecular weight of the polymers in the solution, while the weight-average molecular weight (M_w) is a higher moment of the normal equation for molecular weight-average which depend more on the contribution of the molecules according to their size. Popular methods for determining the M_w of disperse solutions include static light scattering combined with size exclusion chromatography. (Christensen, 2021)

Radius of gyration and weight average radius of gyration are two important parameters that describe the size and shape of a polymer molecule. The radius of gyration is defined as the root mean square distance of the polymer segments from the center of mass of the molecule. The R_G value retrieved from static light scattering data processed by software such as ASTRA, is usually referred to as the z-average radius of gyration. ASTRA also provides estimations of the weight-average mean square radius, R_w. (Christensen, 2021, Wyatt Technology Corporation, 2019)

3.3.4   Combination of SEC and Light Scattering

Combining SEC and light scattering in a single set-up is probably the most common method to determine molecular weight distributions, weight averages and radius of gyration. Two consecutive on-line detectors collect data at regular intervals called elution slices that are processed by software to create a readable output. This allows the user to see the distribution and molecular weight and size change along the elution volume axis. (Podzimek, 2011a)

When combining the SEC and light scattering in a set-up, software such as ASTRA can create a fitted plot of the data and extrapolate the M_w and R_G. There are several ways of obtaining a fitted plot, and choosing a suitable method and fitting degree is important for data analysis. (Christensen, 2021)

3.4 The basic principle of NMR Spectroscopy

Nuclear magnetic resonance (NMR) spectroscopy has since the beginning of the 1950's been an important tool for further understanding of the chemical structure of substances. After learning about the magnetic nuclear properties of atomic nuclei, researchers started to construct and develop tools that could use this phenomenon to characterize the chemical structure of a substance. The importance of this technique has steadily increased ever since its discovery and has contributed to major developments in many research fields. (Günther, 2013)

The quantum mechanical principle for NMR spectroscopy is a highly advanced field and will for the purpose of staying withing the scope of this master project be simplified to the degree that is needed to interpret the results from the experiments.

To help better understand the basic principles of NMR spectroscopy, one should consider some quantum mechanical properties of atomic nuclei. An atomic nucleus consists of protons and neutrons, which are both elementary particles with intrinsic angular momentum or "spin". The spin quantum number (I) is the value of the total spin of a nucleus. I can be either an integer or a half-integer depending on whether the number of protons and neutrons is even or odd. Nuclei with a non-zero spin quantum number have a magnetic moment (μ), which is a vector quantity that describes the strength and direction of the magnetic field generated by the spinning nucleus. (Tampieri et al., 2021)

Objects with a magnetic moment interact with an external magnetic field (B_0) and tend to align themselves with or against it and precess with a frequency $\omega = -\gamma B_0$, where γ is a constant called the gyromagnetic ratio that depends on the type of nucleus. The possible orientations of the magnetic moment are called spin states and are determined by the spin quantum number. The number of allowed orientations or spin states is given by $2I + 1$, so for example, a nucleus with $I = 1/2$ has two spin states, while a nucleus with $I = 1$ has three spin states. A nucleus with a non-zero quantum spin number that is placed in an external magnetic field (B_0) will align its magnetic moment with the field and create its own current in a field-aligned direction and plane. For a ^{1}H nucleus with $I = 1/2$, there are two energy levels: one lower level where the magnetic moment is aligned with B_0 (α-state), and one higher level where the magnetic moment is opposed to B_0 (β-state). The energy difference between these two levels is given by $\delta E = \gamma B_0 h/2\pi$, , where *h* is Planck's constant. (Tampieri et al., 2021)

By applying an electromagnetic field perpendicular to the direction of the B0 field, the nuclear spins will experience a torque that pushes them from their equilibrium orientation along the z-axis onto the x,y-plane. Precession on this plane induces a current in a detector generating a time-domain signal. The precession frequency if affected by the chemical environment around the nucleus. This effect is called the chemical shift, which contains information about the chemical structure of a compound. The signal obtained can also provide quantitative information about the composition of a sample. The area under each peak in an NMR spectrum corresponds to the number of nuclei that resonate at that frequency. Therefore, by comparing the areas of different peaks, one can determine the relative amounts of different compounds in a sample. This assumes that the relative intensity of the peaks is proportional to the concentration of each compound. (Günther, 2013)

A coupling constant is a measure of how much two nuclei interact with each other through their magnetic fields. It is also known as spin-spin coupling or indirect dipole-dipole coupling. The coupling constant depends on the chemical bonds that connect the two nuclei, and it can provide information

about the relative bond distances and angles. The coupling constant can also reveal the connectivity of chemical bonds, as it is responsible for the splitting of resonance lines in NMR spectra. The coupling constant is usually denoted by *J* and expressed in hertz (Hz). It can have different values and signs depending on the type and number of nuclei involved. (Hahn and Maxwell, 1952)

3.4.1 Types of NMR experiments

There are several types of NMR experiments, each giving different types of information to assist in structural elucidation. ^{1}H-NMR, or proton NMR, records chemical shifts, coupling constants and integrals from ^{1}H nuclei in the sample in a one-dimensional spectrum. Other experiments can combine other nuclei (e.g., ^{13}C) with ^{1}H to create multi-dimensional spectra. Heteronuclear Single Quantum Coherence (HSQC) is an experiment that creates a two-dimensional spectrum that shows peaks representing single-bond correlations between protons and carbons, with the ^{1}H and ^{13}C chemical shifts on the x- and y-axis respectively. (Yao et al., 2021)

Heteronuclear multiple bond correlations (HMBC) experiments show long range J-couplings between protons and carbons that are two, three and sometimes even four bonds away, while the direct one-bond correlations are suppressed. Variations of this experiment allow us to separate some of these correlations where H2BC can select and present only two-bond correlations. (Yao et al., 2021)

These experiments can reveal important structural features of organic molecules, such as the presence of functional groups, ring systems, double bonds, and aromaticity. By combining the information from different NMR experiments, one can obtain a comprehensive picture of the molecular structure of a compound. (Yao et al., 2021)

1D NMR (^{1}H and ^{13}C NMR) is a common technique for the structural analysis of polysaccharides. It can provide information about the monosaccharide composition, linkage types, anomeric configurations, and substituent groups of polysaccharides. The chemical shift of both the α- and β-configuration of the anomeric protons and carbons as well as functional groups such as carboxyl or methyl groups often appear at specific frequency regions. However, this can depend on many factors like temperature, ring structure, substitutions, linkages, and solvent conditions. (Yao et al., 2021)

To distinguish and identify chemical shifts that are less recognizable one can use the coupling constants between, for instance the anomeric (H1, C1) and other protons and carbons in the sugar ring. In general, the coupling constant between two nuclei is larger when they are closer together and have a smaller dihedral angle. For example, in an α-sugar, the coupling constant between the anomeric proton and carbon and the proton and carbon at C2 is larger than that in a β-sugar, because they have a smaller dihedral angle due to their axial orientation. Similarly, in a β-sugar, the coupling constant between (H1, C1) and (H5, C5) is larger than that in an α-sugar, because they have a smaller dihedral angle due to their equatorial orientation. Therefore, by measuring the coupling constants between (H1, C1) and other protons and carbons in the sugar ring, one can deduce whether a sugar residue has an α- or β-configuration. (Gerwig, 2021)

Structural analysis of polysaccharides using just 1D-NMR has its limitations, but most of these limitations are resolved by using two-dimensional NMR. A 2D NMR technique called Homonuclear [1]H-^{1}H correlation spectroscopy (^{1}H-^{1}H COSY) can be used to investigate the correlation of adjacent protons and can stepwise connect the protons in a spin system or sugar ring. Another proton correlation technique called total correlated spectroscopy (TOCSY) can find the total correlation of all the protons in one sugar ring system on the same vertical and horizontal line of the 2D-spectrum. HSQC and HMBC

can be used to investigate correlations of proton and carbon nuclei in a similar way to stepwise connect correlating protons on carbons from the same spin system. HMBC as well as through-space proton-proton correlation spectra like NOESY (Nuclear Overhauser Effect SpectroscopY) is often used in polysaccharide analysis to find the sequence of the monosaccharides. (Yao et al., 2021)

One of the challenges in nuclear magnetic resonance (NMR) spectroscopy of high molecular weight polymers is the line broadening effect, which reduces the resolution and accuracy of the analysis. Line broadening occurs when the polymer chains have high molecular weight and slow tumbling rates, or different conformations and orientations in solution, resulting in a range of chemical shifts for the same type of nuclei. A possible way to improve the NMR spectra of high molecular weight polymers is to depolymerize them into smaller fragments, which have more uniform structures and faster tumbling rates. Depolymerization can be achieved by various methods, such as mechanical degradation, chemical cleavage, or enzymatic hydrolysis. Depolymerization of high molecular weight polymers, combined with heating to increase molecular tumbling, reduces the line broadening effect and results in sharper NMR signals. (Cheetham and Mashimba, 1992)

3.4.2   NMR-studies of xanthan

This section attempts to identify the state of the interpretation of NMR data of xanthan. It will also demonstrate that there is a knowledge gap in this field that should be addressed.

Early NMR studies used synthetic analogous pyruvic acetals of methyl glycosides to determine the configuration of the link between the mannose residue and pyruvate found in polysaccharides like xanthan (Garegg et al., 1980). Later, a study used chemically modified xanthan where either acetate, pyruvate or both had been removed to further confirm and approximately assign more carbon chemical shifts using ^{13}C NMR (Rinaudo et al., 1983). ^{1}H NMR results from the same study found the chemical shift of the α anomeric proton signal and the proton signals of the methyl groups of acetyls and pyruvyls. A more complete study used both ^{1}H- and ^{13}C NMR on enzymatically hydrolyzed xanthan with varying degrees of acetylation and pyruvylation and managed to partially assign the different chemical shifts of xanthan (Cheetham and Mashimba, 1992). Even though β-D-mannose acetylation had been hypothesized, this study was published 21 years before it was proven or its position was confirmed (Kool et al., 2013, Hassler and Doherty, 1990). It is reasonable to assume that the available NMR assignment of xanthan is outdated and incomplete.

Xanthan researchers argue that both one- and two-dimensional NMR spectroscopy is a useful tool to investigate the structure of heteropolysaccharides like xanthan, and structural modifications of xanthan seem to be sought after by the different industries that use xanthan (Fu et al., 2022, McIntyre et al., 1996).

3.4.3   Melting curves

Rigid conformations like the double helix structure of xanthan have low molecular tumbling, leading to fast relaxation rates which in turn lead to wide peaks on NMR spectra. However, heating the solution and causing an order-disorder transition of xanthan, increases its mobility, giving sharper signals, which improves the readability of the spectrum. (Morris et al., 1977)

Because of this phenomenon, a plot of the integral of a suitable reporter peak from a series of NMR measurements of xanthan in increasing or decreasing temperature can be fitted to a sigmoidal curve. A melting temperature, T_m, can be extrapolated from this curve by using a sigmoidal Boltzmann-like equation like Equation 7.

Equation 7

$$I = I_{min} + \frac{(I_{max} - I_{min})}{1 + e^{(T_m - T)/slope}}$$

The T_m represents the point where 50 % of the sample is thought to have denatured and could be considered the order-disorder mid-point transition value or melting temperature. *I* is the measured intensity, *Imax* and *Imin* are fitted parameters describing the top and bottom of the sigmoidal curve respectively. *Slope* represents the steepness of the curve.

4 MATERIALS AND METHODS

This chapter explains how the xanthan materials were obtained, how the experiments were conducted, and what instruments were used. Figure 4-1 shows an overview of the steps that were performed in this master project. Step 1 "Gene editing" was done before this project by the researchers at the research lab of Prof. Dr. -Ing. Jochen Schmid at the University of Münster. To perform this project, the *X. campestris spp.* variants were borrowed from the lab and used to produce powdered xanthan material together with the help and supervision of Dr Moritz Gansbiller. In addition to the powdered xanthan material, a small sample (50 ml) of cross flow filtered supernatant of each variant was retrieved. This was done to have a non-extracted, non-dried and non-milled reference to the normal dry powder. This sample was, however, not further analyzed.

1. Gene editing

2. Fermentation

3. Crossflow filtration and extraction

4. Mechanical degradation

5. Dialysis

5b. SEC-MALS

6. Freeze drying

6b. NMR spectroscopy
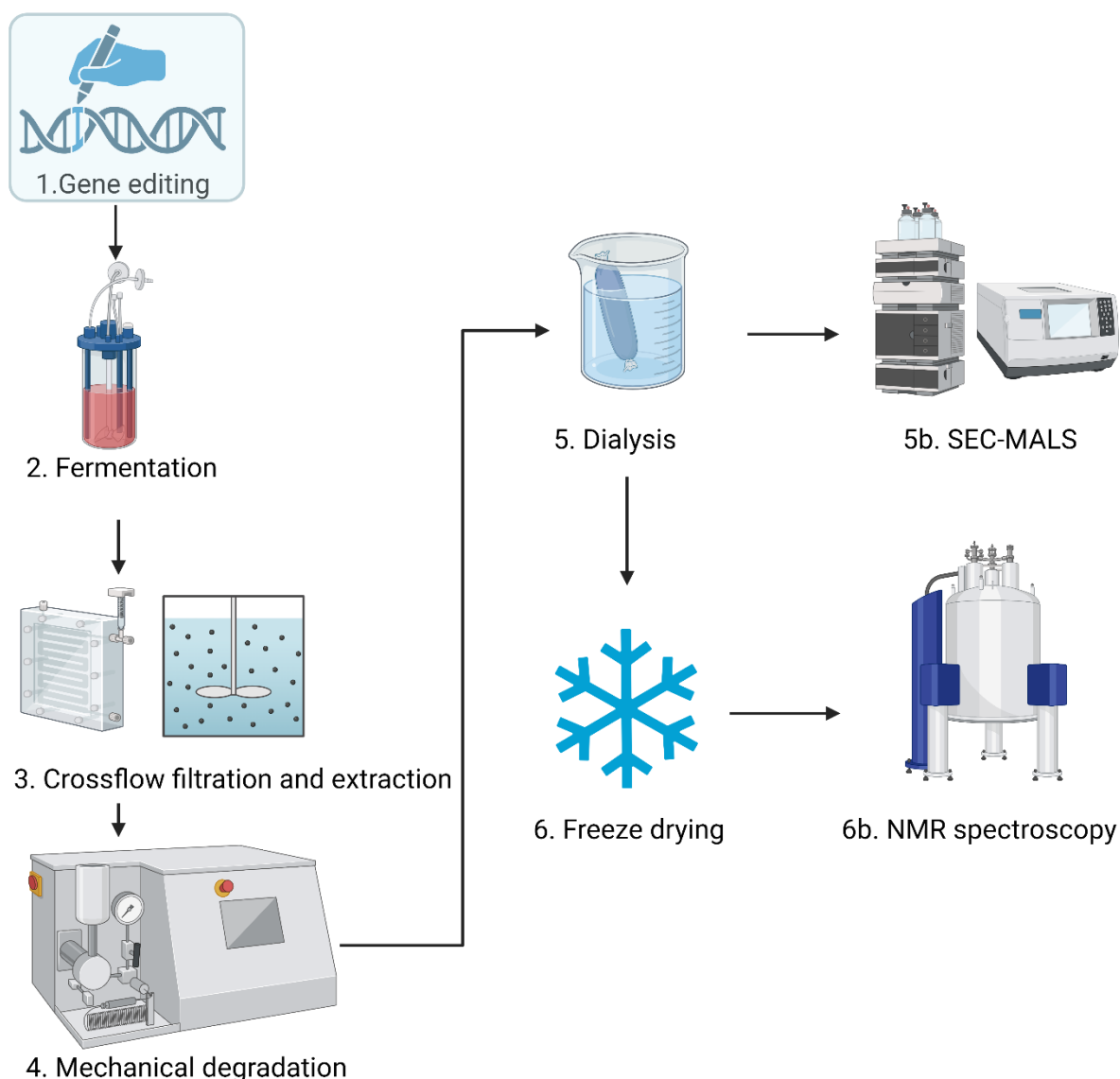
Figure 4-1 Overview over the steps in performed in this master project. The shaded step "gene editing" (1) was not done as a part of this project but was done by the researchers at the research lab of Prof. Dr.-Ing. Jochen Schmid at the University of Münster. Fermentation (2) of the wild type and gene edited mutants (1) must be filtrated before extraction (3). After the material is extracted, it is processed (4,5,6) for SEC-MALS and NMR spectroscopy.

4.1 Materials

4.1.1 Xanthan variants

The xanthan variants used in this project were made by the researchers at the research lab of Prof. Dr. -Ing. Jochen Schmid at the University of Münster. More on the production of mutants can be found in the article "In-depth rheological characterization of genetically modified xanthan variants" by Gansbiller et al. (2019).

In the article from Gansbiller et al. (2019) the different strains of *X. campestris* xanthan were named based on which genes were deleted. For instance: *X. campestris* without *gum*L was named *Xcc ΔgumL*. The xanthan variant produced by Xcc ΔgumL was called XanΔL. The same nomenclature was used for the strain while the xanthan material was shortened by removing "Xan" from the variant named (e.g., XanΔL = ΔL).

The strains used in this project was:

- *Xcc wt (Wild type or WS)*
- *Xcc ΔgumL (ΔL)*
- *Xcc ΔgumFGL (ΔFGL)*
- *Xcc ΔgumFG (ΔFG)*
- *Xcc ΔgumF (ΔF)*
- *Xcc ΔgumG (ΔG)*

4.1.2 Buffers, media, and solutions

- EPS Medium – agar plate: EPS medium in 1% agar gel
- SEC-MALS buffer: 150 mM $NaCO_3$/0.25 mM EDTA
- High ionic strength buffer for stability experiment: $MgSO_4$ 0.5 M
- NMR solvent: D_2O 99.9 % atom D from Sigma-Aldrich
- Antifoam: Antifoam B Emulsion 1 % from Sigma-Aldrich
- Fermentation base: NaOH 2 M
- Fermentation acid: H_3PO_4 7%
- EPS medium: The complete medium consisted of a mixture of the base medium and several supplement solutions (Table 4-1). The g/L represents the final concentration of the fully mixed medium.

Table 4-1 List of the contents of the base media and supplement solutions that the complete EPS medium consisted of and the final concentration of the fully mixed medium.

	Ingredients	g/L
Base media	Peptone from casein	5.00
	$MgSO_4$ x 7 H_2O	1.33
Supplement 1	$CaCl_2$ x 2 H_2O	0.05
	Glucose Monohydrate	33.00
Supplement 2	KH_2PO_4	1.67
Supplement 3	Vitamin mix (ml)	2.00
	Micronutrients (ml)	1.00

4.1.3 Instrumentation

- Biostat B plus 2 L Bioreactor by Sartorius was used to ferment the strains
- CEPA Z-61 flow through centrifuge was used to centrifuge diluted fermentation broth
- Hydrosart Sartorius AG (100 kDa cut-off) ultrafiltration cassette was used for crossflow filtration
- Retsch ZM 200 centrifugal mill was used to mill the dried xanthan material into a fine powder
- Wet Mill Jet Star Burst Mini homogenizer was used to mechanically degrade the samples
- B 1-8 LDplus from Martin Christ Freeze Dryers with an Edwards E2M18 vacuum pump
- Bruker 600 MHz Avance NEO equipped with a 5-mm TBO iProbe was used for NMR experiments
- Agilent Technology 1260 Infinity with a OH pak Lb-G 6B guard column and a OHpak LB-806M main column and a Shodex RI-501 RI-detector connected to a Wyatt Technology DAWN Heleos-II multi-angle light scattering detector was used to perform the SEC-MALS experiments

4.1.4 Software

- NMR spectra were processed and analyzed using Bruker TopSpin version 4.1.4
- SEC-MALS data was processed ana analyzed using ASTRA version 7.3.2
- Biorender was used to create illustrative figures
- Visual studio code, Python 3, and libraries NumPy, Matplotlib, SciPy and Pandas were used to process data and make plots
- Microsoft excel was used to make diagrams and charts
- Inkscape was used to annotate NMR-spectra

4.2 Methods

4.2.1 Precultures

The *Xcc wt*, *Xcc ΔgumL*, *Xcc ΔgumFGL* and *Xcc ΔgumFG* (Gansbiller et al., 2019) were kept at minus 80 °C and were carefully plated out (EPS Medium plate) and inoculated in separate sterile tubes (Falcon 15 ml, EPS medium). Both plates and tubes were inoculated in an agitating incubator (20 h, 250 rpm, 30°C). The plates and tubes were inspected after 20 h to confirm growth. After growth was confirmed, 1 ml of each tube and 50 ml of EPS medium was transferred to a 250 ml baffled shake flask with membrane screwcap and incubated in an agitating incubator (72 h, 250 rpm, 30 °C).

The bioreactors (Biostat B plus 2L) were prepared by autoclaving the equipment with the base media already added. The base media and supplements were prepared and autoclaved separately to avoid aggregation or Schiff-base formation between proteins and sugars. After cooling, the supplements were added and the complete EPS medium was then adjusted to correct the pH (6.8 pH), stirring speed (600 rpm, two six-blade stirrers), airflow (1.5 L/min) and pO_2 (30 %). After adjusting the parameters, the OD of the preculture was measured to get a final OD of 0.3 in the fermenters when adding the preculture to the complete media. During the fermentation process (30 °C), the bioreactor automatically controlled the pH-level and foaming level by the addition of acid (H_3PO_4 7%), base (NaOH 2M) or antifoam (Antifoam B Emulsion 1%). However, the fermentation broth was monitored manually throughout the fermentation process to avoid over-foaming and oleic acid was added as an antifoam when the bioreactor was not able to regulate the foam level itself using its own source of antifoam agent (Antifoam B Emulsion 1%). The full process and preparation of the bioreactor is described in appendix I.

After the fermentation process, two 1 L centrifuge bottles per bioreactor were prepared and each bottle filled with 100 grams of fermentation broth and 900 grams of 10 mM NaCl solution. The bottles were then centrifuged (CEPA Z-61 flow through centrifuge, 17,000 g for about 40 min). After the centrifugation, the supernatant was crossflow-filtered with 10 mM NaCl solution (100 kD pore size membrane).

After filtration, approx. 50 ml of the supernatant was added to four separate tubes (Falcon, 50 ml) while the rest of the supernatant was precipitated using isopropanol. The precipitate was dried overnight in a vacuum drying oven (20 h, 42 °C, 38 mbar) and milled to a fine powder after drying (Retsch ZM 200 centrifugal mill, 18,000 rpm with 1 mm milling grid).

4.2.2 Mechanical degradation and further preparation

The dry xanthan powder was solubilized in milliQ-water (MQ) (50 mg xanthan/5 ml MQ, 24 h of agitating in RT). The solubilized material was further diluted with a 2x SEC-MALS buffer (300 mM $NaCO_3$/0.5 mM EDTA) to 5 mg/ml and agitated at RT for 24 h. Finally, the samples were diluted to 1 mg/ml using 1x SEC-MALS buffer and then run through the Wet Mill Jet Star Burst Mini homogenizer for ten cycles. The material was cooled down using an ice bath for 5 min and sampled (1 ml) between per cycle.

After the mechanical degradation, around 40 ml of each degraded sample was stored in a glass container and eleven 1 ml samples (0-10 cycles) in Eppendorf tubes. The 1 ml samples were prepared for SEC-MALS analysis by dilution from 1 mg/ml to 0.5 mg/ml using the same mobile phase as used for

the SEC-MALS analysis, filtered (0.45 µm) and transferred to SEC-MALS vials (1.5 ml). The rest of the glass container was dialyzed with 10 mM NaCl for 20 ± 2 h (Dialysis tubing, size 2 Inf Dia 18/32" – 14.3 mm: 30 M, 12-14 kDa cut-off, Medicell International Ltd) and then dialyzed against pure MQ-water for 24 h and finally freeze dried (B 1-8 LDplus) for 24 h.

4.2.2.1   Preparations for stability experiment

Three parallels of both the ΔG and ΔF samples were analyzed using SEC-MALS. Each variant had one reference sample (A) that used the standard protocol as described in chapter 4.2.2, one stabilized sample (B) that followed the standard protocol except that a $MgSO_4$ 0.5 M solution rather than the SEC-MALS buffer during mechanical degradation, and a destabilized sample (C) that also followed the standard protocol in chapter 4.2.2 except that it was not cooled with an ice bath between the cycles. A SEC-MALS sequence of two injections per sample was prepared as explained in chapter 4.2.3.

Table 4-2 Three parallels of both ΔG and ΔF with different protocols. One reference protocol (A), one stabilizing (B) and one destabilizing protocol (C).

	Standard	Stabilized	Destabilized
ΔG	GA	GB	GC
ΔF	FA	FB	FC

4.2.2.2   Active carbon treatment

A wild type sample mechanically degraded nine cycles was used to test the removal of impurities by activated carbon (A.C., Charcoal Decolorizing Powder, BDH laboratory supplies, 325 mesh) treatment. Two parallels were prepared for SEC-MALS as explained in chapter 4.2.2, but one of the parallels were treated with A.C. The A.C. treatment involved addition of 10 mg of A.C. and being agitated for 3 h before filtration (0.45 µm). A sequence of two injections per sample was prepared as explained in chapter 4.2.3.

4.2.3   SEC-MALS

All samples were prepared according to chapter 4.2.2 before a sequence with two SEC-MALS experiments per sample was prepared. The experiments per sample had two different injection volumes, 50 and 25 µl for comparison. The differential refractive index increment and second virial coefficients of respectively 0.15 mL/g and $1.0*10^3$ mol*mL/g^2 were selected with the help of Prof. Bjørn E. Christensen. (Osebakken, 2019, Holmvik, 2018)

4.2.4　NMR

Six milligrams each of the freeze-dried material from chapter 4.2.2 were solubilized in 500-550 µl D_2O in NMR tubes w/caps (Wilmad LabGlass) and analyzed using the Bruker 600 MHz Avance NEO equipped with a 5-mm TBO iProbe. Table 5 gives an overview of the recorded experiments. Unless specified, all experiments were recorded at 355 K with 10 min equilibrating between measurements.

Table 4-3 NMR experiments done on each xanthan material variant. All the material variants were analyzed using ^{1}H-NMR at a range of temperatures (298, 313-363 K, 10 min equilibrating between measurements) to estimate a melting curve and melting temperature (T_m). Further, only the WS-type was analyzed using HSQC, HMBC and H2BC. ΔL, ΔFGL and ΔG was analyzed using HSQC and HMBC.

	^{1}**H-NMR (298,313-363 K, 10 min equilibrating between measurements)**	**HSQC**	**HMBC**	**H2BC**
WS	+	+	+	+
ΔL	+	+	+	-
ΔFG	+	+	-	-
ΔFGL	+	+	+	-
ΔF	+	+	-	-
ΔG	+	+	+	-

4.2.5　^{1}H-NMR melting curve plotting

Tm was estimated for all the samples by plotting the integral values of reporter peaks from each ^{1}H-NMR spectra using a python script to fit Equation 7.

The script and input data can be found through this link:

https://github.com/gcourtade/masters/tree/main/2023/KJ_Xanthan_Tm

For all the reporter peaks of the ΔL and the methyl peaks of ΔG, plots of the n-th discrete difference along the y-axis (i.e., integral) were made as shown in appendix C.

4.2.6　2D-NMR assignment strategy

To find spin systems in the 2D-NMR spectra that were obtained, an assignment strategy based on known principles of carbohydrate NMR was used. This strategy used a combination of different NMR experiments, where HSQC spectra were superimposed with HMBC and H2BC spectra to find ^{1}H-^{13}C correlations. This strategy is exemplified and explained in appendix D.

5 RESULTS

5.1 Fermentation results

5.1.1 Selecting mutant strains

Since only four fermenters were available, the project was restricted to four mutants at first. Because it was desirable to compare xanthan variants that were the most contrastive, the *Xanthomonas* variants that were selected were: one wild type (WS), one without pyruvate on the side chains (ΔL, i.e., where *gum*L was deleted), one without acetate on the side chains (ΔFG) and one with neither pyruvate nor acetate on the side chains (ΔFGL). The reason was that selected mutants would reveal how pyruvate and acetate influence the ordered structure of the double strand.

After the first four mutants were analyzed, material from two more mutants (ΔF and ΔG) were sent from the research lab of Prof. Dr. -Ing. Jochen Schmid at the University of Münster. This material was tested in the same manner as the first four samples (wild type, ΔFGL, ΔFG and ΔL) and used for tests described in chapter 4.2.2.1 and chapter 4.2.2.2.

The different possible trimeric side chain compositions are presented in Figure 5-1. When including the glucose backbone of the polysaccharide, as well as the side chain, it is commonly referred to as a pentameric repeating unit or RU. Each RU composition has been given a unique label ranging from RU-A to RU-F. As the xanthan material retrieved from each strain might consist of a heterogeneous mix the different RUs, an overview of the different possible compositions per strain is listed in Table 5-1.
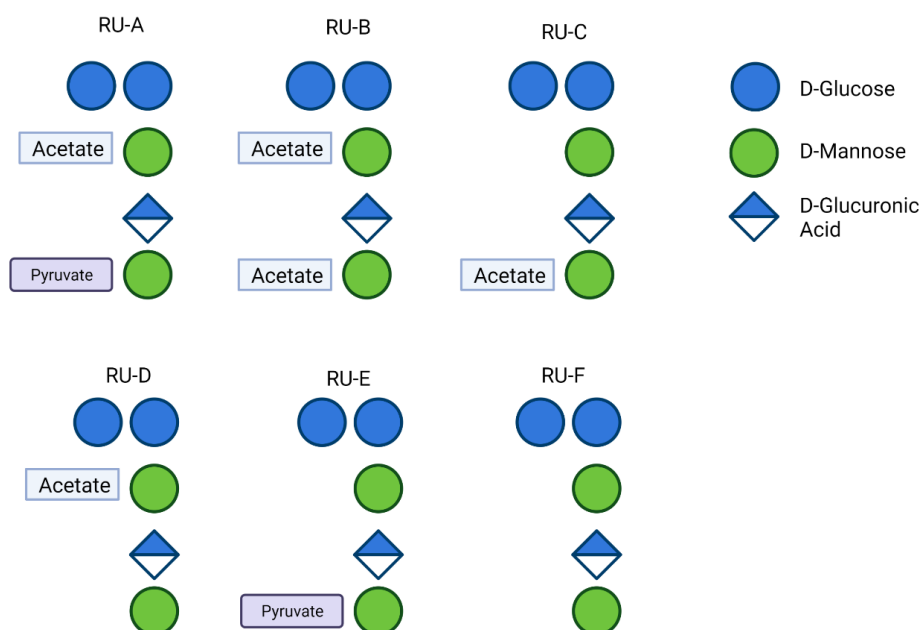
Figure 5-1 Diagrams showing an overview of the possible compositions of the repeating pentasaccharide unit (RU) in xanthan given a unique label each. Blue spheres are D-glucose, green spheres are D-mannose, and the white and blue diamond shapes are D-glucuronic acid. The acetates are O-6 linked, while the pyruvates are linked as diketal through O-4 and O-6.

Table 5-1 Different possible combinations of RUs per genetic variant.

	RU-A	RU-B	RU-C	RU-D	RU-E	RU-F
WS	x	x	x	x	x	x
ΔL	-	x	x	x	-	x
ΔFG	-	-	-	-	x	x
ΔFGL	-	-	-	-	-	x
ΔF	-	-	x	x	x	x
ΔG	x	-	-	x	x	x

5.1.2 Xanthan material yield

In Table 5-2, the yields of ΔL, ΔFG and ΔFGL are compared to the unmodified wildtype. The yields were estimated by comparing the weight of the solutions before the precipitation step in chapter 4.2.1 and the weight of the dried material before milling. All the modified variants had a lower yield compared to the wild type. A correlation between the theoretical maximum of the molecular weight per fully substituted RU (M_{RU}) (i.e., the largest average molecular weight possible of the genetic variant) and the yield compared to the wild type was found.

Table 5-2 Yield of ΔL, ΔFG and ΔFGL compared to the unmodified WS, based on weight of solution before precipitation and the dry weight . Theoretical maximum M_{RU} = the theoretically maximum molecular weight per fully substituted RU (i.e., the largest molecular weight possible of the genetic variant). Relative theoretical maximum M_{RU} (%) = the theoretical maximum M_{RU} compared to the wild type.

Sample	WS	ΔL	ΔFG	ΔFGL
Weight before precipitation (grams)	261.4	374.1	435.6	333.0
Dry weight (grams)	0.69	0.84	0.85	0.55
Percent (%)	0.27	0.22	0.19	0.17
Theoretical maximum M_{RU} (Da)	994.1	966.1	935.1	848.0
Relative theoretical maximum M_{RU} (%)	100.00	97.18	94.06	85.30
Yield compared to wild type (%)	100.00	84.40	73.20	62.70

5.1.3 Acetate and pyruvate content

The acetate and pyruvate content [mM] of each sample were estimated by Dr. Moritz Gansbiller and is presented in Table 5-4. The table showed that the acetate content varied between 0.18 and 13.02 [mM] while the pyruvate content varied between 0.04 and 6.63 [mM]. The method that was used to obtain the results is described in the article "In-depth rheological characterization of genetically modified xanthan variants" by Gansbiller et al. (2019).

Table 5-3 Acetate and pyruvate content [mM] of ΔF, ΔG, wild type, ΔL, ΔFG, and ΔFGL. The data was provided by Dr. Moritz Gansbiller who obtained the results as described in the article "In-depth rheological characterization of genetically modified xanthan variants" by Gansbiller et al. (2019).

Sample	Acetate [mM]	Pyruvate [mM]
ΔF	1.23	6.63
ΔG	7.47	6.27
Wild type	4.53	4.84
ΔL	13.02	0.04
ΔFG	0.18	4.84
ΔFGL	0.19	0.21

In Figure 5-2, the acetate pyruvate content from Table 5-3 is displayed in a bar chart. Both the figure and the table showed that only ΔFG, wild type, ΔG and ΔF had considerable amounts of pyruvate. The levels of pyruvate were increased in ΔG and ΔF compared to the wild type, while ΔFG had the same amount as the wild type. ΔFGL and ΔFG had no considerable amount of acetate. Compared to the wild type, ΔF had an almost 4-fold reduction in acetate while ΔL had an almost 3-fold increase in acetate. There was also a 1.6-fold increase in acetate in ΔG compared to the wild type.
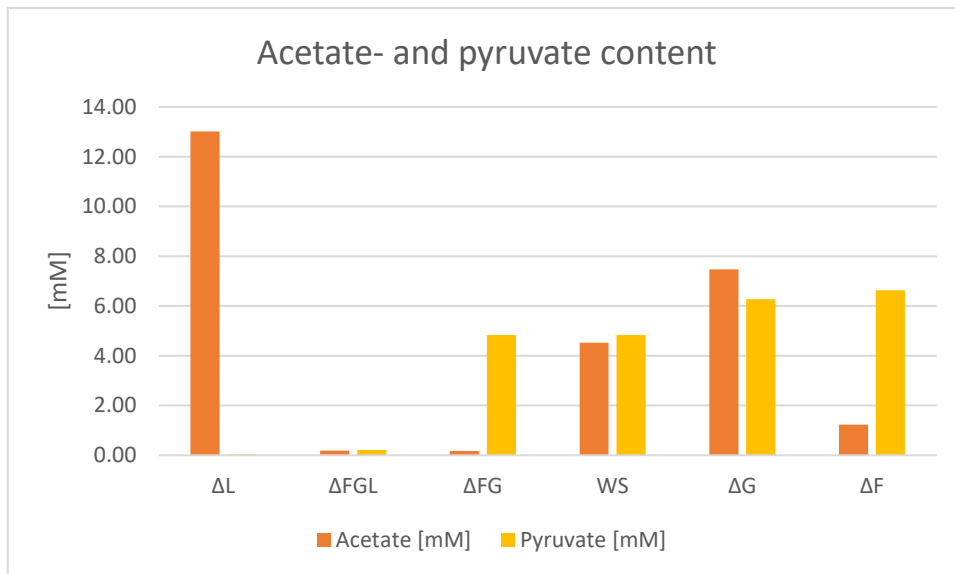
Figure 5-2 Acetate and pyruvate content [mM] of ΔF, ΔG, wild type, ΔL, ΔFG, and ΔFGL. Only four strains (ΔFG, wild type, ΔG and ΔF) had significant amounts of pyruvate. The levels of pyruvate were higher in ΔG and ΔF than in the wild type, while ΔFG had similar levels to the wild type. Neither ΔFGL nor ΔFG showed significant amounts of acetate. Compared to the wild type, strain ΔF showed a nearly 4-fold decrease in acetate levels while strain ΔL showed a nearly 3-fold increase. Strain ΔG showed a 1.6-fold increase in acetate levels compared to the wild type.

5.2 SEC-MALS results

The objective of performing SEC-MALS analysis on the xanthan material was to determine the final M_w and R_w after mechanical degradation. This section includes the results from SEC-MALS and a comparison of the conformational changes of the samples.

SEC-MALS analysis was performed on four parallels of four of the xanthan variants (WS, ΔL, ΔFG and ΔFGL) to determine the weight average molecular weight (M_w), weight average radius of gyration (R_w) and molecular weight distributions at 0, 1 (2), 5 and 10 cycles. One of these four xanthan variants (WS) could not be tested after the first cycle due to a sampling error and was therefore conducted after the second cycle (Table 5-5). When the final variants (ΔF and ΔG) arrived, the two final samples were only analyzed at the tenth cycle. The number of cycles was decided based on previous experiments done by Christian Holmvik (Holmvik, 2018) and Karina Gjerdevik Osebakken (Osebakken, 2019). They reported a stagnation or only minor changes in M_w after ten cycles of mechanical degradation for xanthan material (Osebakken, 2019, Holmvik, 2018). Only the results from the 25 µl injection are presented in this thesis.

The berry fit method with a fit degree of 2 was chosen and detector 5-15 was enabled for all the samples. The fit method and fit degree were chosen because the R_w was between 37 and 48 nm for all the samples.

5.2.1 Comparison of the samples

In Table 5-4, the weight-average molecular weight (M_w) of the tenth iteration of degradation ranged from 323.3 kDa and 619.5 kDa while the weight-average radius of gyration ranged from 37.0 nm to 46.3 nm is presented. All the samples had a much lower calculated mass than expected suggesting that some material was removed during the filtering in the preparation step (See chapter 4.2.2).

Table 5-4 Molecular weight-average, average radius of gyration and calculated mass of all samples after ten cycles of mechanical degradation in SEC-MALS buffer with cooling in ice bath between cycles.

Name	M_w (kDa)	Uncertainty	R_w (nm)	Calculated mass (µg)
WS	530.6	0.2%	41.2	7.41
ΔL	333.3	0.4%	46.3	8.64
ΔFG	619.5	0.3%	39.1	7.57
ΔFGL	477.2	0.3%	44.3	8.42
ΔF	323.3	0.2%	37.0	7.33
ΔG	325.7	0.3%	39.8	6.00

5.2.2   The effect of mechanical degradation of xanthan

All the first four xanthan variants showed a decrease in both M_w and R_w for each cycle, see Table 5-5. The decrease in M_w and R_w was largest after the first cycle and decreased less for each cycle. Even though the mechanical degradation consistently decreased the molecular weight of xanthan from approx. 3500-6700 kDa (at 0 cycles) to approx. 280-610 kDa (after 10 cycles), the first measurements at zero cycles were not considered reliable. This was due to SEC-MALS analysis not being well suited for extreme high molecular weight. Although a study by Gansbiller et al. (2019) have used similar techniques for molecular weight determination of similar samples, it was the general impression amongst the researchers giving the supervision and training on the SEC-MALS equipment that M_w- and R_w-results from high molecular xanthan are unreliable.

Table 5-5 Molecular weight-average, average radius of gyration and calculated mass of all samples after 0, 1 (2), 5 and 10 cycles of mechanical degradation in SEC-MALS buffer with cooling in ice bath between cycles.

	WS			ΔL			ΔFG			ΔFGL		
Cycles	M_w (kDa)	± %	R_w (nm)	M_w (kDa)	± %	R_w (nm)	M_w (kDa)	± %	R_w (nm)	M_w (kDa)	± %	R_w (nm)
0	4165.0	1.3	183.7	3330.8	0.7	140.6	4563.6	2.3	189.3	6379.7	1.3	208.6
1	-	-	-	809.0	0.4	76.8	1816.8	0.7	76.0	1023.7	0.5	74.0
2	1013.1	0.6	71.2	-	-	-	-	-	-	-	-	-
5	674.0	0.3	48.6	433.9	0.4	53.4	900.2	0.3	42.7	570.1	0.3	46.2
10	530.6	0.2	41.2	333.3	0.4	46.3	619.5	0.3	39.1	477.2	0.3	44.3

Figure 5-3 shows the results after SEC-MALS analysis of the ΔL sample after 0, 1, 5 and 10 cycles of mechanical degradation in a Wet Mill Jet Star Burst Mini homogenizer. The differential refractive index (dRI) is a signal that represents the mass distribution of the sample, which is represented by the dotted gaussian lines. The dRI signal got progressively narrower and the distribution was shifted to a higher elution volume with an increasing number of degradation cycles. Similar graphs of ΔL, ΔFG and ΔFGL can be found in Appendix G.

Also in Figure 5-3, a denser dashed line of greater line widths represents the development of the M_w. The M_w gets reduced, and the elution profile is more linearized with the increasing number of degradation cycles. The reduction and linearization are both greatest between 0 cycles and 1 cycle before the development seem to almost stagnate between 5 and 10 cycles. The mass distribution and M_w development was as expected for disperse high molecular weight polymers.
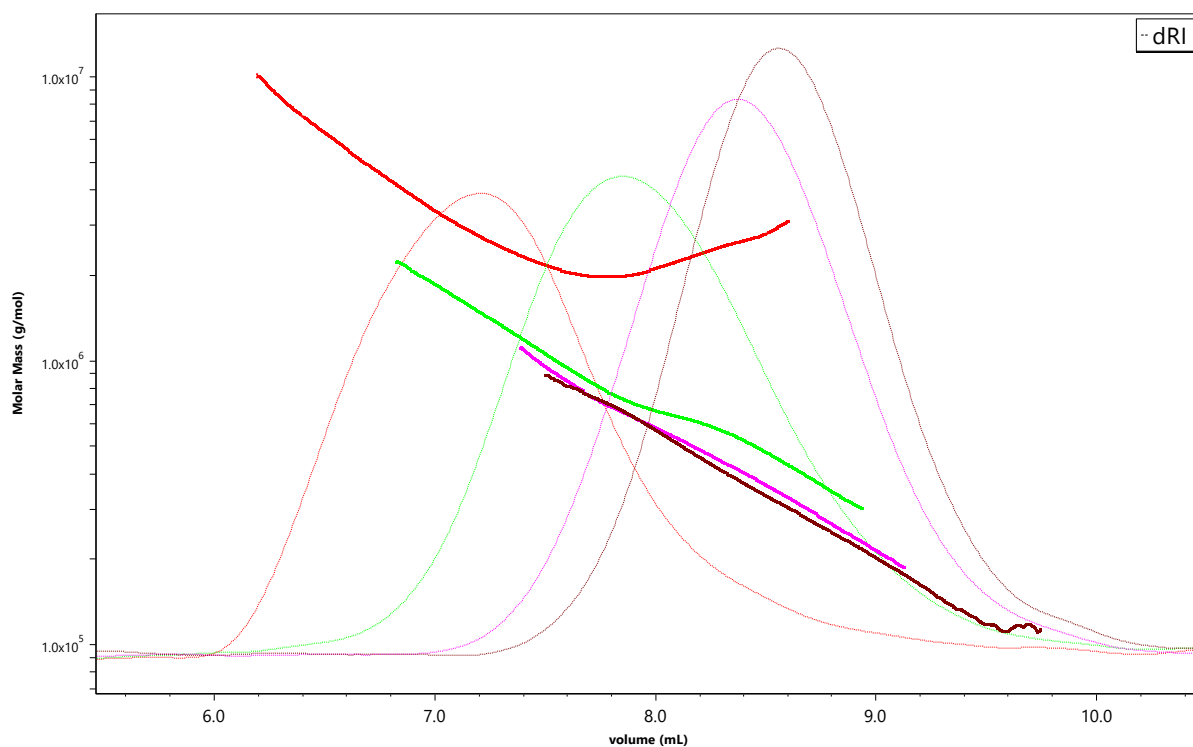
Figure 5-3 Molar mass distribution and refractive index changes for ΔL as a function of elution volume for zero (red), one (green), five (purple) and ten (black) cycles in the Wet Mill Jet Star Burst Mini homogenizer . The dashed line is the differential refractive index displaying the weight distribution becoming progressively narrower and moved to a higher elution volume. The denser dashed lines with greater line widths display the calculated weight-average molecular weight getting progressively lower and less disperse.

The weight-average molecular weight and mass distribution profiles of the samples after ten cycles were compared in Figure 5-4. ΔL, ΔFGL and ΔG had an M_w-profile with a linear decline throughout the elution volume. ΔF had a similar profile, but less linear. Linear elution profiles were expected of uncontaminated and non-aggregated samples. ΔFG and wild type had an irregular M_w-profile where the average showed both a decline and an incline throughout the elution.

Figure 5-5 showed that all the samples had a linear average radius of gyration trend throughout the elution volume after ten cycles of mechanical degradation. There was no correlation between the variations in M_w-profiles found in Figure 5-4 and the R_w-profiles in Figure 5-5.
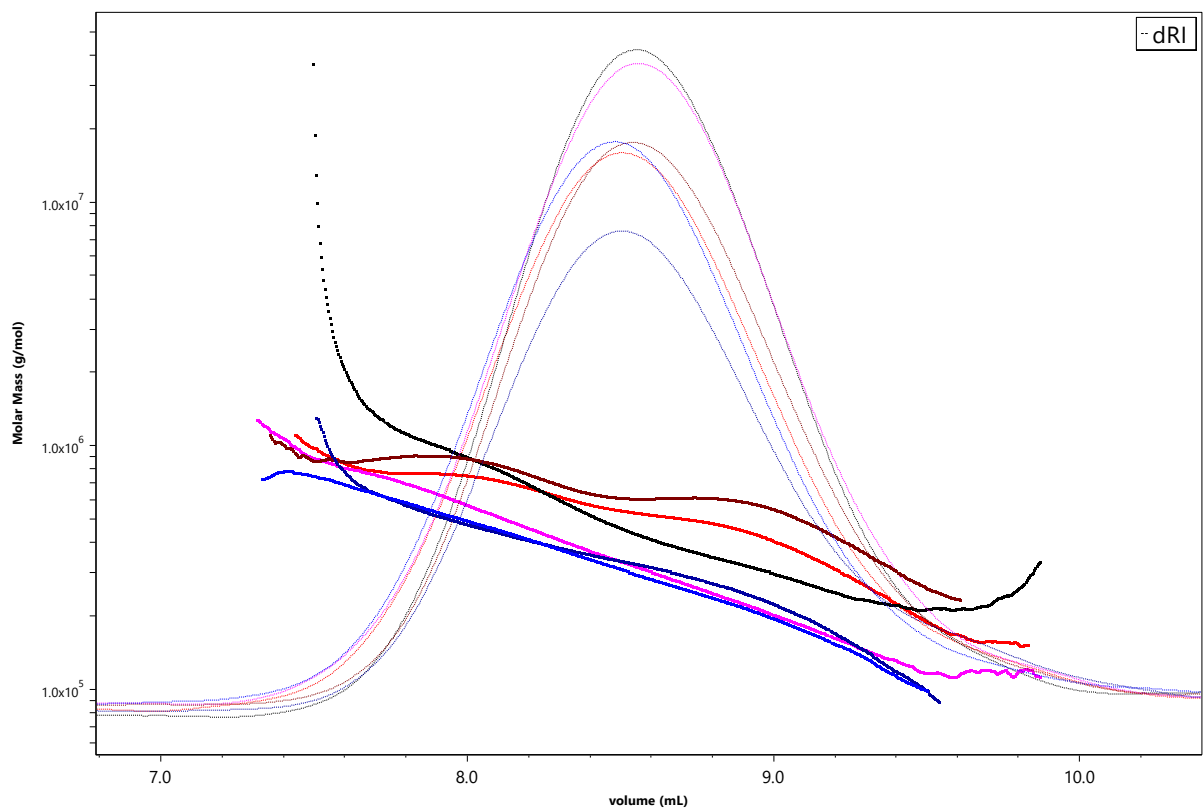
Figure 5-4 Molar mass distribution and refractive index changes for all the samples after ten cycles in a Wet Mill Jet Star Burst Mini homogenizer as a function of elution volume. The dashed line is the differential refractive index displaying the weight distribution being concentrated around the same elution volume, but with difference in total injected mass. The densely dashed line displays the calculated molecular weight and shows some irregularity amongst the samples. ΔL (pink), ΔFGL (black), ΔG (blue) and some extend ΔF (dark blue) as well shows the expected regularity with a somewhat straight line, whereas ΔFG (brown) and WS (red) behaves more unexpectedly with an irregular development throughout the elution.
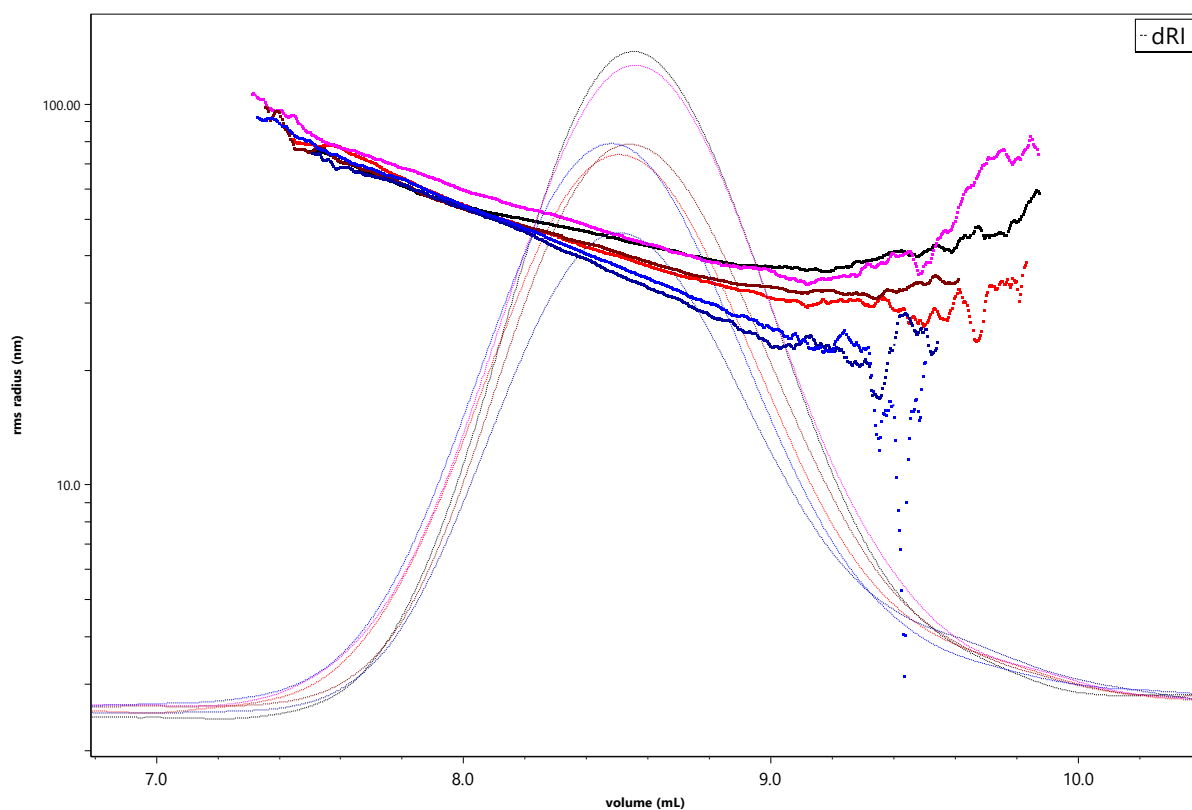
Figure 5-5 Weight-average radius of gyration and refractive index changes for all the samples after ten cycles in a Wet Mill Jet Star Burst Mini homogenizer as a function of elution volume. The dashed line is the differential refractive index displaying the weight distribution of the injected mass separated by a size exclusion chromatograph. The densely dashed line displays the calculated weight-average radius of gyration from static light scattering. All the samples: WS (red), ΔL (pink), ΔFG (brown), ΔFGL (black), ΔF (dark blue) and ΔG (blue) have linear elution profiles.

5.2.3 Stability experiment

The results from the stability experiment (Table 5-6) showed that the M_w varied between 323.7-567.8 kDa and the R_w varied between 34.5-48.7 nm. Compared to the standard (FA and GA), the M_w increased while the R_w decreased in the stabilized variants (FB and GB). The destabilized variants (FC and GC) got a slight increase in M_w and slightly greater increase in R_w. The calculated mass varied between 6.0 and 13.0 µg.

Table 5-6 SEC-MALS results from three parallels of both ΔF and ΔG with different mechanical degradation protocols.

Variant	M_w (kDa)	±	R_w (nm)	Calculated mass (µg)
Δ FA	323.7	0.2%	37.5	6.0
Δ FB	567.8	0.2%	34.5	9.5
Δ FC	359.0	0.3%	41.1	7.0
Δ GA	326.5	0.3%	40.8	7.3
Δ GB	415.2	0.2%	37.0	13.0
Δ GC	332.6	0.4%	48.7	8.3

Destabilizing ΔF (Figure 5-6) and ΔG (Figure 5-7) by not cooling the solutions down between cycles resulted in a weight distribution skewed toward a lower elution volume and less linear M_w elution profiles. The ΔF sample seemed to be more affected by the destabilization. The stabilized samples of ΔF (Figure 5-6) and ΔG (Figure 5-7) showed that higher ionic strength resulted in steeper M_w elution profiles while the weight distribution remained unchanged. A correlation between the linearity and steepness of the M_w elution profiles and the stability of the material was found.
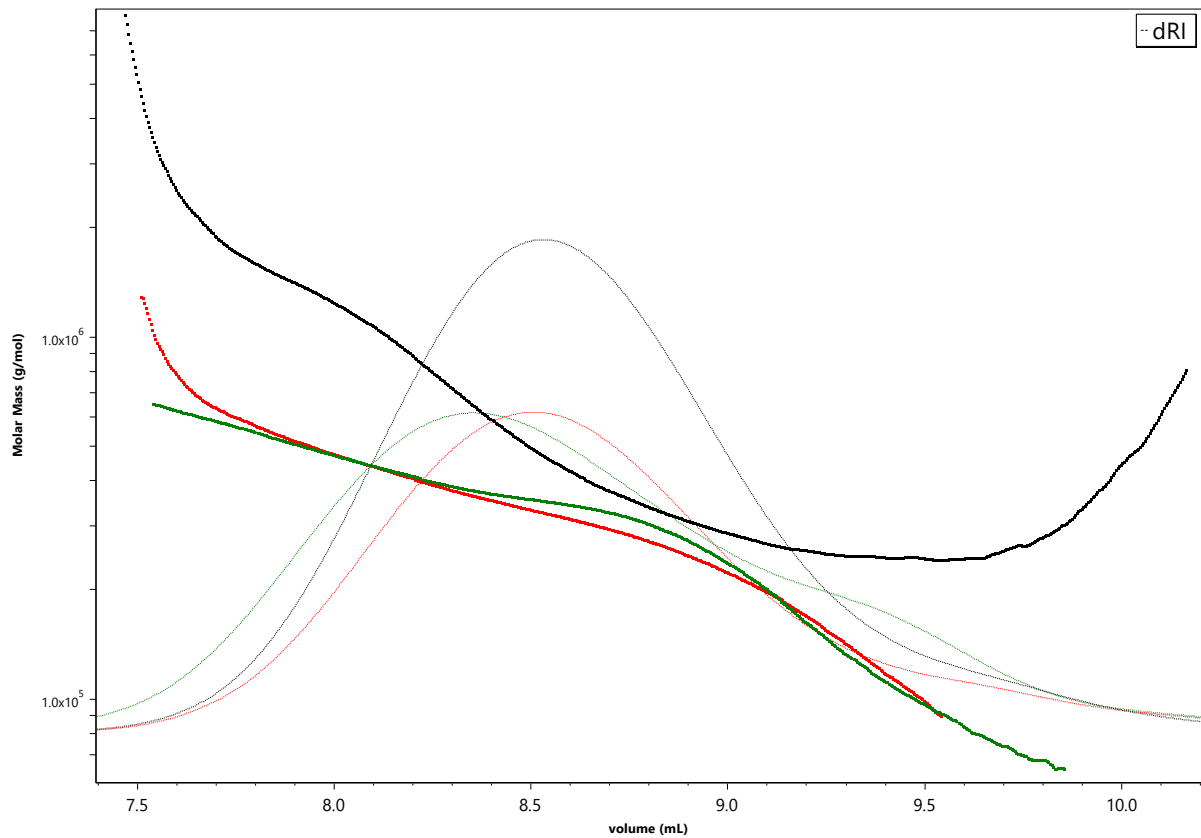
Figure 5-6 Molar mass distribution and refractive index changes for three different parallels of ΔF (A, B and C) after ten cycles in the Wet Mill Jet Star Burst Mini homogenizer as a function of elution volume. The dashed line is the differential refractive index displaying the weight distribution being concentrated around the same elution volume, but with difference in total injected mass. The densely dashed line displays the calculated molecular weight and shows some irregularity amongst the samples. ΔFA (red line) was processed using the standard protocol described in chapter 4.2.2 and shows an almost linear M_w elution, and a normal weight distribution. ΔFB (black line) was processed using a buffer with higher ionic strength (chapter 4.2.2.1) and shows a similarly linear but steeper M_w elution than ΔFA and a similar weight distribution. ΔFC (green line) was processed without cooling between cycles (chapter 4.2.2.1) and shows a less linear elution than ΔFA and a broader weight distribution that is skewed to a lower elution volume with a shoulder at the higher elution volume.
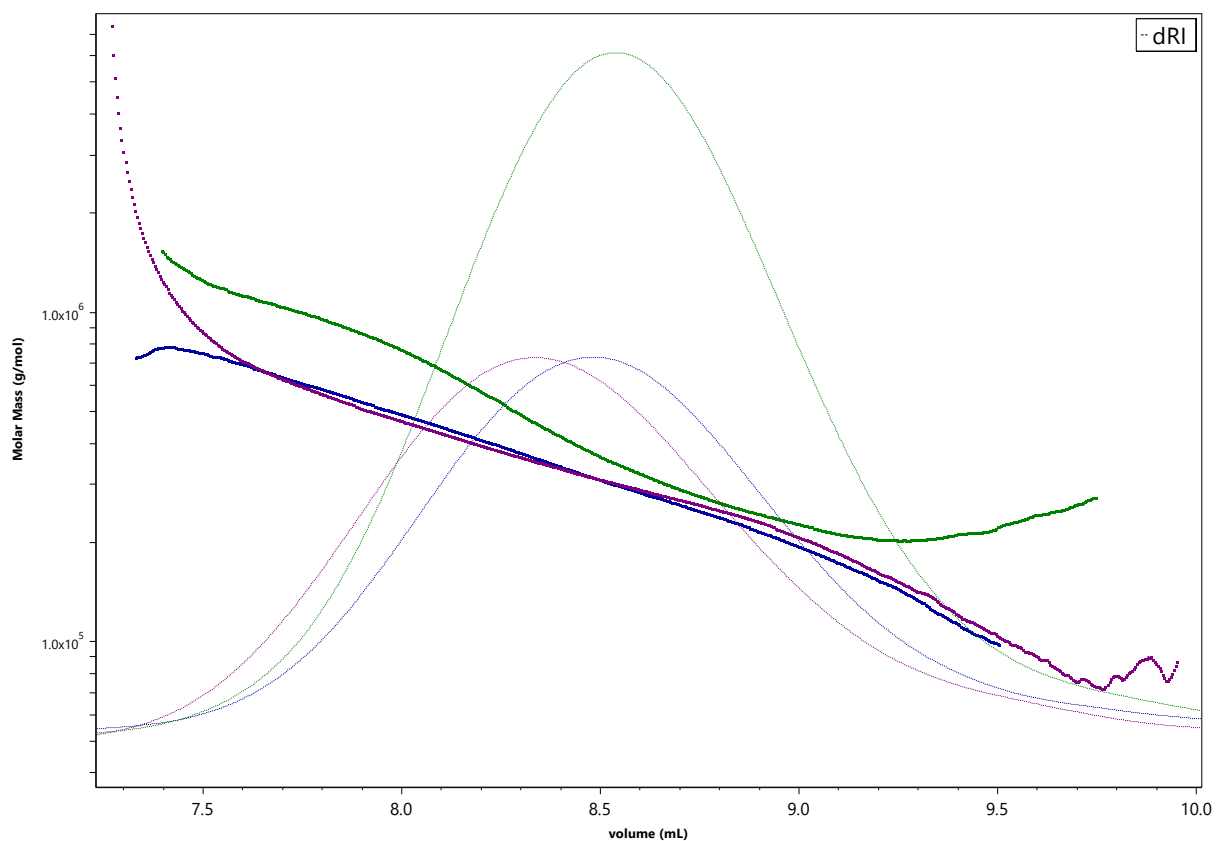
Figure 5-7 Molar mass distribution and refractive index changes for three different parallels of ΔG (A, B and C) after ten cycles in the StarBurst Mini homogenizer as a function of elution volume. The dashed line is the differential refractive index displaying the weight distribution being concentrated around the same elution volume, but with difference in total injected mass. The densely dashed line displays the calculated molecular weight and shows some irregularity amongst the samples. ΔGA (blue line) was processed using the standard protocol described in chapter 4.2.2 and shows an almost linear M_w elution, and a normal weight distribution. ΔGB (green line) was processed using a buffer with higher ionic strength (chapter 4.2.2.1) and shows a similarly linear but steeper M_w elution than ΔFA and a similar weight distribution. ΔFC (purple line) was processed without cooling between cycles (chapter 4.2.2.1) and shows a less linear elution than ΔFA and a broader weight distribution that is skewed to a lower elution volume.

5.2.4 The impurity experiment

The results from the impurity experiment (chapter 4.2.2.2) where wild type xanthan after nine cycles of mechanical degradation was compared to an equal sample that had been treated with active carbon to remove impurities yielded a M_w between 431.3-496.7 kDa and an R_w between 50.2-55.9 nm while the calculated mass was reduced by a 3-fold. Both the M_w and R_w increased after the active carbon treatment. However, the calculated mass was reduced drastically.

Table 5-7 SEC-MALS result from the impurity experiment where wild type xanthan after nine cycles of mechanical degradation was compared to equal sample that had been treated with active carbon. A.C. is short for active carbon.

	M_w (kDa)	±	R_w (nm)	±	Calculated mass (µg)
Wild type A.C. (Nine cycles)	496.7	0.4%	55.9	1.5%	4.76
Wild type (Nine cycles)	431.3	0.4%	50.2	1.8%	14.47

In Figure 5-8, SEC-MALS data of a wild type sample processed that had been mechanically degraded nine cycles (WTS) was compared to an equivalent wild type sample that had been treated with activated carbon (WTAC) as described in chapter 4.2.2.2. The wild type standard (WTS) showed a non-linear M_w elution, and a normal weight distribution. Wild type activated carbon (WTAC) showed an even more non-linear M_w elution than WTS and normal weight distribution of much lower injected mass that was slightly skewed towards a lower elution volume.
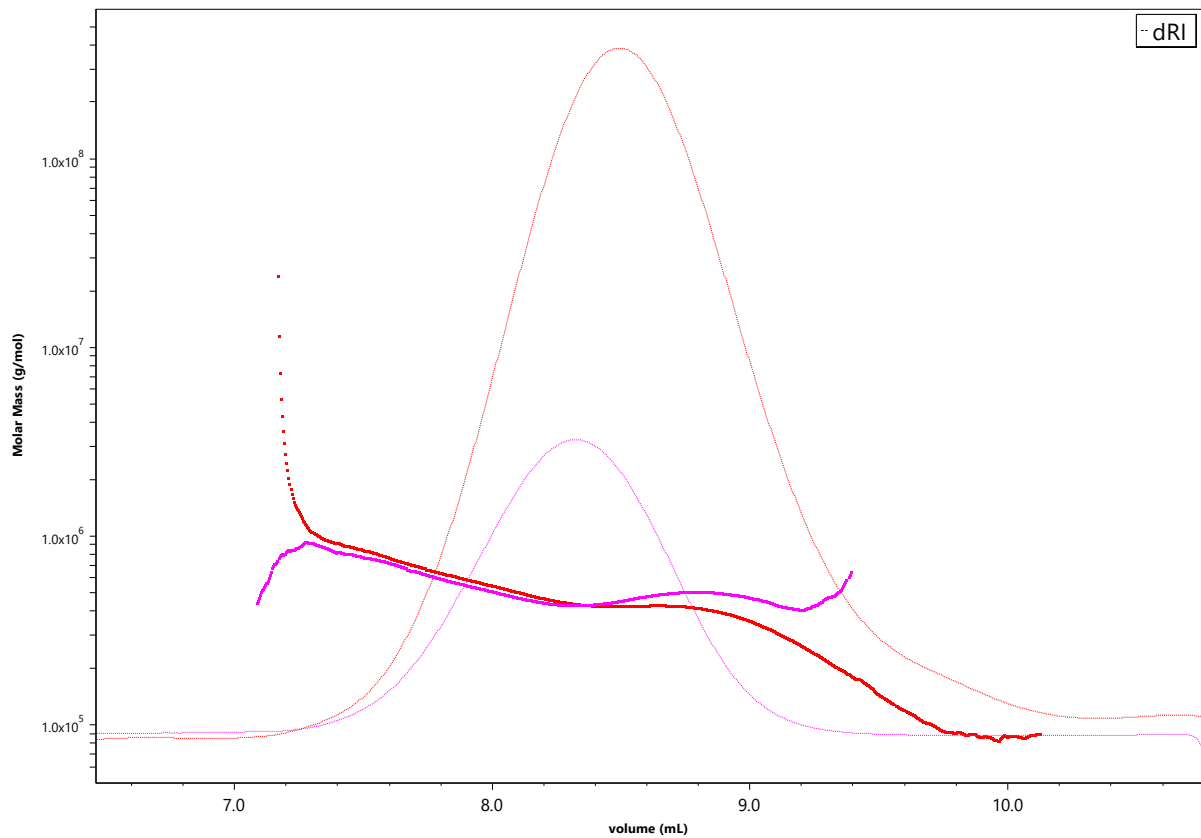
Figure 5-8 Molar mass distribution and refractive index changes for two different parallels of the wild type (wild type standard = red, wildtype activated carbon = purple) after nine cycles in the StarBurst Mini homogenizer as a function of elution volume. The dashed line is the differential refractive index displaying the weight distribution being concentrated around the same elution volume, but with difference in total injected mass. The densely dashed line displays the calculated molecular weight and shows some irregularity between the two samples. Wild type standard (WTS) was processed using the standard protocol described in chapter 4.2.2 and shows a non-linear M_w elution, and a normal weight distribution. Wild type activated carbon (WTAC) was treated with activated carbon (chapter 4.2.2.2) and shows an even more non-linear M_w elution than WTS and normal weight distribution of much lower injected mass that is slightly skewed towards a lower elution volume.

5.3 ¹H-NMR results

The objective of doing a series of ¹H-NMR measurements at increasing temperatures was to estimate and compare the T_m of the different mechanically degraded biotechnologically modified variants of xanthan.

Using the method described in chapter 4.2.5, melting curves from the anomeric proton of the α- and β-mannose as well as the available methyl peaks of the acetyl and pyruvyl substitutions were made for all the samples. However, the anomeric proton and acetyl and pyruvyl peaks of the ΔL and the acetyl and pyruvyl peaks had to be estimated based on the alternative method described in 4.2.5.

Before generating melting curves, reporter peaks had to be selected. A good T_m reporter must be a peak that is present in all the spectra that are analyzed, and it should also be easily isolated, meaning that it is not prone to overlapping with other signals. The peak should also have a narrow signal with a sigmoidal development in the selected temperature interval. Based on these criteria, the peaks from the anomeric proton of the α- and the β-mannose were used as reporters. Figure 5-9 shows a ¹H-NMR spectrum of the wild type measured at 363 K. The peaks were annotated based on literature and confirmed using 2D-NMR as described in chapter 5.4.
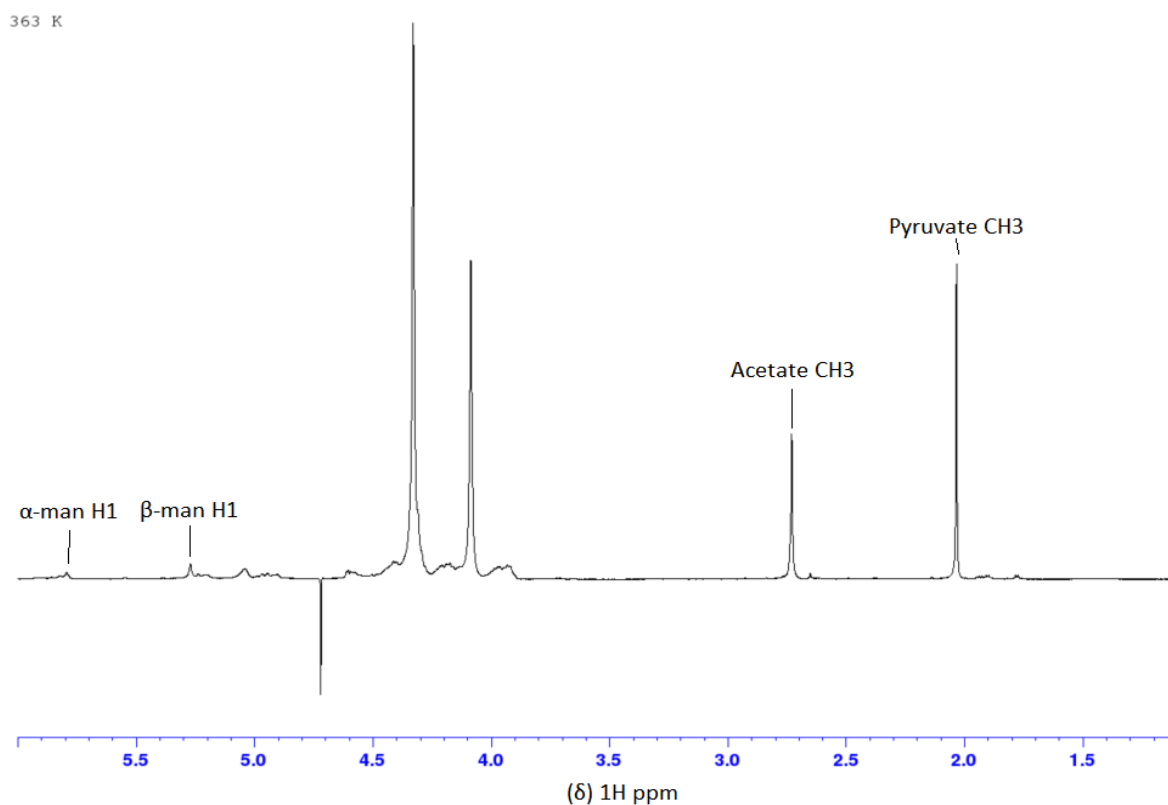
Figure 5-9 ¹H-NMR spectrum of the wild type at 363 K. The annotated peaks are the signals from the anomeric protons of the mannose and the methyl groups of acetyls and pyruvyl decorations. The two largest peaks are an unknown impurity in the sample. The negative peak between 5.0 and 4.5 ppm is a suppressed water peak.

Figure 5-10 is an overlay of an HSQC and ¹H-NMR spectra of the wild type in the region 5.39-4.39 Δ¹H ppm, 103.4-98.9 Δ¹³C ppm showing the anomeric proton signals. The anomeric proton of the β-mannose (BM1) overlapped with another anomeric proton (G/GA1.1). The anomeric protons of α- and

38

β-mannose (AM1 and BM1) and the unknown anomeric proton peaks (G/GA1.1, G/GA2.1 and G/GA3.1) are assigned in chapter 5.4. G/GA1.1, G/GA2.1 and G/GA3.1 are thought to be either from the glucose backbone or the glucuronic acid. The anomeric proton of the β-mannose (BM1) overlapped with another anomeric proton (G/GA1.1).
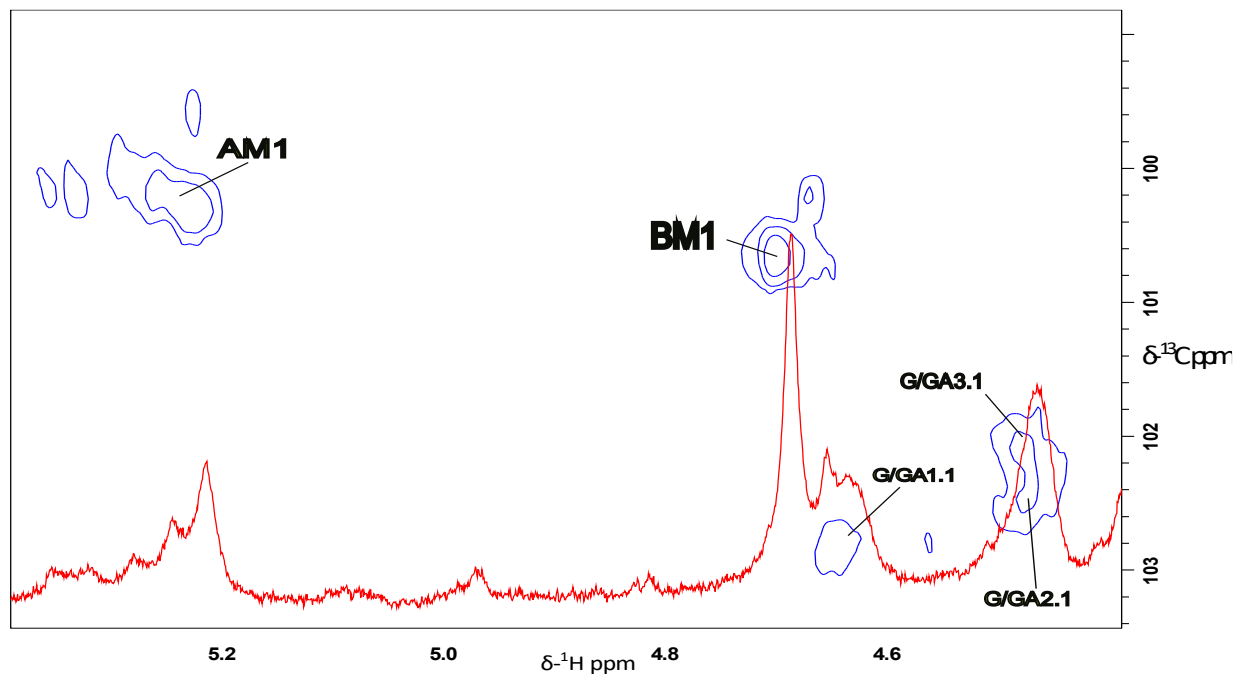
Figure 5-10 Overlay of a region (5.39-4.39 Δ^{1}H ppm, 103.4-98.9 Δ^{13}C ppm) of the HSQC (blue) and ^{1}H-NMR (red) spectra of WS. The anomeric proton of the α-mannose (AM1) was easy to isolate by selecting the entire peak on the ^{1}H-NMR spectrum, while the anomeric proton of the β-mannose peak overlapped with another anomeric proton peak (G/GA1.1) which made it impossible to isolate on ^{1}H-NMR. The annotations were made from 2D-NMR spectra as described in 5.4.

5.3.1 The effect of deacetylation and depyruvylation on melting temperature

To evaluate whether the anomeric proton peaks of the α- and β-mannose could be suitable for generating melting curves, both proton peaks on each spectrum were integrated and compared. In addition to this, the acetate and pyruvate peaks on ^{1}H spectra at each temperature were also integrated and analyzed. To summarize the results, the T_m values of all the selected peaks are represented in Table 5-8. Only WS, ΔL, ΔF and ΔG had an acetate methyl peak, while only WS, ΔFG, ΔF and ΔG had a pyruvate methyl peak.

*Table 5-8 Order-disorder mid-point transition values or melting temperatures (T_m) of all the samples based on both the anomeric protons of α and β-mannose and methyl peaks of the substitutions. Only WS, ΔL, ΔF and ΔG had an acetate methyl peak, while only WS, ΔFG, ΔF and ΔG had a pyruvate methyl peak. *The methyl T_m values of ΔL and ΔG, and the anomeric T_m values of ΔL could not be determined based on Equation 7 and had to be derived as described in chapter 4.2.5.*

	α-Man H1 T_m (°C)	β-Man H1 T_m (°C)	Acetate T_m (°C)	Pyruvate T_m (°C)
WS	68.0 ± 1.2	65.1 ± 0.5	62.9 ± 0.4	60.6 ± 0.7
ΔL	>= 85*	>= 85*	>= 85*	-
ΔFG	64.1 ± 1.7	61.5 ± 1.0	-	53.5 ± 0.6
ΔFGL	81.1 ± 1.0	81.4 ± 0.7	-	-
ΔF	67.6 ± 0.7	63.2 ± 0.6	63.0 ± 0.4	58.3 ± 0.7
ΔG	88.5 ± 4.7	86.6 ± 2.9	>= 85*	>= 85*

Figure 5-11 shows a side-by-side comparison of the T_m values of the anomeric protons of α- and β-mannose from each sample. The shaded bars extending in ΔL data illustrate that the melting temperature for this variant is at least 85 °C. The anomeric proton of β-mannose had a slightly lower (approx. 3°C) T_m than that of α-mannose in most samples, except for ΔFGL and ΔG, where the T_m values overlapped within the standard deviation range.
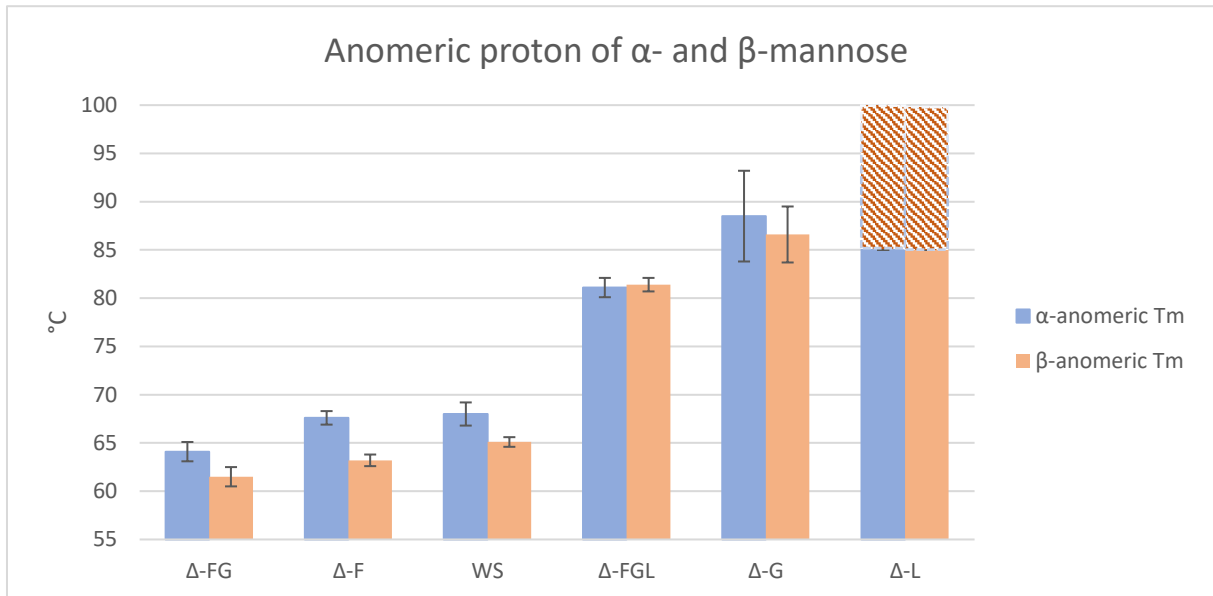
Figure 5-11 Comparison of the T_m values (°C) of the anomeric protons of α and β-mannose with error bars. The ΔL values are based on plotting the n-th discrete difference along the y-axis and choosing the tallest point. This means that it was only possible to determine that the melting temperature of ΔL could be greater than or equal to 85 °C.

The melting temperature of different variants of the polysaccharide was measured and compared with the wild type. The results showed that deleting the *gum*FGL, -G or -L residues increased the thermal stability of the polysaccharide, while deleting the *gum*F or -FG genes decreased it.

5.3.2 Comparing T_m with acetate- and pyruvate content and M_w

To assess the correlations between the T_m (retrieved from α-mannose H1) and other parameters such as acetate- and pyruvate content or M_w, two plots were made. In Figure 5-12, a diagram comparing T_m (Table 5-8) and M_w (Table 5-4) indicated no correlation between the two. Figure 5-13 showed a comparison of T_m (Table 5-8) and acetate- and pyruvate content (Figure 5-2) which indicated a correlation between low T_m with low acetate- to pyruvate content ratio and high T_m with a high acetate- to pyruvate content ratio. The bars of Δ-L goes to 100 °C in both Figure 5-12 and Figure 5-13, however they should just show that it is atleast 85 °C like in Figure 5-11.
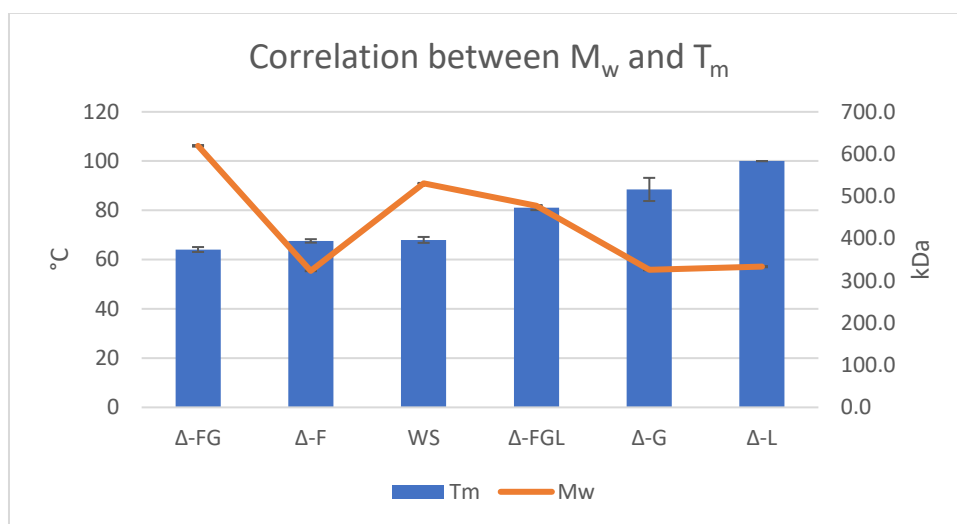
Figure 5-12 Simple diagram comparing the T_m (blue bars) and M_w (orange lines) of ΔFG, ΔF, wild type, ΔFGL, ΔG and ΔF. No correlation between T_m and M_w was found. The bar of Δ-L goes to 100 °C, however it should just show that it is atleast 85 °C like in Figure 5-11.
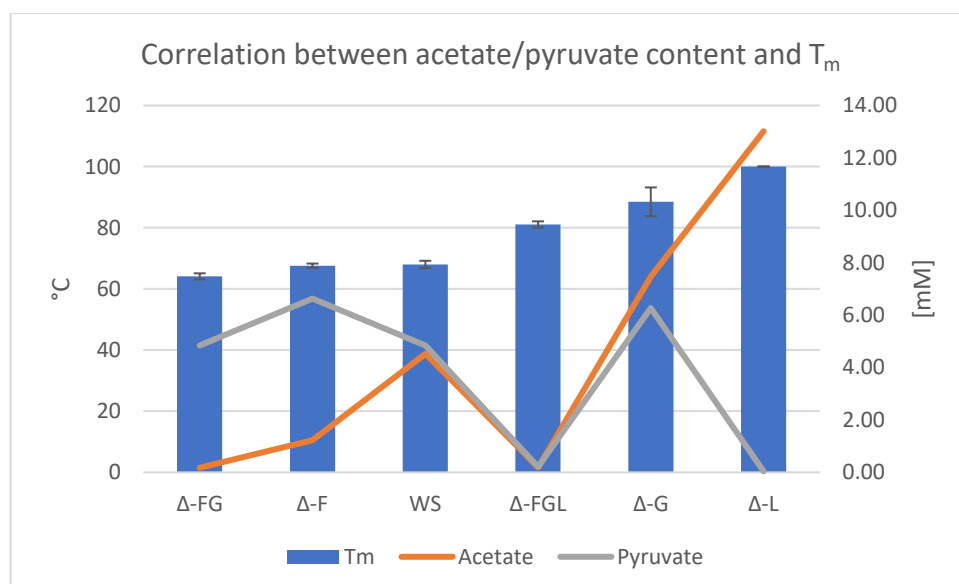
Figure 5-13 Simple diagram comparing the Tm (blue bars), acetate- and pyruvate content (orange and grey lines respectively) of ΔFG, ΔF, wild type, ΔFGL, ΔG and ΔF. Compared to the wild type, a low ratio between acetate- and pyruvate content correlated with lower Tm values, while high acetate compared to low pyruvate content correlated with higher Tm values. Removing both substituents increased the Tm. The bar of Δ-L goes to 100 °C, however it should just show that it is atleast 85 °C like in Figure 5-11

5.3.3 Measuring acetate and pyruvate content with ^{1}H-NMR

The degree of pyruvate and acetate substitution (DS_{Pyr} and DS_{Ac}) of the wild type xanthan sample was estimated by comparing the integrals of the pyruvate and acetate peak and the α-anomeric proton of the ^{1}H-spectrum at 363 K and compared with their respective theoretical maximum values of DS in Table 5-9. The rationale behind this method is that the integrals of the α-anomeric proton and the substitution peak would be perfectly correlated if the side chains had the maximum theoretical degree of substitution (DS). Since the pyruvate and acetate peak is a methyl group each containing three equivalent protons, they would each have three times the intensity and a 1:3 intensity ratio with the α-anomeric proton. Since there is only one possible position of pyruvate for each RU, the maximum DS_{Pyr} would be 1.0, meaning that 100 % of the side chains are pyruvylated. There are however two possible positions for acetate on the side chain meaning that the maximum DS_{Ac} would be 2.0, meaning that all the side chains have two acetate each. Since the pyruvate and acetate are competing for the position on β-mannose, the sum of DS_{Pyr} and DS_{Ac} can exceed 2.0.

*Table 5-9 Degree of acetate and pyruvate substitution calculated using ^{1}H-NMR for each sample. $DS_{Ac,sample}$ = Degree of acetyl substitution, $DS_{Pyr,sample}$ = Degree of pyruvyl substitution, DS_{Ac} (max) = theoretical maximum of degree of acetyl substitution, DS_{Pyr} (max) = theoretical maximum of degree of pyruvyl substitution, $\sum DS_{Ac,Pyr}$ (max) = theoretical maximum of the sum of DS_{Pyr} and DS_{Ac}, $\sum DS_{Ac,Pyr,sample}$ sum of $DS_{Ac,sample}$ and $DS_{Pyr,sample}$. *Value exceeding the theoretical maximum.*

	WS	ΔL	ΔFG	ΔFGL	ΔF	ΔG
DS_{Ac} (max)	2.0	2.0	1.0	0.0	1.0	1.0
DS_{Pyr} (max)	1.0	0.0	1.0	0.0	1.0	1.0
$\sum DS_{Ac,Pyr}$ (max)	2.0	2.0	2.0	0.0	1.0	2.0
$DS_{Ac,sample}$	1.4	2.8*	0.0	0.0	0.2	1.3
$DS_{Pyr,sample}$	1.9*	0.0	1.9*	0.0	1.8*	1.6*
$\sum DS_{Ac,Pyr,sample}$	3.3*	2.8*	1.9*	0.0	2.0	2.9*

By dividing the integral of the pyruvate peak by three and comparing it with the integral of the (α)-anomeric proton of WS, the DS was found to be around 188 % pyruvylation (Table 5-9). This is, as explained in the previous paragraph, not possible since it exceeds the theoretical maximum and there are many other examples of DS-values exceeding the theoretical maximum in the same table. Causes for this are considered in the Discussion (chapter 6.3.5).

5.4   2D-NMR results

As a part of the characterization of the biotechnologically modified xanthan material, an attempt to elucidate the structures of the different variants after mechanical degradation was done by a combination of HSQC, H2BC and HMBC measurements at high temperature (355 K). The aim of the 2D-NMR assignment was to confirm the identities of the reporter signals used for calculating melting curves.

The 2D-spectra of all the samples that were analyzed in this study can be found in Appendix F. Chapter 4.2.4 presents the types of 2D-NMR experiments that were acquired for each sample in Table 4-3. The results of the 2D-NMR analysis of the wild type spectra (HSQC, HMBC and H2BC), ΔFGL spectra (HSQC and HMBC) and parts of the HSQC spectra from ΔF and ΔL are discussed in detail in the following sections.

Firstly, the wild type (WS) was chosen as the target of the assignment strategy described in chapter 4.2.6. After the β-mannose spin system was found and no other complete systems could be assigned in the wild type spectrum, a similar approach was used for the ΔFGL, ΔF, ΔG and ΔL variants to find spin systems that could not be directly assigned in the spectra for the WS variant.

Because the wild type material could contain all the possible RUs (Figure 5-1) there could be both substituted and non-substituted ring carbons on the WS spectrum. Including all the possible combinations of substitution levels there could be a total of eight spin systems in the WS-spectrum as seen in Table 5-10.

Table 5-10 Representation of the different combinations of substituents that could be found in the WS-spectrum.

Monomer	Substitution
α-D-mannose	No substituent
α-D-mannose	Acetyl
β-D-mannose	No substituent
β-D-mannose	Acetyl
β-D-mannose	Pyruvyl
Glucose	No substituent
Glucose	Trimeric side chain
Glucuronic acid	No substituent

5.4.1   WS – Spin system

In Figure 5-14, a partial assignment of the wild type is shown on a triple overlay of wild type HSQC, HMBC and H2BC spectra. A complete spin system assigned to be the pyruvylated β-mannose (BMP, i.e., β-mannose pyruvylated) is annotated. The figure shows a consecutive correlation pattern between the HSQC, H2BC and HMBC spectra from BMP1-BMP2-BMP3-BMP4-BMP5-BMP6a/BMP6b-quaternary carbon and methyl pyruvate peaks. The H6-C6 HSQC-peak is split into two peaks (BMP6a and BMP6b) because the two protons (CH_2) are diastereotopic. No HSQC-peak of the pyruvate quaternary carbon (C7) was identified because it does not have a proton. However, it should theoretically have both a three-bond correlation to the H4 and H6 as described in appendix D. Only the three-bond correlation to the H6 could be seen in Figure 5-14.

A zoomed in version with a step-by-step description of the assignment process can be found in the appendix D. Also in Figure 5-14, many other unidentified peaks can be seen. These are described in chapter 5.4.4.
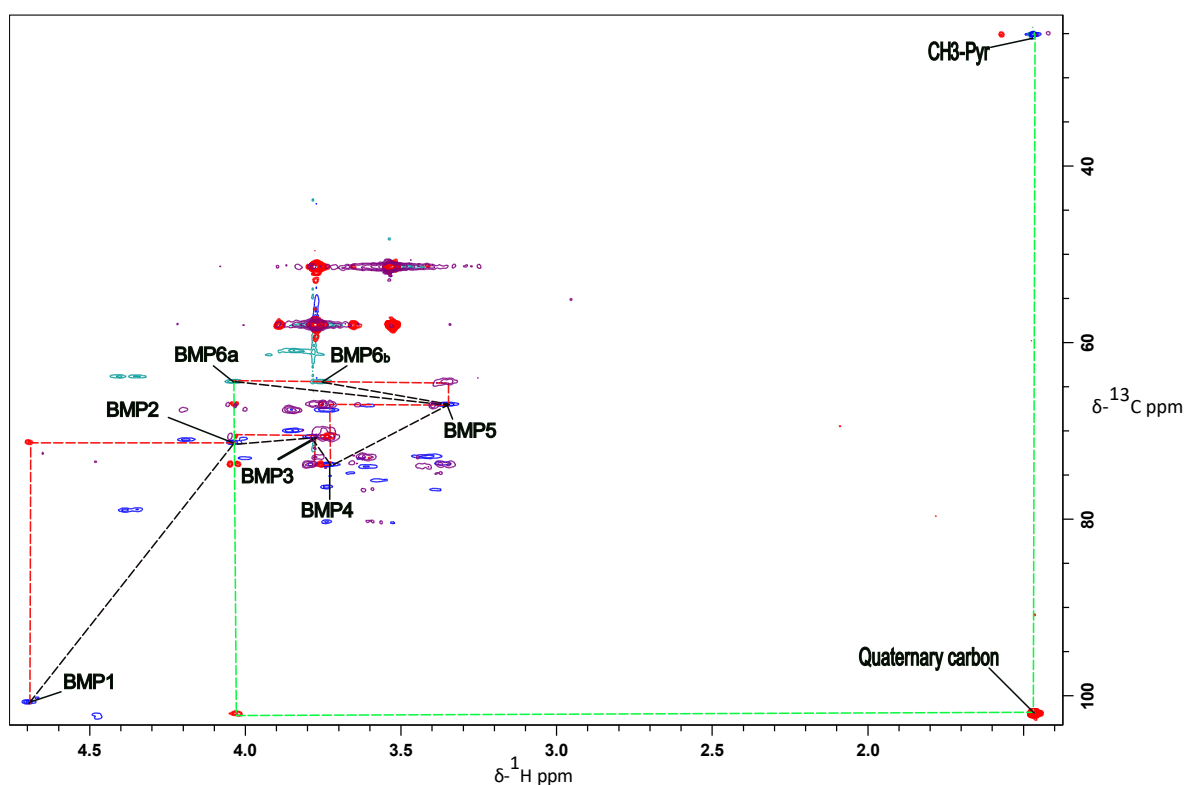
Figure 5-14 Overlay of HSQC, HMBC and H2BC spectra (4.77-1.40 δ ^{1}H ppm, 104.1-23.4 δ ^{13}C ppm) of wild type xanthan showing a spin system connected to pyruvate methyl peak. The spectra show CH1 and CH3 peaks (Blue), CH2 peaks (Green), HMBC peaks (Red) and H2BC peaks (Purple). The dashed red lines show how HSQC peaks are correlated by either HMBC, H2BC or both. The black dashed lines show the direction of the correlation to make it easier to read. The dashed green line shows the HMBC-correlation between the H6 and the methyl group of the pyruvyl through a non-protonated carbon as explained in appendix D. The illustration shows a consecutive correlation from BMP1-BMP2-BMP3-BMP4-BMP5-BMP6a/BMP6b-quaternary carbon and methyl pyruvyl peaks. BMP(#) is short for "β-mannose pyruvylated" and shows their assumed position in the carbon rings by their representative number.

5.4.2 ΔFGL- Spin systems

Two complete spin systems were found from analyzing the HSQC and HMBC spectra of ΔFGL. The two spin systems were assumed to be the non-substituted α- and β-mannoses. Figure 5-15 and Figure 5-16 shows an overlay of the HSQC- and HMBC-spectra with the spin systems annotated. Figure 5-15 shows an annotation of the assumed non-substituted α-mannose and the consecutive correlation pattern from AMNS1-AMNS2-AMNS3-AMNS4-AMNS5-AMNS6a/AMNS6b. Figure 5-16 shows an annotation of the assumed non-substituted β-mannose and the consecutive correlation pattern from BMNS1-BMNS2-BMNS3-BMNS4-BMNS5-BMNS6a/BMNS6b. Just as Figure 5-14, the H6 peaks in both spins systems are split.

The rest of the ΔFGL spectrum was analyzed further to find more correlating paths that could indicate more complete spin systems. However, the remaining peaks could not be connected into new complete spins systems. Six peaks assumed to be the anomeric protons of the glucuronic acid and glucose (with and without the side chain) and their corresponding H2-C2 peaks were assigned (Figure 5-17). In Figure 5-18, two more peaks were assigned to the H6-C6 of the glucose molecules in the backbone structure.
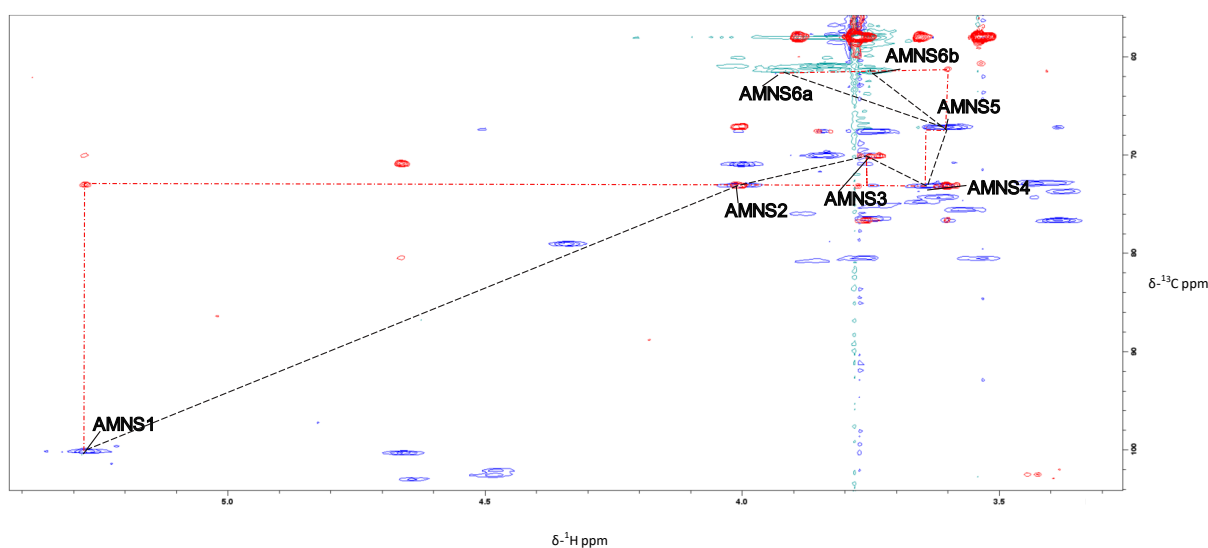
Figure 5-15 Overlay of HSQC- and HMBC-spectra (5.42-3.3 δ ^{1}H ppm, 103.5-57.8 δ ^{13}C ppm) of Δ-FGL showing a spin system from the assumed anomeric proton of the α-mannose. The spectra show CH1 and CH3 peaks (Blue), CH2 peaks (Green) and HMBC peaks (Red). The dashed red lines show how HSQC peaks are correlated by either HMBC, H2BC or both. The black dashed lines show the direction of the correlation to make it easier to read. The illustration shows a consecutive correlation from AMNS1-AMNS2-AMNS3-AMNS4-AMNS5-AMNS6a/AMNS6b. AMNS(#) is short for "α-mannose non-substituted" and shows their assumed position in the carbon rings by their representative number.
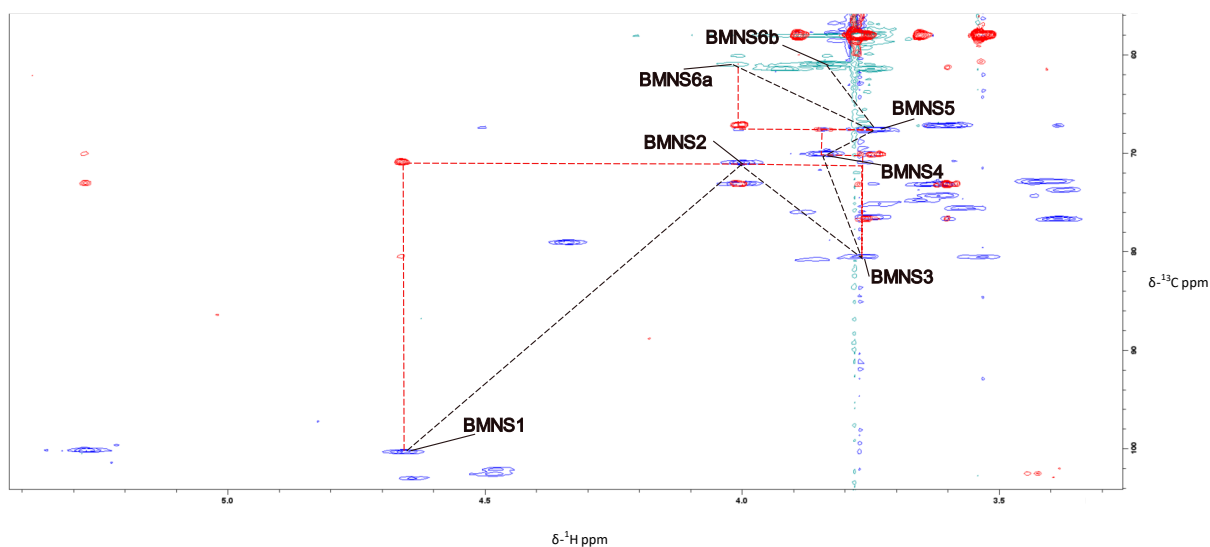
Figure 5-16 Overlay of HSQC- and HMBC-spectra (5.42-3.3 δ ^{1}H ppm, 103.5-57.8 δ ^{13}C ppm) of Δ-FGL showing a spin system from the assumed anomeric proton of the α-mannose. The spectra show CH1 and CH3 peaks (Blue), CH2 peaks (Green) and HMBC peaks (Red). The dashed red lines show how HSQC peaks are correlated by either HMBC, H2BC or both. The black dashed lines show the direction of the correlation to make it easier to read. The illustration shows a consecutive correlation from BMNS1- BMNS2-BMNS3-BMNS4-BMNS5-BMNS6a/BMNS6b. BMNS(#) is short for "β-mannose non-substituted" and shows their assumed position in the carbon rings by their representative number.
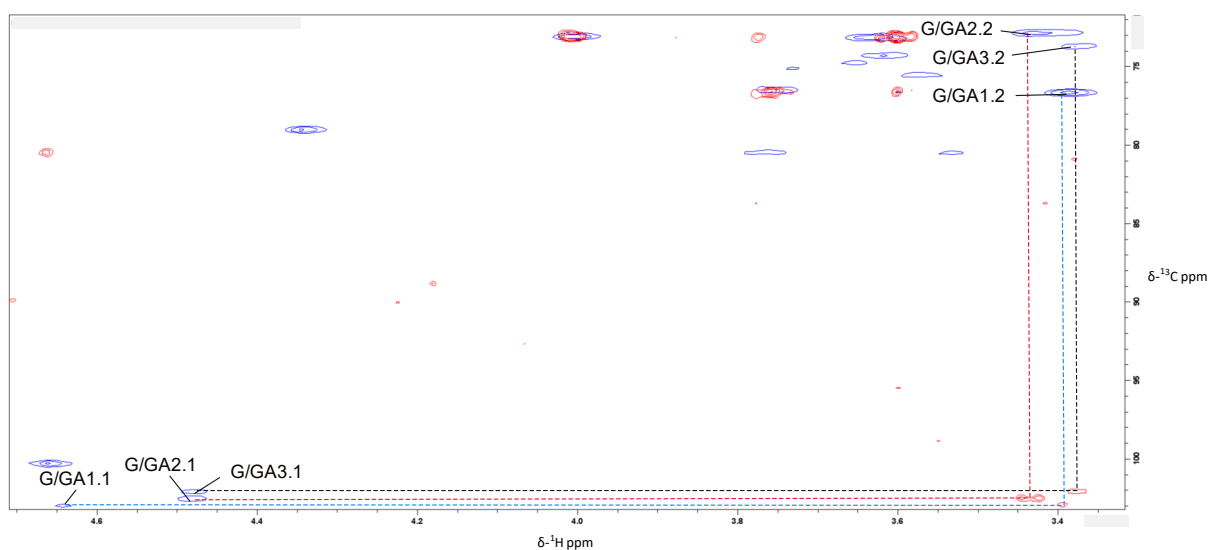
Figure 5-17 Overlay of HSQC- and HMBC-spectra (4.70-3.31 δ ^{1}H ppm, 104.1-70.5 δ ^{13}C ppm) of Δ-FGL showing three anomeric proton peaks and their respective H2/C2 peaks. The spectra show CH1 and CH3 peaks (Blue) and HMBC peaks (Red). The dashed red/blue/black lines show how the HSQC peaks are correlated through HMBC peaks. G/GA(#) is short for "Glucose or Glucuronic acid" while the number is the unique label followed by the assumed position in the carbon rings.
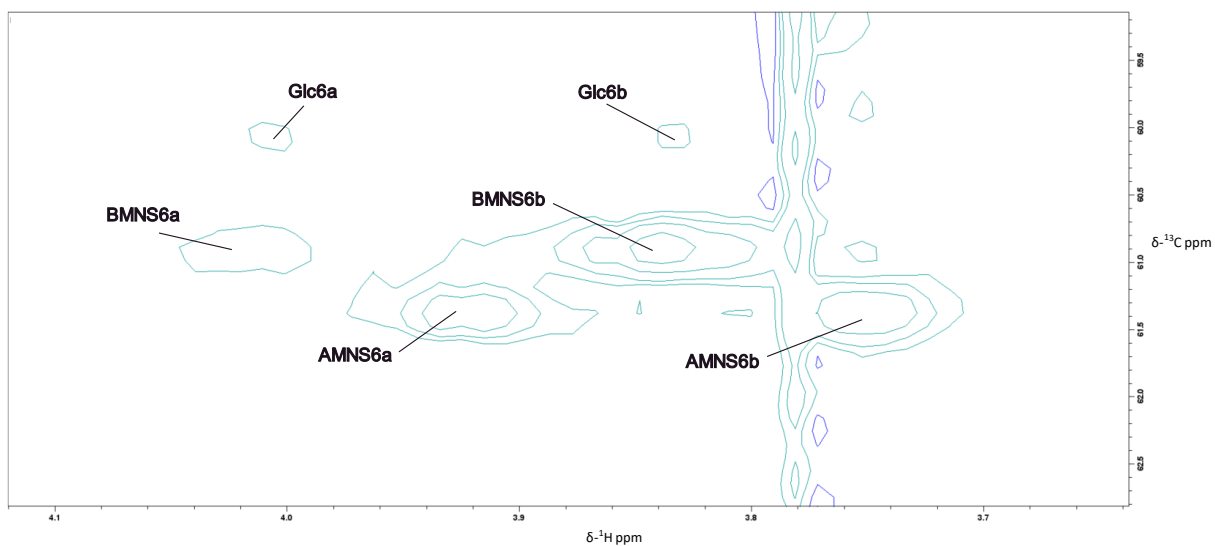
Figure 5-18 HSQC spectrum of Δ-FGL in region 4.11-3.65 δ ^{1}H ppm and 63.2-59.0 δ ^{13}C ppm showing the H6-C6 CH2 peaks (green). The BMNS6a/b- and AMNS6a/b-peaks were assigned in Figure 5-15 and Figure 5-16, while the Glc6a/b peaks were deduced based on the structure of xanthan.

5.4.3   Partial annotation of the wild type HSQC-spectrum

In Figure 5-19, an overlay the HSQC spectra of both Δ-FGL and wild type showed that the peaks of the complete and partial spin systems from chapter 5.4.2 overlapped corresponding peaks in the wild type spectrum.
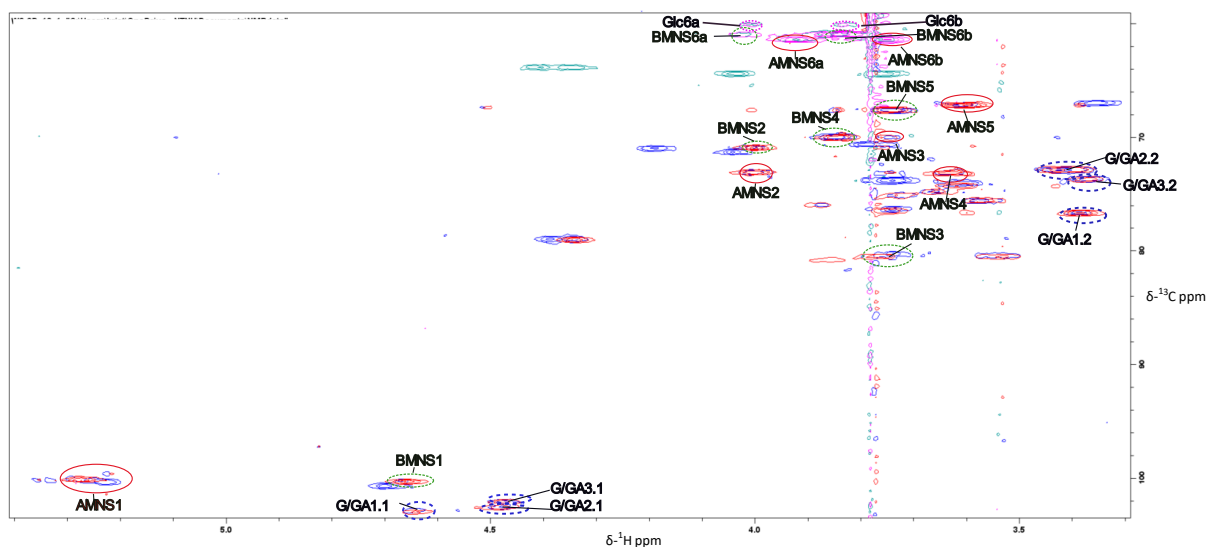
Figure 5-19 Overlay of Δ-FGL and wild type HSQC-spectra (5.42-3.3 δ ^{1}H ppm, 103.5-57.8 ^{13}Cppm) showing peaks from AMNS-spin system (red circles), BMNS-spin system (green dashed circles), G/GA partial spin systems (blue dashed circles) and Glc6 (pink dashed circles) from chapter 5.4.2 overlapping peaks in the wild type HSQC-spectrum. In the wild type spectrum, the CH1 and CH3 peaks appear blue while the CH2-peaks appear green. In the Δ-FGL spectrum, the CH1 and CH3 peaks appear red while the CH2-peaks appear purple.

A cluster of four peaks in the ^{1}H region 4.69-4.13 ppm and ^{13}C region 65.6-62.2 ppm was only visible in a triple overlay of the HSQC spectra of ΔL, ΔF and WS (Figure 5-20). The cluster consisted of two split H6-C6 peaks, AMA6a/b (α-mannose acetylated 6a and 6b) and BMA6a/b (β-mannose acetylated 6a and 6b). AMA6a/b was only present on the wild type and ΔL, while BMA6a/b was present on all three spectra.
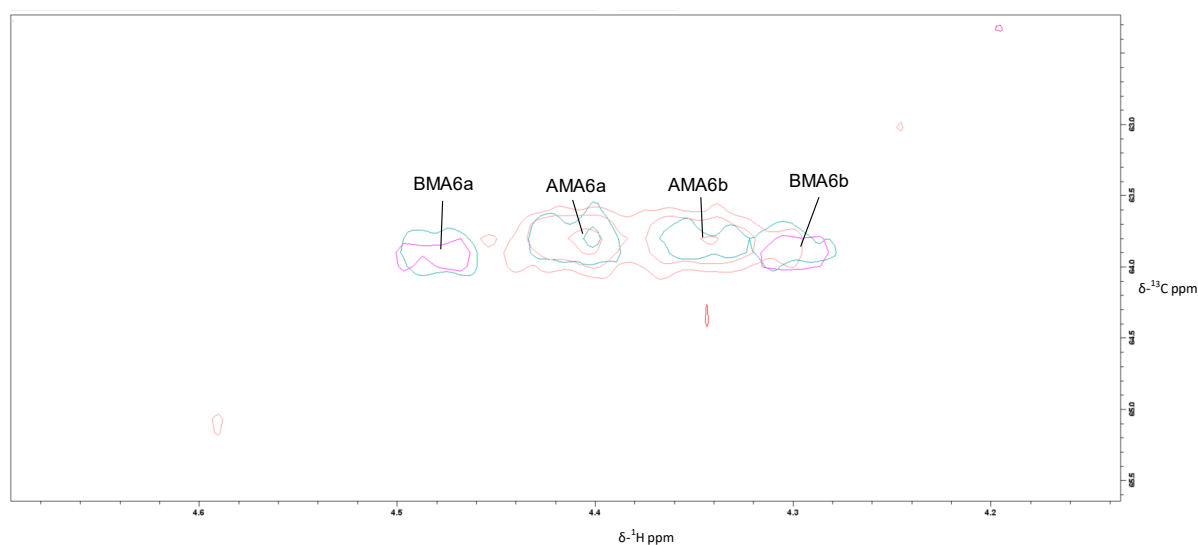
Figure 5-20 Overlay of the HSQC-spectra of wild type (orange), Δ-F (purple) and Δ-L (green) in the region 4.69-4.13 δ ^{1}H ppm and 65.6-62.2 δ ^{13}C ppm showing a cluster of four peaks thought to be acetylated H6-C6-mannose-

49

peaks. All the spectra had a signal at the BMA6a/b, only the wild type and Δ-L spectra had AMA6a/b. BMA and AMA is short for β-mannose acetylated and α-mannose acetylated. The signals are split due to being diastereotopic.

Figure 5-21 shows an HSQC spectrum of the wild type in the region 5.42-3.3 δ ^{1}H ppm, 103.5-57.8 δ ^{13}C ppm where the complete spins system (AMNS, BMNS and BMP) and partial spin systems (AMA6a/b, BMA6a/b, G/GA1, G/GA2, G/GA3 and Glc6a/b) that were identified in this project are assigned in one illustration.
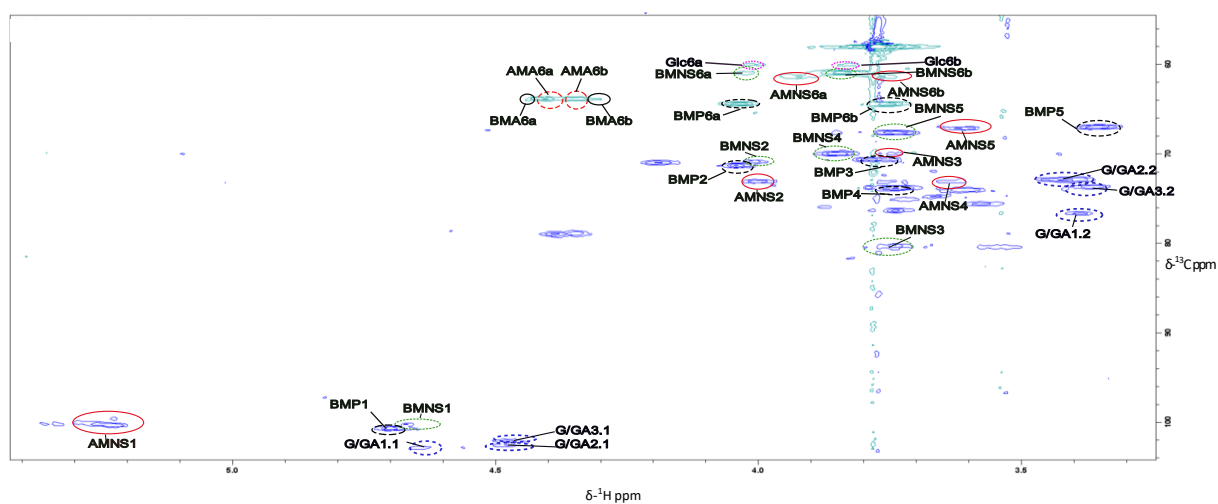
Figure 5-21 Indirectly assigned wild type HSQC-spectrum (5.42-3.3 δ ^{1}H ppm, 103.5-57.8 δ ^{13}C ppm. The methyl groups of pyruvyl and acetate are excluded in this figure.

Table 5-11 shows all the chemical shifts (δ ^{1}H and δ ^{13}C) of the assigned wild spectrum in Figure 5-21.

Table 5-11 Chemical shifts of the partially assigned HSQC-spectrum.

Peak name	δ ^{1}H [ppm]	δ ^{13}C [ppm]
AMNS1	5.23	100.4
AMNS2	4.00	73.1
AMNS3	3.75	69.9
AMNS4	3.63	73.1
AMNS5	3.61	67.1
AMNS6a	3.93	61.3
AMNS6b	3.75	61.3
BMNS1	4.67	100.0
BMNS2	4.00	70.8
BMNS3	3.74	80.3
BMNS4	3.85	70.0
BMNS5	3.74	67.6
BMNS6a	4.02	61.0
BMNS6b	3.84	60.8
BMP1	4.70	100.5
BMP2	4.04	71.3
BMP3	3.77	70.5
BMP4	3.74	73.7
BMP5	3.35	66.9
BMP6a	4.04	64.4
BMP6b	3.76	64.5
G/GA1.1	4.64	102.8
G/GA1.2	3.39	76.6
G/GA3.1	4.48	101.9
G/GA3.2	3.37	73.6
G/GA2.1	4.47	102.5
G/GA2.2	3.41	72.9
AMA6a	4.41	63.7
AMA6b	4.36	63.7
BMA6a	4.30	63.9
BMA6b	4.48	63.9

5.4.4 Unknown peaks

Figure 5-22 shows an HSQC-spectrum of the wild type where a region with two large unknown peaks (3.77 δ^1H ppm, 58.0 δ^{13}C ppm and 3.53 δ^1H ppm, 51.4 δ^{13}C ppm) is marked. There are also unknown peaks forming a stripe formation at approx. 3.77 δ^1H ppm. A similar pattern of unknown peaks was found in the spectra of ΔL, ΔFG and ΔFGL (appendix F). Figure 5-23 shows an overlay of wild type, ΔF and ΔG that has been zoomed in to the region marked in Figure 5-22. It shows that the two unknown peaks found in wild type (and ΔL, ΔFG and ΔFGL see appendix F) are not found in ΔF and ΔG. ΔF has two peaks that look similar with a different chemical shift (3.83 δ^1H ppm, 58.1 δ^{13}C ppm and 3.63 δ^1H ppm, 51.4 δ^{13}C ppm), and ΔG has only one peak in this region at 3.72 δ^1H ppm and 58.7 δ^{13}C ppm.
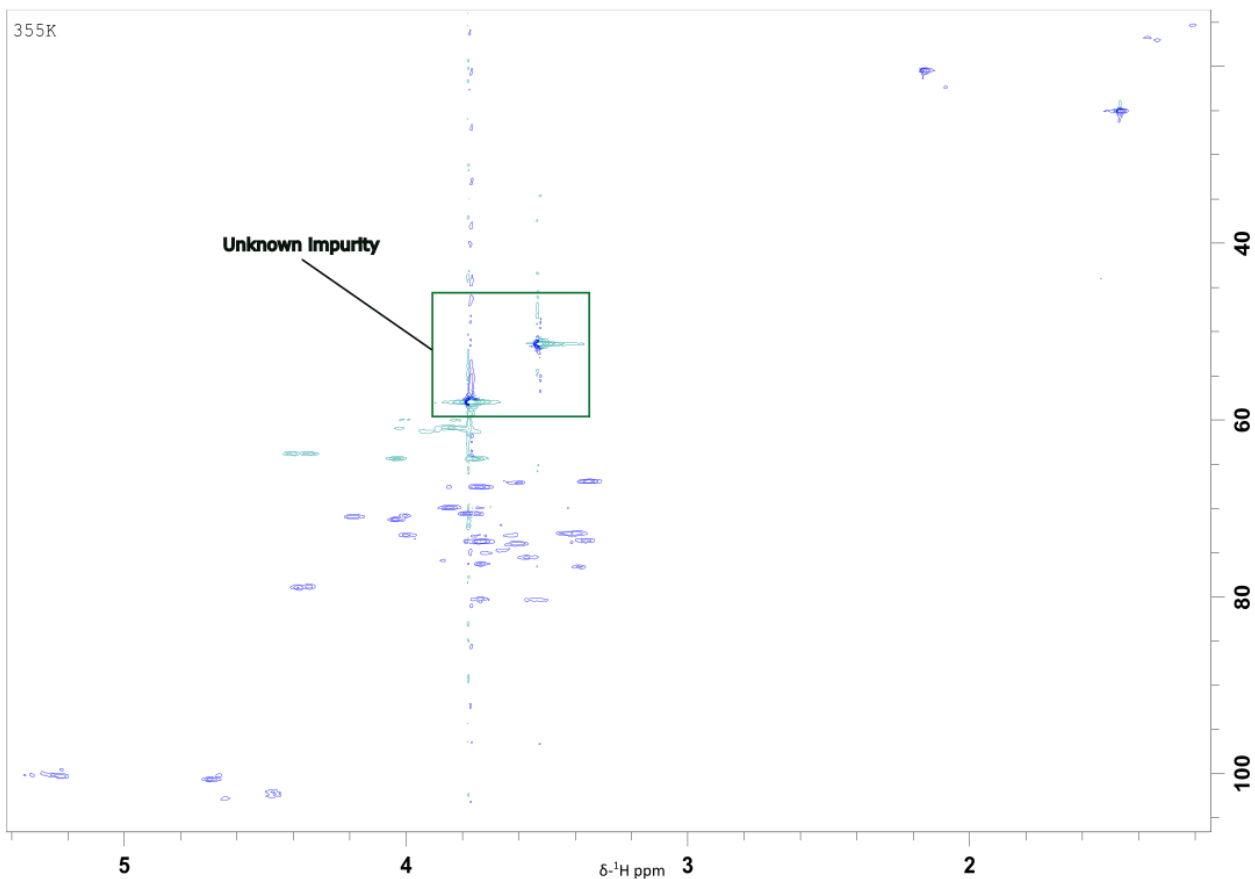
Figure 5-22 HSQC spectrum on the wild type spectra (355 K) in the region 5.41-1.15 δ ^{1}H ppm, 105.9-14.1 δ ^{13}C ppm with a region of impurities marked with a green square. The same impurities were found in ΔL, ΔFG and Δ FGL. The peaks forming a stripe at approx. 3.77 δ ^{1}H ppm were also thought to be a result of impurities.
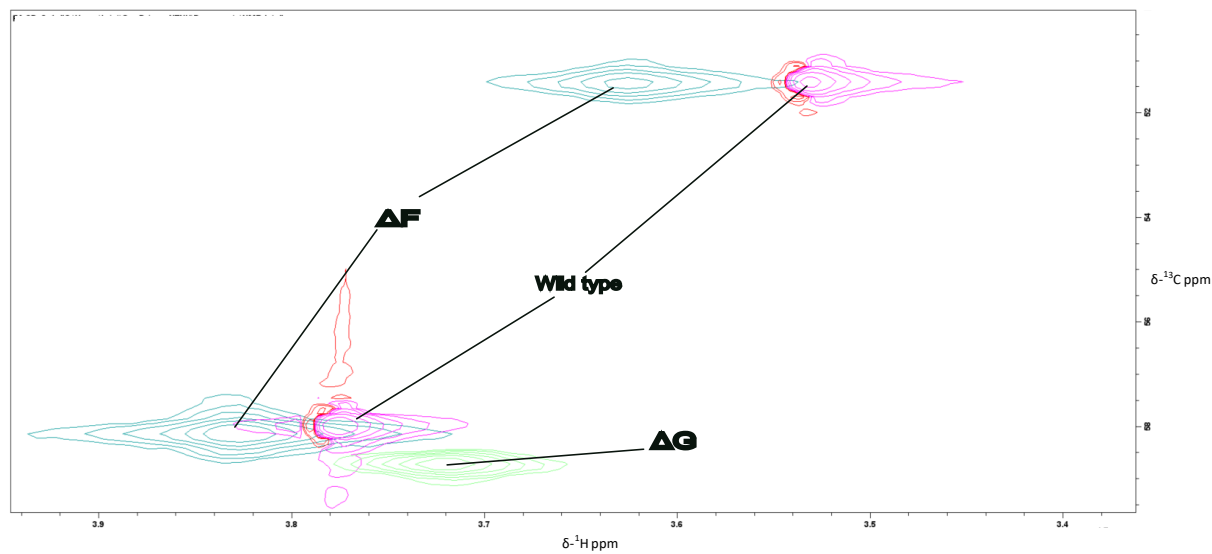
Figure 5-23 Overlay of the HSQC-spectra of wild type (purple/red), Δ-F (dark green) and Δ-G (bright green) in the region 3.94-3.36 δ ^{1}H ppm and 59.6-50.0 δ ^{13}C ppm showing unknown impurities. Peaks similar to the peaks found in the wildtype were also found on ΔL, ΔFG and Δ FGL as seen in appendix F.

6 DISCUSSION

Three different main experimental methods have been used to characterize and compare different mechanically degraded biotechnologically modified xanthan variants: SEC-MALS, ^{1}H-NMR and 2D NMR. This section will be used to discuss the results and evaluate the methods. In addition to this, the results from the fermentation of the wild type, ΔFGL, ΔL and ΔFG, and results from the acetate and pyruvate content of all samples will be discussed.

6.1 Fermentation

The correlation between the fermentation yields of the wild type, ΔFGL, ΔL and ΔFG and the theoretical maximum molecular weight per RU presented in Table 5-2 could explain the differences in the fermentation yields. However, this correlation could not explain the difference in fermentation yield between the samples and the wild type since the measured yield was consistently greater than the expected difference given a theoretical maximum molecular weight per RU of samples. This meant that the differences in fermentation yield had to be a result of either reduced production of xanthan or altered composition of RUs (i.e., having more low M_w RUs).

The results from Table 5-3 were obtained by analyzing a solution of 10 g/L and presented in [mM] (Gansbiller et al., 2019). This means that the results do not reflect the RU compositions or the differences in the average molecular weight of the RUs. These results should therefore not be used to measure the effect of the position of combination of substitutions. However, the total acetate and pyruvate content could be used as a comparative parameter by itself.

The results of the acetate and pyruvate content of the different genetic variants were similar to what was found by Hassler and Doherty (1990) and Gansbiller et al. (2019). The removal for gumL in ΔL and ΔFGL resulted in pyruvate levels close to the detection level of the analysis. The 3-fold increase in acetate in ΔL compared to the wild type can be explained by there not being a competition between pyruvate and acetate at the terminal mannose when both *gum*L and *gum*G are present, like in the wild type.

In ΔG the increased pyruvate levels could be explained by not having a competition at the terminal mannose since the *gum*G is removed.

In ΔF the acetate reduction could be explained by not having the possibility of inner acetylation and only having the possibility of acetylation at terminal mannose where it has competition from the gumL.

The increased levels of pyruvate in ΔF and increased level of acetate in ΔG was unexpected and could not be explained by a different level in competition between the acetyltransferases and the pyruvate ketalases. However, as previously mentioned these results do not reflect the RU compositions or the differences in the average molecular weight of the RUs. This means that the unexpected variations in acetate and pyruvate could be a result of differences in RU compositions.

6.2 Determination of physical properties by SEC-MALS

Previous studies have shown that SEC-MALS on high molecular weight polysaccharides such as xanthan can be used to compare how different processing or molecular modifications affect the physical properties of the polymer. A similar comparison was done in this project, where the final M_w and R_w as well as the M_w and R_w elution profiles of different biotechnologically modified xanthan were determined and compared. Since the results of 25 µl injection were of good quality for all the samples, the results from the 50 µl injection were discarded. This was because the 25 µl injection reflects the properties of the samples in more dilute conditions reducing interactions between the polymers.

Table 5-4 showed the estimated M_w and R_w values after ten cycles of mechanical degradation as described in chapter 4.2.2. These values were close to what has been reported earlier by Osebakken (2019) (230-641 kDa, 38-63 nm) and Holmvik (2018) (546-1414 kDa, R_w not found). The variations between the sample seen in the M_w and R_w (323-620 kDa, 37-46 nm) from Table 5-4 could have been caused by several factors. It is reasonable to assume that the different side chains compositions could have influenced the stability of the samples during the degradation and that this could affect the level of denaturation and formation of aggregates. It could also be explained by differences in M_w and R_w before degradation, although the result from zero cycles were not considered reliable.

In Figure 5-3, the reduction in distribution line widths and linearization of the M_w lines indicated that the material had gotten less disperse, and that the average size got reduced after being mechanically degraded.

Since there was no correlation between the variations in the M_w profiles observed in Figure 5-4 and the linear R_w profiles in Figure 5-5 it became evident that there were differences in R_w:M_w ratios amongst the particles in the samples. This could be explained by the presence of particles that appear to have the same molecular weight but have different hydrodynamic volume in the solutions. This might be a result of aggregates in the samples. Inter-dimeric aggregates formed by renatured strands have a lower radius of gyration due to a more compact formation and a looser conformation between the connected strands leading to lower chain stiffness and R_w. A simple illustration of this principle is given in Figure 6-1 where both the intra- and inter-renaturation reduces the ratio between radius of gyration and molecular weight.
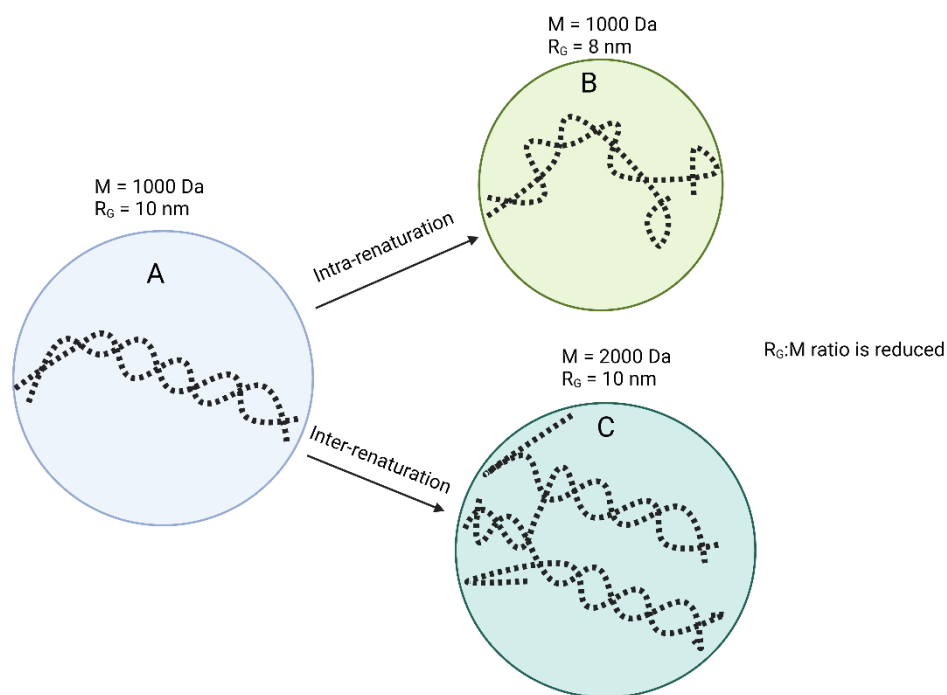
Figure 6-1 Simple illustration of inter- and intra-renaturation of the ordered structure of xanthan induced by either solvent conditions, heat, or mechanical stress. Example A is the native form of xanthan with a radius of gyration to molecular weight (R_G:M) ratio of 0.01. Example B has the same molecular weight but has a reduced radius of gyration due to hair-pin loops formed during renaturation giving it an R_G:M ratio of 0.008. Example C has doubled its molecular weight but has the same radius of gyration due to the formation of a dimer with another double strand giving it an R_G:M ratio of 0.005. Both example B and C have reduced the RG:M ratio after renaturation.

The formation of more compact molecules by intra-renaturation or aggregates by inter-molecular renaturation could have been caused by mechanical degradation as proposed by Lagoueyte and Paquin (1998). This suggests that in general, highly linear elution profiles indicate little or no aggregation, while irregular or non-linear profiles indicate the presence of aggregates.

The study of Lagoueyte & Paquin were performed in low ionic strengths and experiments performed by Osebakken et al. proved that buffering the solution and doing the mechanical degradation in high ionic strength solvents improved the stability and avoided denaturation during mechanical degradation (Osebakken, 2019).

Previous studies have shown that removal of pyruvate substituents or presence of acetate improves the stability of the ordered structure of xanthan while the presence of pyruvate destabilizes the ordered structure of xanthan (Kool et al., 2014, Hassler and Doherty, 1990, Gansbiller et al., 2019). Assuming that denaturation during mechanical degradation is reduced for high stability ordered structures, it is reasonable to expect that xanthan without substituents or with a high acetate content is more stable during mechanical degradation compared to samples with high pyruvate or low acetate content.

This assumption correlates well with the highly linear elution profiles of the ΔL, ΔFGL and ΔG which either lack substituents or are high in acetate (Figure 5-4). It also correlates well with the less linear profiles of WS and ΔFG since they both have high pyruvate and low acetate content (Figure 5-2). The native and renatured strands would likely have different R_w:M_w ratios meaning that molecules of the same M_w could elute at different elution volumes. However, this becomes even more complex when

considering the heterogenous nature of the solutions, where strands with different stability might be simultaneously present in the same solution. This leads to the possibility of having both native and renatured strands in the solution after mechanical degradation.

However, even if the irregularities seen in Figure 5-4 correlate with the explanation above, it is important to stress that it is speculative and that other explanations such as unknown impurities could possibly explain the irregularities. To further test this, the impurity experiment and the stability experiment was done with ΔF and ΔG samples chapter 5.2.3.

Since the less linear M_w elution profiles of ΔFC and ΔGC (Figure 5-6 and Figure 5-7) in the stability experiment could be explained by the formation of aggregates after renaturation, the results correlated with the explanation that the linearity of the M_w elution profiles was related to the stability of the samples. The skewed weight distributions could also be related to the formation of the aggregates (i.e., larger fragments) as fragments of larger hydrodynamic volume elutes earlier in SEC.

Even though the stabilized samples (ΔFB and ΔGB) showed that a buffer with higher ionic strength indicated a reduction in aggregate formation, the results were not considered reliable since the material used for the ΔFB and ΔGB parallels was dialyzed and freeze dried before the SEC-MALS experiments. These processing steps could explain the differences in injected mass (Figure 5-6 and Figure 5-7) and might have affected the results.

The results of the impurity experiment presented in Figure 5-8 showed that treating the wildtype with active carbon removed some of the mass and made less linear M_w elution profiles compared to the standard. This indicated that no impurities causing less linear elution profiles had been removed by the active carbon treatment.

To summarize, SEC-MALS was used to characterize and compare native and different xanthan variants. This was possible due to the partially depolymerization resulting from mechanical degradation. The main insight from SEC-MALS is that mechanical degradation consistently decreased the molecular weight of xanthan from approx. 3500-6700 kDa (at 0 cycles) to approx. 280-610 kDa (after 10 cycles).

The limitations of using SEC-MALS as a characterization tool for mechanically degraded biotechnologically modified xanthan that were elucidated based on the experiments conducted in this project was considered to revolve around the unreliable results from high molecular weight xanthan.

6.3 Order-disorder transition analysis by ^{1}H-NMR

Previous studies have used many analytical methods such as rheometry, light scattering, optical rotation and NMR spectroscopy to investigate the thermally induced order-disorder transition of native xanthan (Bercea and Morariu, 2020, Norton et al., 1984, Morris et al., 1977). Other studies have even investigated the influence of the side chain composition on the order-disorder transition using rheometry (Gansbiller et al., 2019) and optical rotation (Kool et al., 2014). However, no studies of the influence of the side chain compositions of biotechnologically modified xanthan have been done using NMR spectroscopy to our knowledge. In this project, this has been analyzed using mechanically degraded biotechnologically modified xanthan variants.

The expected temperature range for order-disorder transition of xanthan depends on the molecular weight, concentration, pH, ionic strength, and level of aggregation. For chemically degraded xanthan in a dilute solution (1 g/L, 0.04 M NaCl) the transition temperature is found around 65-82 °C in optical rotation experiments depending on the degree of depolymerization and side chain composition (Rinaudo et al., 1983). This means that both the anomeric proton peaks and methyl peaks of the wild type, ΔFG, ΔFGL and Δ F were close to the expected range. The anomeric proton peaks and acetate and pyruvate methyl peaks of ΔG and ΔL were higher than the reference data of Rinaudo et al. (1983).

6.3.1 Choosing the reporter

The anomeric proton of the α-mannose (AM1) was considered the best reporter since it was represented in all the spectra, did not overlap other signals (Figure 5-10), and could produce sigmoidal melting curves (Appendix B). The difference in T_m between the α-mannose H1 and the β-mannose H1 could have been caused by the overlap between β-mannose H1 peak with G/GA1.1 (Figure 5-10).

6.3.2 The effect of acetate and pyruvate content

By comparing the acetate and pyruvate content of each sample with the wild type (Figure 5-2) a correlation between acetate- and pyruvate content and the T_m (Figure 5-11) was found (Figure 5-13).The T_m of the xanthan material seemed to be affected by the presence or absence of pyruvate and acetate groups. The T_m increased when pyruvyl was removed or when no groups were attached, and decreased when acetate was removed. The difference between ΔF and ΔFG suggested that removing both acetates had a greater effect than removing one. This might imply that the presence of acetate groups increases the stability of the ordered structure, while pyruvyl groups reduce it.

The results of Rinaudo et al. (1983) that were obtained using optical rotation experiments reported that the T_m was reduced when acetate was removed, increased when pyruvate was removed and slightly decreased when the both acetate and pyruvate was removed. The results of Gansbiller et al. (2019) obtained from rheometry concluded that the stability decreased when acetate content was reduced, increased when pyruvate content was reduced and increased when both acetate and pyruvate content was reduced. Their findings concerning the acetate and pyruvate free xanthan samples were contradictory. However, this could be explained by the fact that they used different measurement techniques and that the samples were modified differently (i.e., chemical, and biotechnological modification).

In this thesis, the increased T_m of ΔFGL compared to the wildtype (Figure 5-11) and the almost 1:1 ratio of acetate and pyruvate in the wild type (Figure 5-2) indicated that the destabilizing effect of pyruvylation was greater than the stabilizing effect of acetate.

6.3.3 Position of the acetate substitution

Based on the findings of Gansbiller et al. (2019) it was thought that both the position of acetyl and the total content of acetate or pyruvate were two factors that could affect the melting temperature. In this thesis it was concluded that a comparison between ΔG and ΔF would not be well suited to investigate whether an acetyl on the α-mannose or an acetyl on the β-mannose contributes more to the stability of the ordered structure. This was because even though they have same the pattern except for the position of the acetyl, they differ too much in both total acetate and pyruvate content to be reliably compared (Figure 5-2). A better approach would be to compare samples that have similar acetyl and pyruvate contents but different acetyl positions. A potential way of doing this could be to compare xanthan from a mutant without the *gum*F and *gum*L genes (ΔFL) and xanthan from a mutant without the *gum*G and *gum*L genes (ΔGL). These mutants would be able to produce only RU-Cs and -Fs or only RU-Ds and -Fs (Figure 5-1), respectively making it possible to investigate how the position affects stability. However, this has been attempted using rheometry by both Gansbiller et al. (2019) and Hassler and Doherty (1990), and failed since neither achieved ΔGL and ΔFL variants with similar acetyl and pyruvyl content.

6.3.4 Molecular weight

A study by Kitamura et al. investigated whether the transition temperature had any systematic dependence of molecular weight, but their findings did however not support this (Kitamura et al., 1991). This was also investigated for this thesis, and no correlation between M_w or R_w and T_m was found (Figure 5-12).

6.3.5 Degree of substitution

The calculated DS values of acetyl and pyruvyl exceeded the theoretical maximum in all the samples except ΔFGL (Table 5-9). An explanation for this could be line broadening of the anomeric proton caused by the ordered structure and high molecular weight of the material. This incoherence indicates that the integral measured for the anomeric proton (as a reference to estimate the amount of pyruvate and acetate) may have been weaker than expected, thus leading to the overestimation of the DS.

6.3.6 Impurities and aggregates

Indications of impurities in the samples (chapter 5.4.4) and aggregations (chapter 5.2.2) might have affected the melting curves. Future work could attempt to purify the samples even more by doing several rounds of isopropanol precipitation or filtration, or attempt to measure the difference in T_m between native and renatured xanthan. This could reveal if any of these factors have any significant impact on ^{1}H-NMR-estimated T_m values of xanthan.

6.3.7 ^{1}H-NMR tool for characterizing xanthan stability

Even though using ^{1}H-NMR to measure data for melting curves from mechanically degraded biotechnologically modified xanthan variants was successful for the wildtype, ΔFG, ΔFGL and ΔF, it turned out to be challenging for ΔL and the methyl groups of ΔG since they were too stable in temperature range of this experiment (298-363 K). The experiment was however restricted to being below the boiling point of D_2O (374.4 K or 101.4 °C, SIGMA-ALDRICH (2023)). The change of integral as a function of temperature for these xanthan variants did not always produce a sigmoidal trend, leading to incomplete and possibly misleading melting curves. The overestimated DS values (Table 5-9) and difference between the reporters (Table 5-8) indicated that the T_m values did not actually represent the melting temperature of the ordered structure since weak signals of the anomeric protons could

indicate that it had not fully dissociated at 363 K. This means that for these cases using ^{1}H-NMR might not yield accurate measurements. Nevertheless, the technique can still be used to probe the stability of many different variants given that the melting temperature is below the boiling point of D_2O.

6.4 2D-NMR

Previous studies have partially assigned the wild type xanthan spectra (Cheetham and Mashimba, 1992, Rinaudo et al., 1983). Due to the line broadening in high molecular weight native xanthan the partial assignments relied on either partial or fully depolymerization. Some of the easily identifiable peaks such as the anomeric proton of the α-mannose and the methyl groups of the substituents could be assigned on the native xanthan, while further assignments were only possible after partial or full depolymerization (Cheetham and Mashimba, 1992). These assignments are outdated and a partial assignment by 2D-NMR experiments was done to confirm the identity of the atoms used to report melting curve and learn more about the structure of xanthan.

6.4.1   Identifying the anomeric proton peaks of α- and β-mannose

The non-substituted and pyruvylated sugar ring spin systems found by using the 2D-NMR assignment strategy described in appendix D could be used to confirm the position of the anomeric proton of the α- and β-mannose. The α- and β-classifications of the mannose spin systems were deducted from their relative position on the proton spectrum (chapter 5.4). Typically, anomeric protons of α-mannose are found at a higher frequency than anomeric protons of β-mannose (Gerwig, 2021). It is also common for the C6-carbons on an α-ring to be found at a higher frequency on the carbon spectrum than the C6-carbons on a β-ring (Gerwig, 2021). The pyruvylated spin system from Figure 5-14 was connected to the pyruvyl methyl peak through a quaternary carbon peak as predicted by the chemical structure of xanthan which confirmed that it was the pyruvylated β-mannose.

As Cheetham and Mashimba (1992) speculated, the anomeric proton of β-mannose overlapped another anomeric proton as seen in Figure 5-10. They assigned this other anomeric proton as the anomeric proton of glucuronic acid after analysis of depolymerized xanthan.

6.4.2   Further assignment of wild type spectra

It was interesting to see if the 2D-NMR spectra of the biotechnologically modified xanthan variants could be used to improve the existing partial assignments. By overlaying spectra from different variants, it was believed that some peaks could be assigned based on the elimination method. For instance: theoretically, there should be peaks in the Δ-L spectrum belonging to the acetylated mannoses that do not appear in the Δ-FGL-spectrum. This means that by eliminating all the overlapping peaks from two almost identical HSQC-spectra, the remaining HSQC-peaks should represent the spin systems they do not have in common. However, even though the signal of a substance is absent in an NMR spectrum, the substance might still be present in the sample. Low concentration, line broadening or noise might make signals invisible (Torres and Price, 2016).

This approach identified distinct peaks that belonged to the acetylated mannoses (AMA6a/b and BMA6a/b) and glucose residues (Glc6a/b). In Figure 5-20, HSQC-spectra of the wild type, Δ-F and Δ-L was used to identify and assign the H6-C6 peaks of acetylated α-mannoses (AMA6a/b and BMA6a/b), while Figure 5-18 could identify the H6-C6 peaks of glucose on the wild type spectrum.

After assigning the peaks in Figure 5-21, there were still unassigned peaks in all the spectra (appendix F). Most of these unassigned peaks were from unassigned mannose signals or glucose and glucuronic acid residues, but some are speculated to be a result of impurities (Figure 5-23).

Before comparing the partially assigned spectrum of the wild type from this thesis with existing assignments there are two things to point out. Firstly, in the article *"Proton and carbon-13 NMR studies*

on xanthan derivatives" by Cheetham and Mashimba (1992) it is pointed out that there are differences in chemical shifts between the partially depolymerized and the fully depolymerized xanthan samples. Secondly, the existing assignments (Cheetham and Mashimba, 1992, Rinaudo et al., 1983) were made from enzymatically and chemically modified samples, while this thesis used biotechnologically modified samples. This makes it difficult to compare the partial assignment from Table 5-11 with the existing assignments (Cheetham and Mashimba, 1992, Rinaudo et al., 1983). Having this in mind, it is still interesting to use the existing assignments to attempt assigning the remaining anomeric peaks in Figure 5-17. Cheetham and Mashimba (1992) wrote that they believed the anomeric proton of the glucuronic acid residue shifts to a lower frequency upon depolymerization and that it in high molecular weight polymers would have a higher shift than the anomeric protons of the glucose in ^{1}H-NMR. Based on this it would be reasonable to assume that G/GA1.1 in Figure 5-17 is the anomeric proton of the glucuronic acid residue and that the G/GA1.2 consequently would be the H2-C2 of the glucuronic acid residue. This is also somewhat supported by the comparison of the ^{13}C-shifts of the anomeric proton of the glucuronic acid in the partial and fully depolymerized samples from the article "*Proton and carbon-13 NMR studies on xanthan derivatives*" by Cheetham and Mashimba (1992). Doing new experiments with more variants (ΔFL, ΔGL and ΔI) at a lower molecular weight might prove the hypothesis of Cheetham and Mashimba (1992), but will remain a speculation for this thesis.

It was not possible to tell whether the NMR-assignments of biotechnologically modified xanthan yield different chemical shifts than assignments based on chemically or enzymatically modified xanthan using the results from this thesis. However, is it reasonable to assume that biotechnologically modified samples are purer than chemically or enzymatically modified samples that might have residual acetyl or pyruvyl after the chemical or enzymatical treatment. This suggests that if the readability of the spectra is improved by lowering the molecular weight even more than it was done in this project, using biotechnologically modified samples and modern 2D-NMR experiments might yield even better assignments than the existing ones. Another indication of this is that even with depolymerized samples, Cheetham and Mashimba (1992) only generated partially assigned spin systems for the non-acetylated mannoses and the pyruvylated β-mannose, while complete spin systems of the non-acetylated mannoses, the pyruvylated β-mannose and some partially assigned spin systems was assigned in this thesis (Table 5-11). Based on this it is reasonable to state that the strategy used in this thesis already has improved, and has an even greater potential to further improve, the existing assignments of wild type xanthan spectra.

7 FUTURE WORK

Future research with the objective of analyzing the order-disorder transition of native xanthan (i.e., not renatured) could attempt to improve the protocol by either doing the mechanical degradation at higher ionic strength or using gentler method of depolymerization. The data from the native xanthan could then be compared with T_m values of reheated samples (i.e., renatured). In addition to this, future work could attempt to purify the extracted material even more before homogenizing by doing several rounds of isopropanol precipitation or filtration. This could reveal if these factors had any significant impact on the ^{1}H-NMR-estimated T_m values of xanthan obtained in this project.

To further improve the NMR assignment of wild type xanthan, two strategies are proposed based on the findings in this thesis. Firstly, it could be possible to improve the readability of the NMR spectra by lowering the molecular weight even more by for instance using ultrasonication, or chemical or enzymatical degradation. Secondly, optimizing the strategy by using more variants such as Δ*gum*FL, Δ*gum*GL or even truncated variants with or without acetyl (Δ*gum*IF or Δ*gum*I) might make it easier to assign the glucuronic acid residues. This is because the truncated variants could make it easier to exclude the signals of the glucuronic acid residues since the signal from the outer mannose residues would not be present in the spectra of the truncated variants.

Having an improved NMR assignment of wild type xanthan might enable potential new methods of xanthan characterization. It could be speculated that the RU composition of the different variants could be estimated using NMR by depolymerizing the xanthan material completely down to the separate pentameric RUs and then using the improved assignment of the wild type xanthan spectrum to estimate the composition of RUs in the sample. It could also be interesting to investigate whether an improved NMR assignment of the wild type xanthan could be used to identify and confirm structural modifications of xanthan and to elucidate the positions of said modifications.

8 CONCLUSION

The results from the fermentation showed that there were variations in yield and acetate- and pyruvate content compared to the wild type. The variations in yield indicated either reduced xanthan production or a low M_w RU composition in the mutant strains compared to the wild type. The variations in acetate- and pyruvate content were explained by either increased or reduced competition on the β-mannose or variations in RU composition.

SEC-MALS was used to characterize and compare native and different xanthan variants. This was possible due to the partially depolymerization resulting from mechanical degradation using a Wet Mill Jet Star Burst Mini homogenizer. The main insight from SEC-MALS was that mechanical degradation consistently decreased the molecular weight of xanthan from approx. 3500-6700 kDa (at 0 cycles) to approx. 280-610 kDa (after 10 cycles). Based on the SEC-MALS experiments, the mechanical degradation seemed to have reduced the R_w:M_w ratio in the less stable variants more than the more stable variants. This suggested that the less stable material underwent order-disorder transitions forming aggregates during the mechanical degradation.

^{1}H-NMR was used to estimate the T_m of mechanically degraded native and biotechnologically modified xanthan variants. The anomeric proton of the α-mannose was found to be the best reporter for T_m. The T_m values for the wildtype, ΔFG, ΔFGL and ΔF was successfully estimated using the chosen melting curve model. However, the estimation of the change of integral as a function of temperature failed for all the reporters of ΔL and the methyl groups of acetate and pyruvate in ΔG because they were too stable in the chosen temperature region and did not produce a sigmoidal trend. This means that the experiment showed that the model was successful for samples with a melting temperature below 90 °C. Comparing the acetate- and pyruvate contents with the estimated T_m values showed that increased acetate content increased the T_m, while increased pyruvate content decreased the T_m. The removal of acetate and pyruvate also showed increased T_m. Overestimated DS values and a T_m difference between reporters indicated that the T_m values of the ^{1}H-NMR experiment did not actually represent the melting temperature of the ordered structure since weak signals of the anomeric protons could indicate that it had not fully dissociated at 363 K. This means that using ^{1}H-NMR might not yield accurate measurements. Nevertheless, it was concluded that ^{1}H-NMR could still be used to probe the stability of many different variants given that the melting temperature is below the boiling point of D_2O.

2D-NMR was used to assign the T_m reporters, and to partially assign the rest of the xanthan spectrum of the wild type. Three complete monosaccharide residues were assigned: the non-substituted α- and β-mannose and the pyruvylated β-mannose. The H6-C6 peaks of the acetylated α- and β-mannose and glucose residue were also identified and assigned. In addition to this, six peaks were identified as either glucose or glucuronic acid residues. Based on the results it was suggested that using modern NMR spectroscopy and biotechnologically modified variants was a potential strategy of improving the existing NMR assignments of wild type xanthan.

9 REFERENCES

BECKER, A. 2015. Challenges and perspectives in combinatorial assembly of novel exopolysaccharide biosynthesis pathways. *Frontiers in Microbiology,* 6.

BECKER, A., KATZEN, F., PÜHLER, A. & IELPI, L. 1998. Xanthan gum biosynthesis and application: a biochemical/genetic perspective. *Applied Microbiology and Biotechnology,* 50**,** 145-152.

BERCEA, M. & MORARIU, S. 2020. Real-time monitoring the order-disorder conformational transition of xanthan gum. *Journal of Molecular Liquids,* 309**,** 113168.

CHATURVEDI, S., KULSHRESTHA, S., BHARDWAJ, K. & JANGIR, R. 2021. A Review on Properties and Applications of Xanthan Gum. *In:* VAISHNAV, A. & CHOUDHARY, D. K. (eds.) *Microbial Polymers: Applications and Ecological Perspectives.* Singapore: Springer Singapore.

CHEETHAM, N. W. H. & MASHIMBA, E. N. M. 1992. Proton and carbon-13 NMR studies on xanthan derivatives. *Carbohydrate Polymers,* 17**,** 127-136.

CHRISTENSEN, B. E. 2021. *Compendium TBT4135 Biopolymers,* NTNU, NOBIPOL Department of Biotechnology,.

FLORES CANDIA, J. L. & DECKWER, W. D. 1999. Effect of the nitrogen source on pyruvate content and rheological properties of xanthan. *Biotechnology Progress,* 15**,** 446-452.

FU, X., QIN, F., LIU, T. & ZHANG, X. 2022. Enhanced Oil Recovery Performance and Solution Properties of Hydrophobic Associative Xanthan Gum. *Energy & Fuels,* 36**,** 181-194.

GANSBILLER, M., SCHMID, J. & SIEBER, V. 2019. In-depth rheological characterization of genetically modified xanthan-variants. *Carbohydrate Polymers,* 213**,** 236-246.

GAREGG, P. J., JANSSON, P.-E., LINDBERG, B., LINDH, F., LÖNNGREN, J., KVARNSTRÖM, I. & NIMMICH, W. 1980. Configuration of the acetal carbon atom of pyruvic acid acetals in some bacterial polysaccharides. *Carbohydrate Research,* 78**,** 127-132.

GERWIG, G. J. 2021. Analysis of Carbohydrates by Nuclear Magnetic Resonance SpectroscopyNuclear magnetic resonance spectroscopy (NMR). *In:* GERWIG, G. J. (ed.) *The Art of Carbohydrate Analysis.* Cham: Springer International Publishing.

GUERRA, M. L., MALAFAIA, C. B., MACEDO, A. J., SILVA, M. V., MARIANO, R. L. R. & SOUZA, E. B. 2018. Biofilm formation by Xanthomonas campestris pv. viticola affected by abiotic surfaces and culture media. *Tropical Plant Pathology,* 43**,** 146-151.

GÜNTHER, H. 2013. *NMR spectroscopy : basic principles, concepts, and applications in chemistry,* Weinheim, Wiley-VCH.

HAHN, E. L. & MAXWELL, D. E. 1952. Spin Echo Measurements of Nuclear Spin Coupling in Molecules. *Physical Review,* 88**,** 1070-1084.

HASSLER, R. A. & DOHERTY, D. H. 1990. Genetic Engineering of Polysaccharide Structure: Production of Variants of Xanthan Gum in Xanthomonas campestris. *Biotechnology Progress,* 6**,** 182-187.

HOLMVIK, C., B.E. CHRISTENSEN, AND M.Ø. DALHEIM 2018. Depolymerisation and Characterisation of Xanthans - A study of rheological and structural properties for Enhanced Oil Recovery. *NTNU*.

KITAMURA, S., TAKEO, K., KUGE, T. & STOKKE, B. T. 1991. Thermally induced conformational transition of double-stranded xanthan in aqueous salt solutions. *Biopolymers,* 31**,** 1243-1255.

KOOL, M. M., GRUPPEN, H., SWORN, G. & SCHOLS, H. A. 2013. Comparison of xanthans by the relative abundance of its six constituent repeating units. *Carbohydrate Polymers,* 98**,** 914-921.

KOOL, M. M., GRUPPEN, H., SWORN, G. & SCHOLS, H. A. 2014. The influence of the six constituent xanthan repeating units on the order–disorder transition of xanthan. *Carbohydrate Polymers,* 104**,** 94-100.

LAGOUEYTE, N. & PAQUIN, P. 1998. Effects of microfluidization on the functional properties of xanthan gum. *Food Hydrocolloids,* 12**,** 365-371.

LEE, B.-M., PARK, Y.-J., PARK, D.-S., KANG, H.-W., KIM, J.-G., SONG, E.-S., PARK, I.-C., YOON, U.-H., HAHN, J.-H., KOO, B.-S., LEE, G.-B., KIM, H., PARK, H.-S., YOON, K.-O., KIM, J.-H., JUNG, C.-H., KOH, N.-H., SEO, J.-S. & GO, S.-J. 2005. The genome sequence of Xanthomonas oryzae pathovar oryzae KACC10331, the bacterial blight pathogen of rice. *Nucleic Acids Research,* 33**,** 577-586.

LEE, H.-C. & BRANT, D. A. 2002. Rheology of Concentrated Isotropic and Anisotropic Xanthan Solutions: 3. Temperature Dependence. *Biomacromolecules,* 3**,** 742-753.

MCINTYRE, D. D., CERI, H. & VOGEL, H. J. 1996. Nuclear Magnetic Resonance Studies of the Heteropolysaccharides Alginate, Gum arabic and Gum Xanthan. *Starch - Stärke,* 48**,** 285-291.

MOFFAT, J., MORRIS, V. J., AL-ASSAF, S. & GUNNING, A. P. 2016. Visualisation of xanthan conformation by atomic force microscopy. *Carbohydrate Polymers,* 148**,** 380-389.

MORRIS, E. R. 2019. Ordered conformation of xanthan in solutions and "weak gels": Single helix, double helix – or both? *Food Hydrocolloids,* 86**,** 18-25.

MORRIS, E. R., REES, D. A., YOUNG, G., WALKINSHAW, M. D. & DARKE, A. 1977. Order-disorder transition for a bacterial polysaccharide in solution. A role for polysaccharide conformation in recognition between Xanthomonas pathogen and its plant host. *Journal of Molecular Biology,* 110**,** 1-16.

NATIONAL CENTER FOR BIOTECHNOLOGY INFORMATION. 2023a. *Pubchem Compound Summary for CID 175, Acetate.* [Online]. https://pubchem.ncbi.nlm.nih.gov/compound/Acetate. Available: https://pubchem.ncbi.nlm.nih.gov/compound/Acetate [Accessed 13/05 2023].

NATIONAL CENTER FOR BIOTECHNOLOGY INFORMATION. 2023b. *Pubchem Compound Summary for CID 107735, Pyruvate.* [Online]. https://pubchem.ncbi.nlm.nih.gov/compound/Pyruvate. Available: https://pubchem.ncbi.nlm.nih.gov/compound/Pyruvate [Accessed 13/05 2023].

NORTON, I. T., GOODALL, D. M., FRANGOU, S. A., MORRIS, E. R. & REES, D. A. 1984. Mechanism and dynamics of conformational ordering in xanthan polysaccharide. *Journal of Molecular Biology,* 175**,** 371-394.

OSEBAKKEN, K. G., CHRISTENSEN, BJØRN E. 2019. Conformation of the acid form of xanthan and DMSO. *NTNU*.

PETERS, H. U., SUH, I. S., SCHUMPE, A. & DECKWER, W. D. 1993. The pyruvate content of xanthan polysaccharide produced under oxygen limitation. *Biotechnology Letters,* 15**,** 565-566.

PETRI, D. F. S. 2015. Xanthan gum: A versatile biopolymer for biomedical and technological applications. *Journal of Applied Polymer Science,* 132.

PODZIMEK, S. 2011a. Combination of SEC and Light Scattering. *Light Scattering, Size Exclusion Chromatography and Asymmetric Flow Field Flow Fractionation.*

PODZIMEK, S. 2011b. Light Scattering. *Light Scattering, Size Exclusion Chromatography and Asymmetric Flow Field Flow Fractionation.*

PODZIMEK, S. 2011c. Size Exclusion Chromatography. *Light Scattering, Size Exclusion Chromatography and Asymmetric Flow Field Flow Fractionation.*

RASHIDI, A. R., AZELEE, N. I. W., ZAIDEL, D. N. A., CHUAH, L. F., BOKHARI, A., EL ENSHASY, H. A. & DAILIN, D. J. 2023. Unleashing the potential of xanthan: a comprehensive exploration of biosynthesis, production, and diverse applications. *Bioprocess and Biosystems Engineering*.

RINAUDO, M., MILAS, M., LAMBERT, F. & VINCENDON, M. 1983. Proton and carbon-13 NMR investigation of xanthan gum. *Macromolecules,* 16**,** 816-819.

SCHILLING, C., BADRI, A., SIEBER, V., KOFFAS, M. & SCHMID, J. 2020. Metabolic engineering for production of functional polysaccharides. *Current Opinion in Biotechnology,* 66**,** 44-51.

SENA-VÉLEZ, M., REDONDO, C., GELL, I., FERRAGUD, E., JOHNSON, E., GRAHAM, J. H. & CUBERO, J. 2015. Biofilm formation and motility of Xanthomonas strains with different citrus host range. *Plant Pathology,* 64**,** 767-775.

SIGMA-ALDRICH. 2023. *NMR Deuterated Solvent Properties Reference Chart* [Online]. Available: https://www.sigmaaldrich.com/NO/en/technical-documents/technical-article/analytical-chemistry/nuclear-magnetic-resonance/nmr-deuterated-solvent-properties-reference [Accessed 08/05/2023].

SUGINO MACHINE LIMITED. *Various types of chambers for "Star Burst"* [Online]. Available: https://www.sugino.com/site/qa-e/sbs-techinical-chamber-e.html#ball [Accessed 11.04 2023].

SUTHERLAND, I. W. 1981. Xanthomonas polysaccharides - Improved methods for their comparison. *Carbohydrate Polymers,* 1**,** 107-115.

TAKEMASA KOJIMA, K. T., TOSHIO YANAKI, MITSUAKI MITANI. 1983. *Method for a specific depolymerization of a polysaccharide having a rod-like helical conformation*. USA patent application US06.

TAMPIERI, A., SZABÓ, M., MEDINA, F. & GULYÁS, H. 2021. A brief introduction to the basics of NMR spectroscopy and selected examples of its applications to materials characterization. *Physical Sciences Reviews,* 6.

TORRES, A. M. & PRICE, W. S. 2016. Common problems and artifacts encountered in solution-state NMR experiments. *Concepts in Magnetic Resonance Part A,* 45A**,** e21387.

VORHÖLTER, F.-J., SCHNEIKER, S., GOESMANN, A., KRAUSE, L., BEKEL, T., KAISER, O., LINKE, B., PATSCHKOWSKI, T., RÜCKERT, C., SCHMID, J., SIDHU, V. K., SIEBER, V., TAUCH, A., WATT, S. A., WEISSHAAR, B., BECKER, A., NIEHAUS, K. & PÜHLER, A. 2008. The genome of Xanthomonas campestris pv. campestris B100 and its use for the reconstruction of metabolic pathways involved in xanthan biosynthesis. *Journal of Biotechnology,* 134**,** 33-45.

WASHINGTON, G. E. & BRANT, D. A. 2021. Model for the Temperature-Induced Conformational Change in Xanthan Polysaccharide. *Biomacromolecules,* 22**,** 4691-4700.

WYATT TECHNOLOGY CORPORATION 2019. ASTRA 7.3 User's guide M1006 Rev. I. *In:* CORPORATION, W. T. (ed.).

YAO, H.-Y.-Y., WANG, J.-Q., YIN, J.-Y., NIE, S.-P. & XIE, M.-Y. 2021. A review of NMR analysis in polysaccharide structure and conformation: Progress, challenge and perspective. *Food Research International,* 143**,** 110290.

Appendices

A. Mechanical degradation resiliency experiment

Non-linear molecular weight elution profiles for the wild type and ΔFG compared to highly linear elution profiles in ΔL and ΔFGL led to the conclusion that some aggregation had formed during the mechanical degradation for the less stable variants. It was decided to test this hypothesis when new material of the ΔF and ΔG was obtained. A stability experiment was done to find out if this hypothesis could predict the results of the new material. After receiving more material from Dr Schmidt's lab, the ΔG and ΔF was tested and produced the following results:

Table A 1 Three parallels of both ΔG and ΔF with different protocols. One reference protocol, one stabilizing and one destabilizing protocol

	Standard	Stabilized	Destabilized
ΔG	GA	GB	GC
ΔF	FA	FB	FC

The M_w ranged from 323.7 to 567.8 kDa and the R_w ranged from 34.5 to 48.7 nm Table A 2.

Table A 2 SEC-MALS results from three parallels of both ΔF and ΔG with different mechanical degradation protocols.

	Mn (kDa)	±	M_w (kDa)	±	Polydispersity	R_w (nm)	Calculated mass (µg)
Δ FA	283.8	0.3%	323.7	0.2%	1.14	37.5	6.0
Δ FB	428.0	0.4%	567.8	0.2%	1.33	34.5	9.5
Δ FC	294.2	0.5%	359.0	0.3%	1.22	41.1	7.0
Δ GA	279.1	0.4%	326.5	0.3%	1.17	40.8	7.3
Δ GB	339.5	0.3%	415.2	0.2%	1.22	37.0	13.0
Δ GC	276.5	0.9%	332.6	0.4%	1.20	48.7	8.3

B. Plotted melting curves

Plots of integration values (*I*) from the selected reporter peaks of wild type (WS), ΔFGL, ΔFG, ΔF and ΔG ¹H-NMR spectra over temperature (°C). Plots of ΔL are not included because they could be fitted as explained in chapter 5.3.
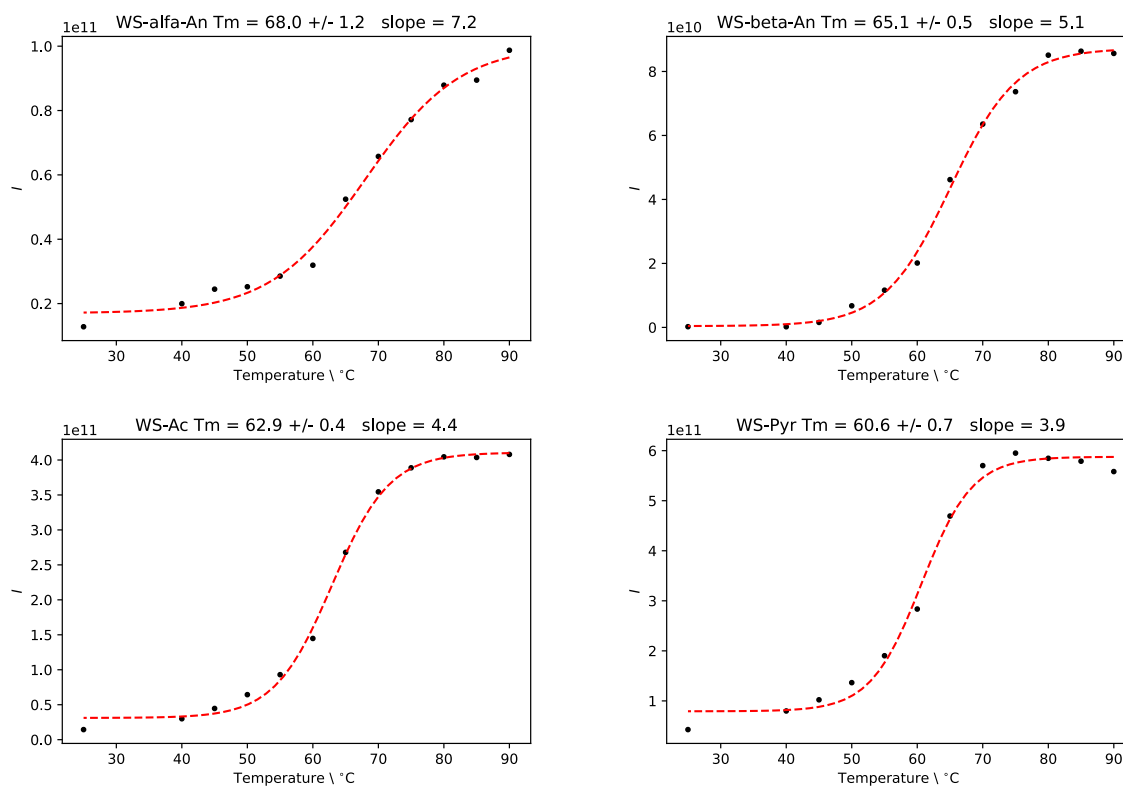
Figure B 1 Plots of integration values (I) from wild type (WS) ¹H-NMR spectra over temperature (°C). WS-α-An: Wild type α-mannose anomeric proton, WS-β-An: wild type β-mannose anomeric proton, WS-ac: wild type acetate and WS-Pyr: wild type pyruvate. T_m was calculated from the midpoint of the temperature induced transition and ranged between 68.0 ± 1.2 and 60.6 ± 0.7. The slope ranged between 3.9 and 7.2.
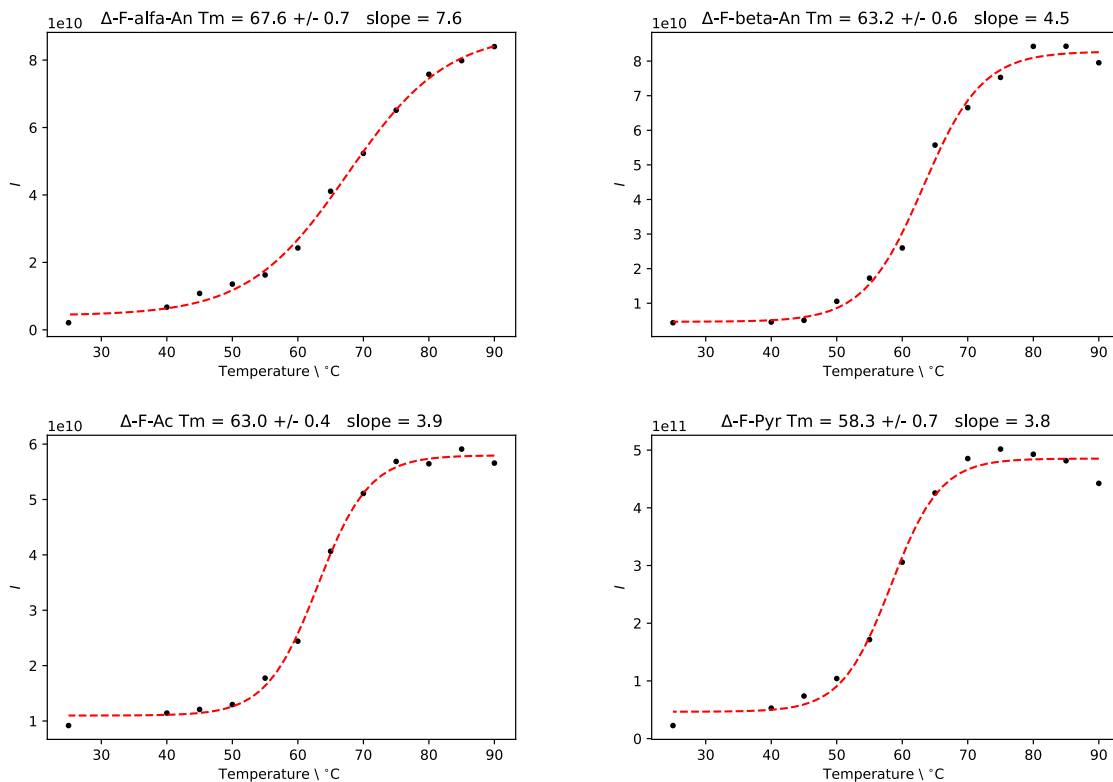
Figure B 2 Plots of integration values (I) from ΔF (Δ-F) ¹H-NMR spectra over temperature (°C). Δ-F-α-An: ΔF α-mannose anomeric proton, Δ-F-β-An: ΔF β-mannose anomeric proton, Δ-F-ac: ΔF acetate and ΔF -Pyr: ΔF pyruvate. Tₘ was calculated from the midpoint of the temperature induced transition and ranged between 67.6 ± 0.7 and 58.3 ± 0.7. The slope ranged between 3.8 and 7.6.
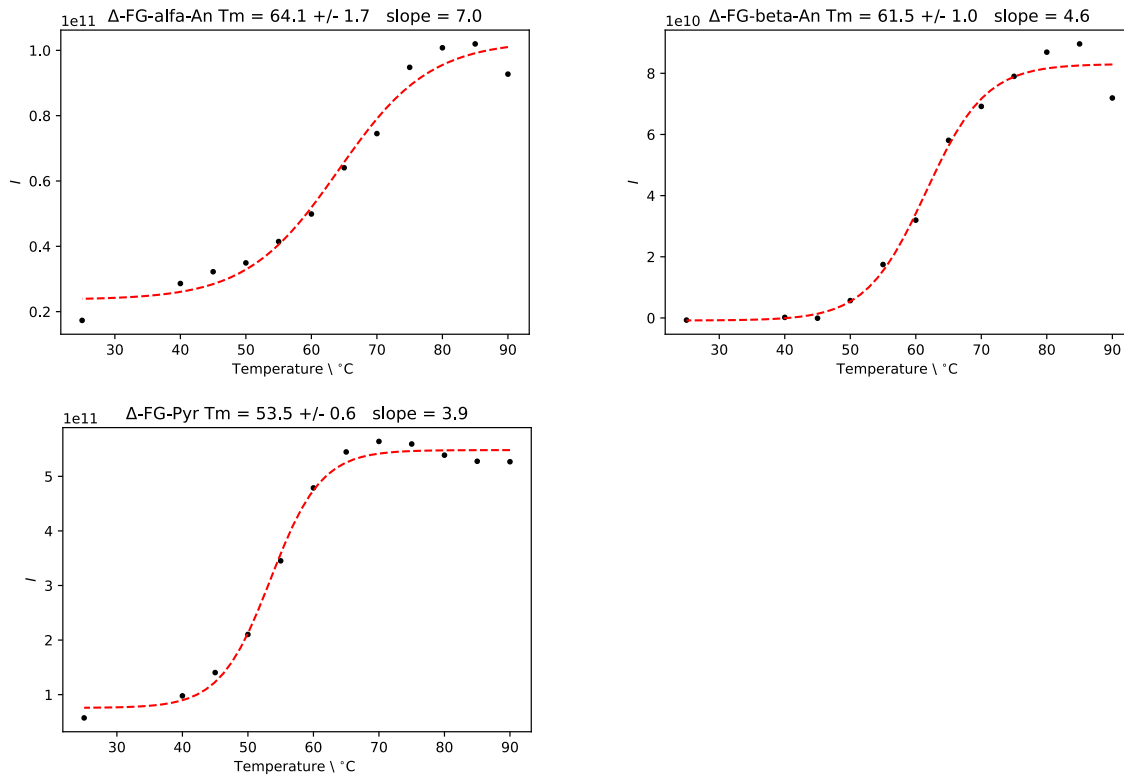
Figure B 3 Plots of integration values (I) from ΔFG (Δ-FG) ¹H-NMR spectra over temperature (°C). Δ-FG-α-An: ΔFG α-mannose anomeric proton, Δ-FG-β-An: ΔFG β-mannose anomeric proton and Δ-FG-Pyr: ΔFG pyruvate. T_m was calculated from the midpoint of the temperature induced transition and ranged between 64.1 ± 1.7 and 53.5 ± 0.6. The slope ranged between 3.9 and 7.0.
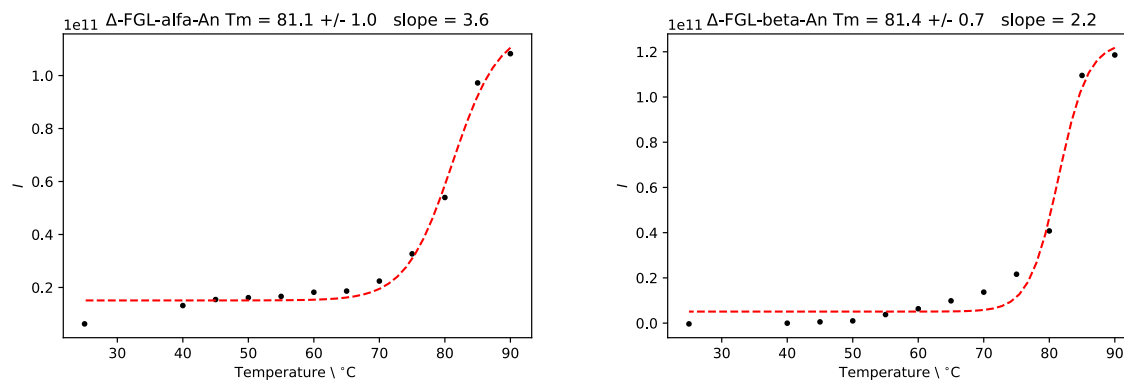
Figure B 4 Plots of integration values (I) from ΔFGL (Δ-FGL) ¹H-NMR spectra over temperature (°C). Δ-FGL-α-An: ΔFGL α-mannose anomeric proton and Δ-FGL-β-An: ΔFGL β-mannose anomeric proton. T_m was calculated from the midpoint of the temperature induced transition and ranged between 81.1 ± 1.0 and 81.4 ± 0.7. The slope ranged between 2.2 and 3.6.
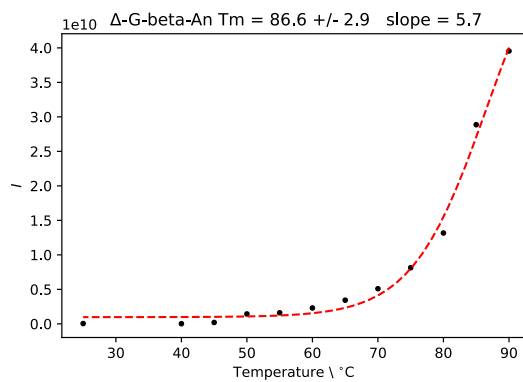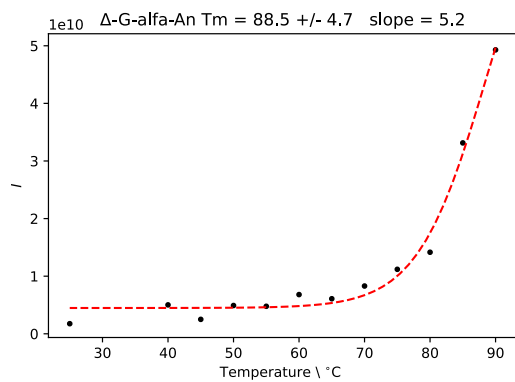
Figure B 5 Plots of integration values (I) from ΔG (Δ-G) ^{1}H-NMR spectra over temperature (°C). Δ-G-α-An: ΔG α-mannose anomeric proton and Δ-G-β-An: ΔG β-mannose anomeric proton. T$_m$ was calculated from the midpoint of the temperature induced transition and ranged between 88.5 ± 4.7 and 86.6 ± 2.9. The slope ranged between 5.2 and 5.7.

C. First derivatives

For all the reporter peaks of the ΔL and the methyl peaks of ΔG, plots of the n-th discrete difference along the y-axis (i.e., integral) were made. The largest values of this plot represented the point with the largest increase, meaning that the midpoint of a potential sigmoidal shape would at least be at said point.
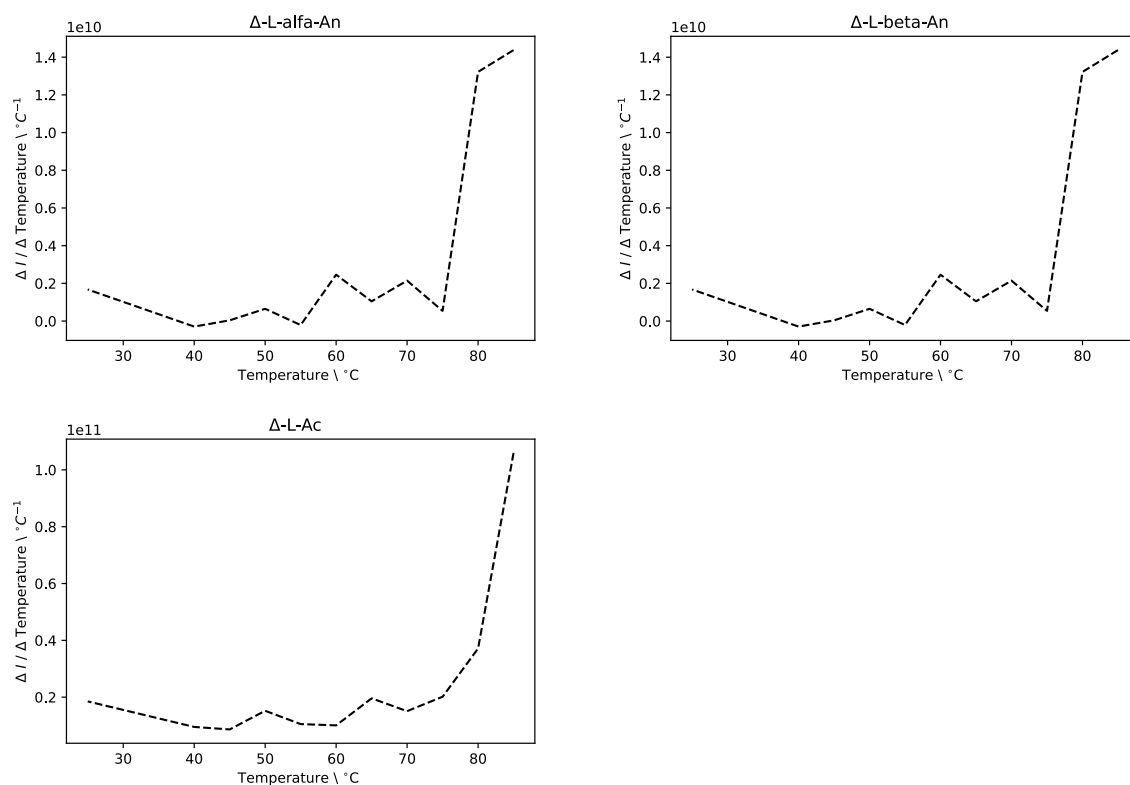
Figure C 1 A reversed plot of the n-th discrete difference (was actually negative but has been reversed from better visualization) of the plotted integral values (I) from ΔL (Δ-L) ^{1}H-NMR spectra over temperature (°C) along the y-axis. Δ-L-α-An: ΔL α-mannose anomeric proton, Δ-L-β-An: ΔL β-mannose anomeric proton and Δ-L-Ac: ΔL acetate. The largest increase on the plot was at 85 °C, meaning that the T_m was at least 85 °C.
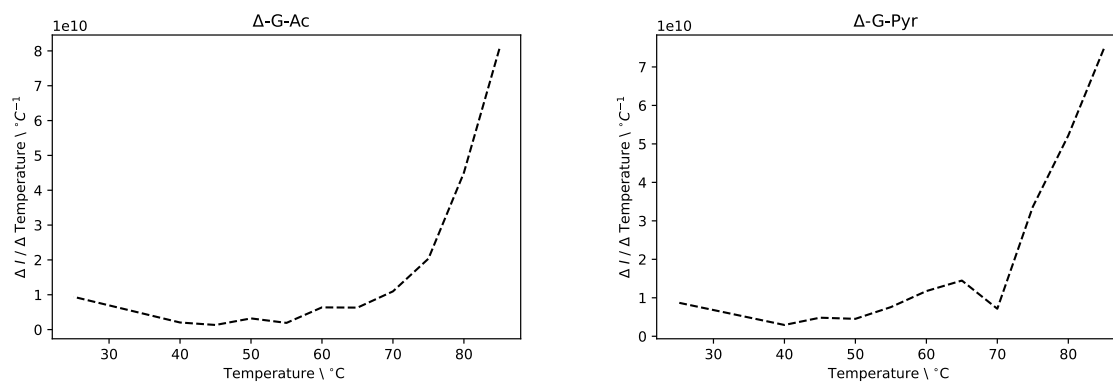
Figure C 2 A reversed plot of the n-th discrete difference (was actually negative but has been reversed from better visualization) of the plotted integral values (I) from ΔL (Δ-L) ^{1}H-NMR spectra over temperature (°C) along the y-axis. Δ-G-Ac: ΔG acetate and Δ-G-Pyr: ΔG pyruvate. The largest increase on the plot was at 85 °C, meaning that the T_m was at least 85 °C.

D. 2D assignment strategy

¹H-¹³C assignment (HSQC, HMBC and H2BC)

The following assignment strategy or similar strategies was performed on all the 2D-NMR spectra that were obtained. The figures are screenshots from Topspin and were not fully processed in Inkscape. The x-axis is δ-¹H ppm and the y-axis δ-¹³C ppm for all figures in this chapter. The figures and text refer to proton-carbon peaks in a simplified manner, where H6-C6 is shortened to just H6. Another simplification in this section is that correlations are shown through lines that are drawn onto the spectra, while chemical shifts (ppm) are not described.

To find the first spin system of the WS-material, the HSQC-pyruvate peak (i.e., methyl group of the pyruvate) was selected as a starting point. This was because the HSQC-pyruvate peak was expected to have two HMBC-correlations and one H2BC-correlation to its neighbouring carbons. In Figure D 1, the molecular structure of the β-Mannose is presented where the two- and three bond correlations are coloured with respectively red and blue.
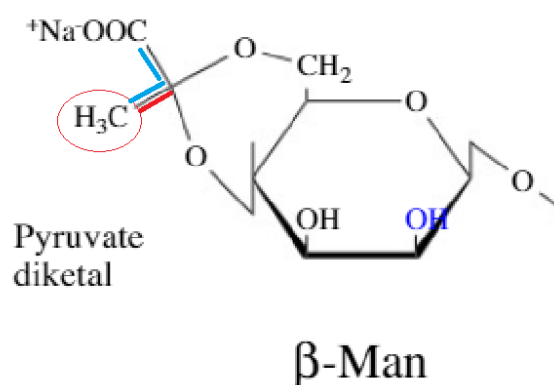
Figure D 1 The structure of the β-mannose with the predicted two and three bond correlations marked in respectively red and blue. Retrieved from (Christensen, 2021) and annotated in MS paint.

The predicted correlations did show up in the 2D-NMR spectrum of WS at high temperature (355 K) as shown in Figure D 2. The carbon correlation at the highest frequency at 176 ppm was assumed to be a carboxyl group due to its high frequency. Therefore, it was assumed that the remaining peak at around 102 ppm was due to a two-bond correlation with the pyruvyl group, called the quaternary carbon. However, this was not found on the H2BC-spectrum.
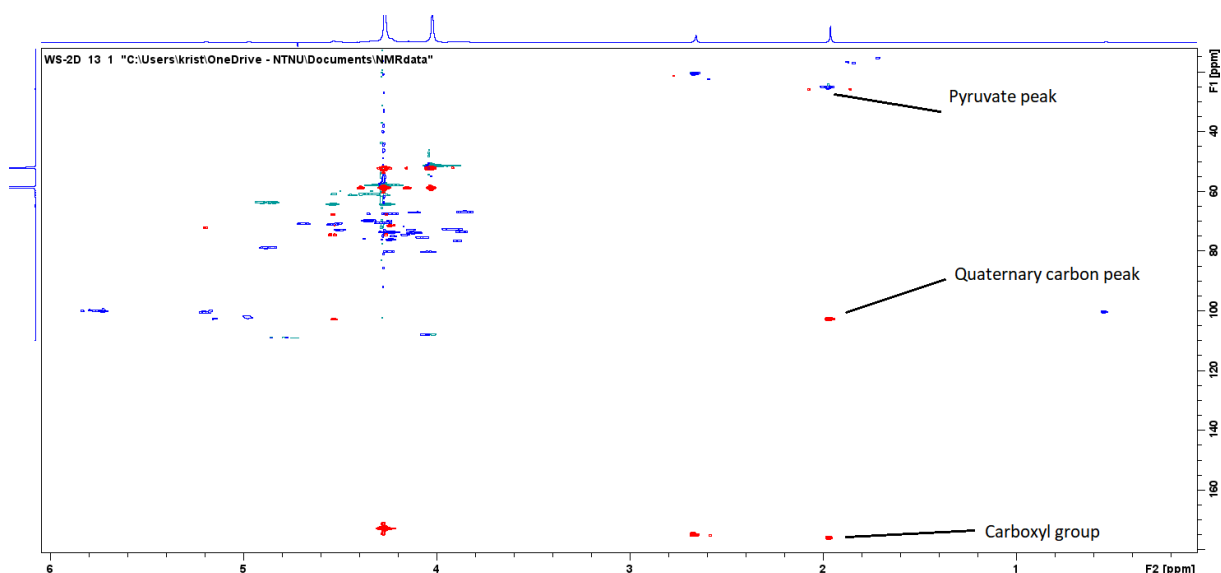
Figure D 2 A two-layered 2D spectrum of HSQC and HMBC readings of WS at high temperature (355 K). Blue = HSQC CH/CH3 peaks, green = HSQC CH2 peaks and red = HMBC peaks.

The quaternary carbon peak was expected to have a correlation with both the β-mannose H6 and β-mannose H4, and because the β-mannose H6 position is a CH2, it should turn up as green on this spectrum due to its negative phasing. This was found in Figure D 3. After finding the β-mannose H6, an attempt was made to assign the rest of the spin system using the strategy explained below.
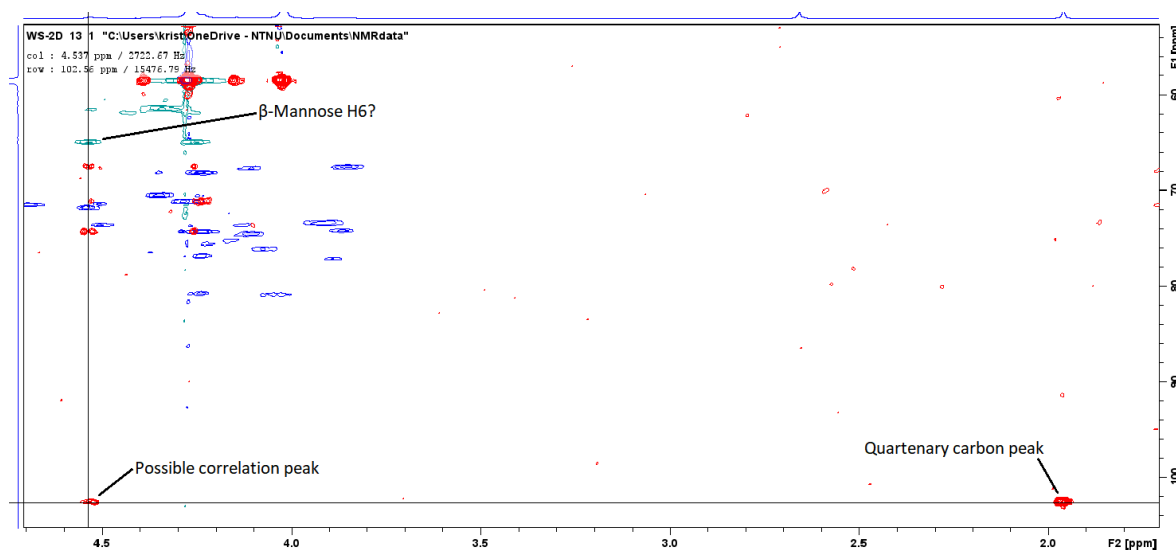
Figure D 3 HSQC + HMBC of WS where the assumed quaternary carbon correlation peak is correlated to a CH2 HSQC peak assumed to be a β-mannose H6 peak. Blue = HSQC CH/CH3 peaks, green = HSQC CH2 peaks and red = HMBC peaks.

The β-mannose H6 signal in Figure D 4 seemed to be split into two peaks, having the same carbon shift. This is common for CH2-peaks because it can behave diastereotopically. Both split signals seem to correlate to the same HSQC-peak through two HMBC peak at the same carbon shift. This peak could be either β-mannose H5 or β-mannose H4 since the HMBC spectrum does not distinguish between two- or three bond correlations.

75
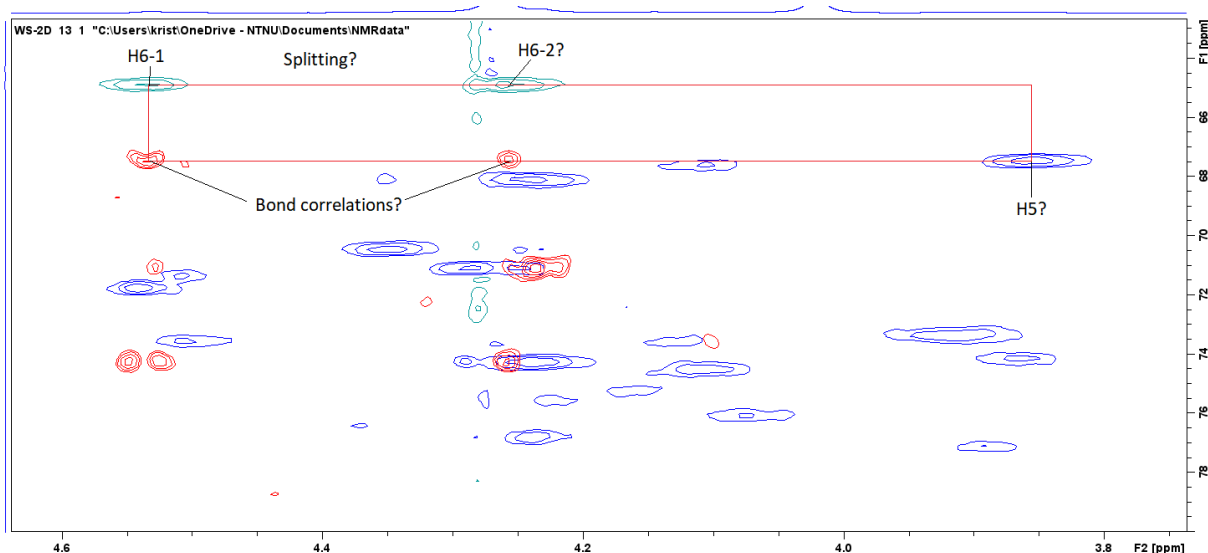
Figure D 4 HSQC + HMBC of WS where the assumed β-mannose H6 from Figure D 3 is correlated to an assumed β-mannose H5 or β-mannose H4 peak through a multiple bond correlation. The assumed β-mannose H6 seemed to be a split peak because another CH2 peak at the same carbon chemical shift had a multiple bond correlation to the same assumed β-mannose H5 or β-mannose H4 peak. Blue = HSQC CH/CH3 peaks, green = HSQC CH2 peaks and red = HMBC peaks.

A new HMBC-correlation was found in Figure D 5 between the β-mannose H6-peaks and a new unidentified peak. This did not contribute to identifying what peaks belong to which position, so further investigation was needed.
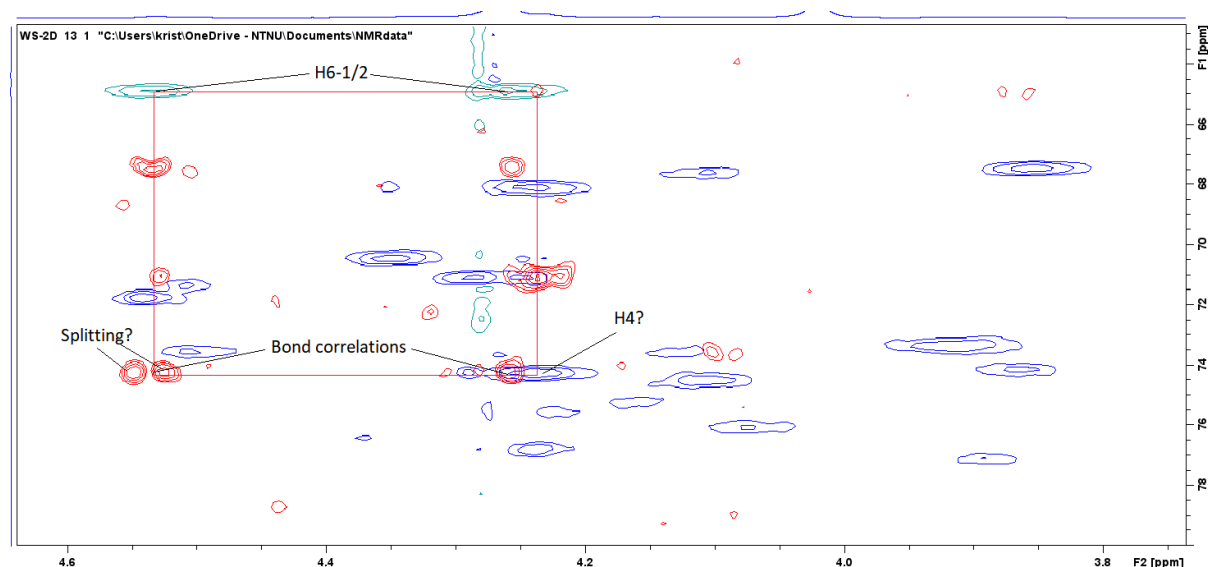
Figure D 5 HSQC + HMBC of WS where the assumed β-mannose H6 from Figure D 3 is correlated to an assumed β-mannose H5 or β-mannose H4 peak through a multiple bond correlation.

To verify whether the unidentified peak in Figure D 4 was the β-mannose H5- or the β-mannose H4-peak, a H2BC spectrum was searched for a correlation (Figure D 6). After finding a two-bond correlation between the β-mannose H6 and the peak thought to be either β-mannose H5 or β-mannose H4, it was very likely that it was the β-mannose H5-peak. The remaining peak correlating to the β-mannose H6 was by the process of elimination likely to be the β-mannose H4-peak, since the β-mannose H5-peak

had been assigned. However, the HMBC can sometimes even show three-bond correlations so further proof is required to confirm its identity.
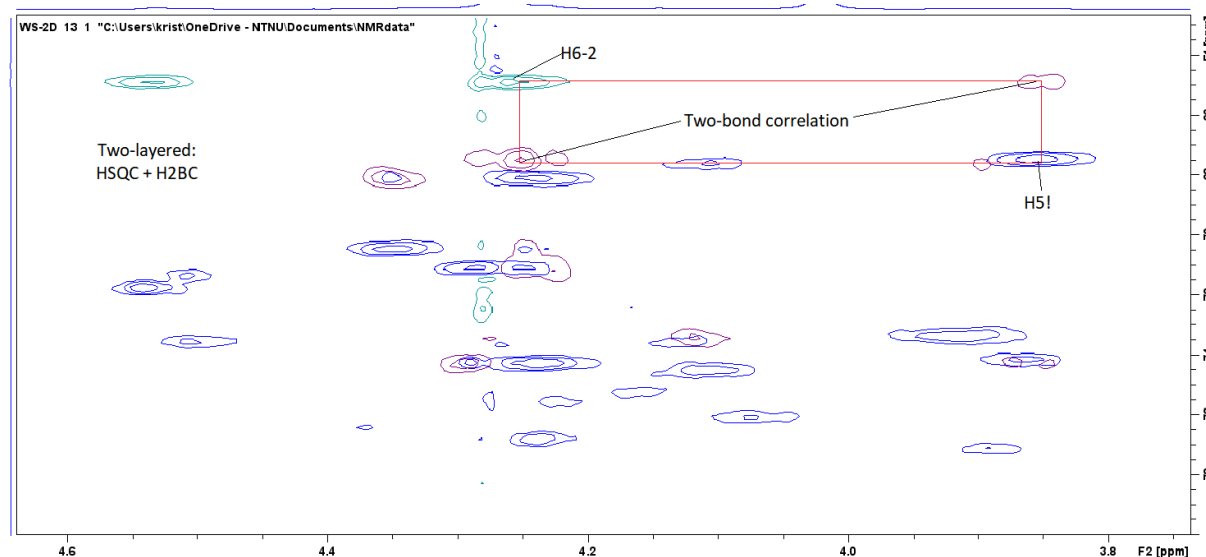
Figure D 6 HSQC + H2BC spectra where one of the assumed β-mannose H6 peaks correlates to the assumed β-mannose H5 and confirms that there is a two-bond correlation. Blue = HSQC CH/CH3 peaks, green = HSQC CH2 peaks and purple = H2BC peaks.

The assumed H4-peak was found to have a two-bond correlation with the now verified H5-peak from the H2BC-spectrum in Figure D 7, confirming that the potential H4-peak was most likely the H4-peak of the spin system.
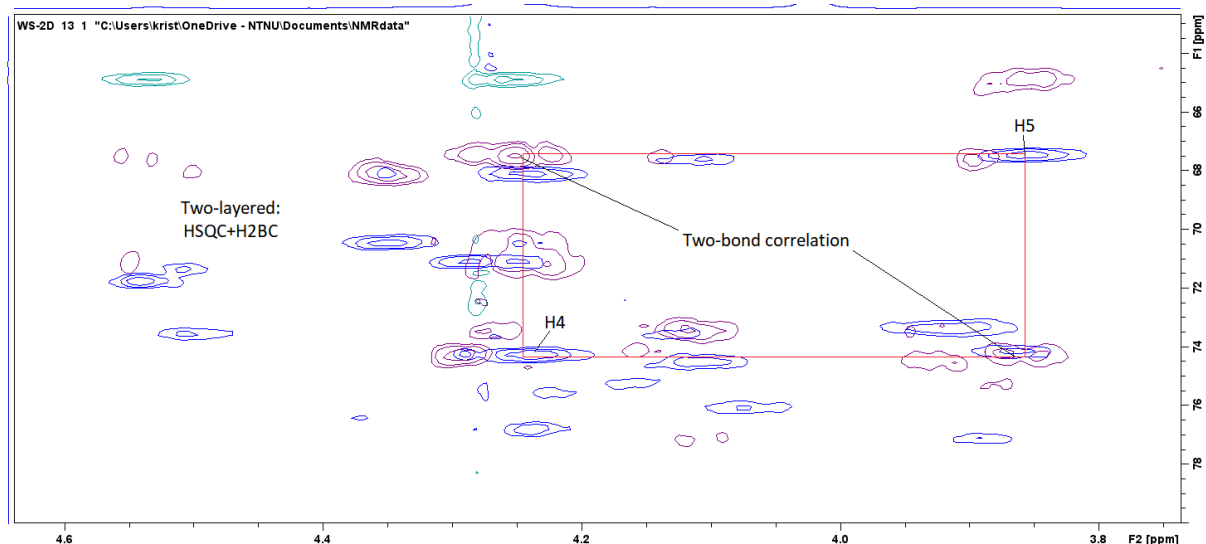
Figure D 7 HSQC + H2BC spectra where one of the assumed β-mannose H5 peaks correlates to the assumed H4 and confirms that there is a two-bond correlation between the two. Blue = HSQC CH/CH3 peaks, green = HSQC CH2 peaks and purple = H2BC peaks.

Further on, a new HMBC-correlation between the β-mannose H4 and a new peak was found in Figure D 8. This was confirmed to be the β-mannose H3-peak through a two-bond correlation with the previously confirmed β-mannose H4 by using the H2BC-spectrum in Figure D 9.
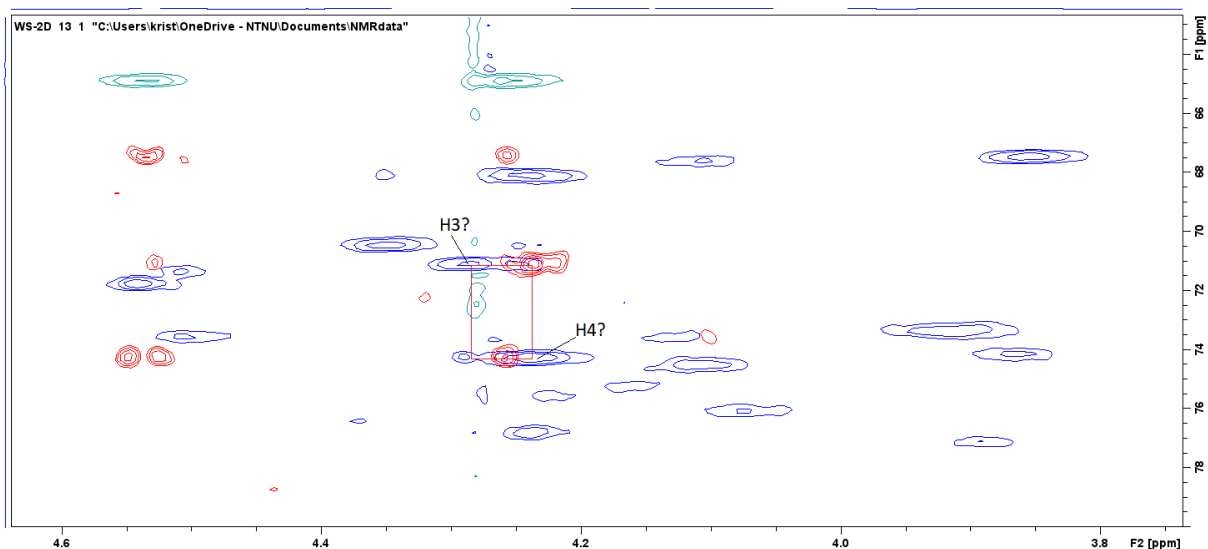
Figure D 8 HSQC + HMBC spectra of WS where confirmed β-mannose H4 peak correlates with a new unidentified peak suggested to be either β-mannose H3 or β-mannose H2. Blue = HSQC CH/CH3 peaks, green = HSQC CH2 peaks and purple = H2BC peaks.
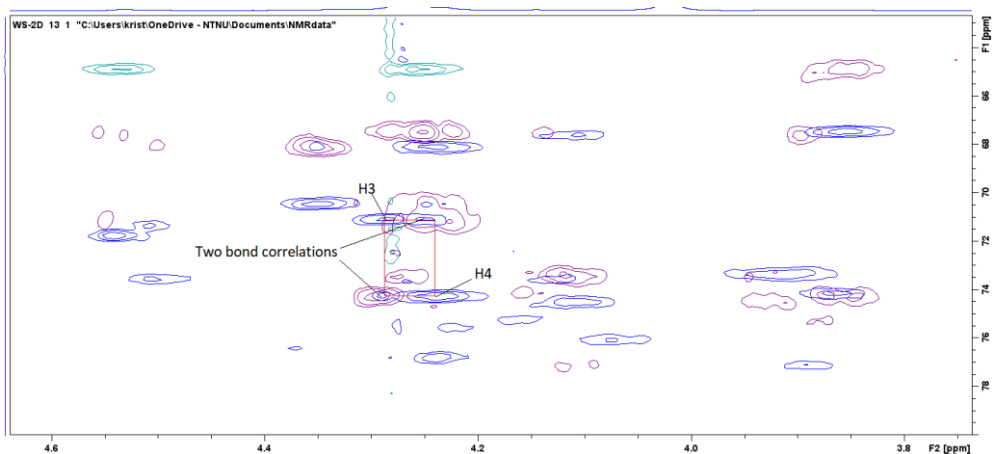
Figure D 9 HSQC + H2BC spectra of WS the β-mannose H4 peak correlates to the assumed β-mannose H3 and confirms its identity through a two-bond correlation. Blue = HSQC CH/CH3 peaks, green = HSQC CH2 peaks and purple = H2BC peaks.

The β-mannose H3-peak seemed to have an HMBC-correlation to a new peak as seen in Figure D 10, before this was further confirmed to be the β-mannose H2-peak using the H2BC-spectrum in Figure D

11. This new peak however seemed to be two overlapping peaks and was thought to be a result of having both acetylated and non-acetylated H2-protons at the β-mannose position.
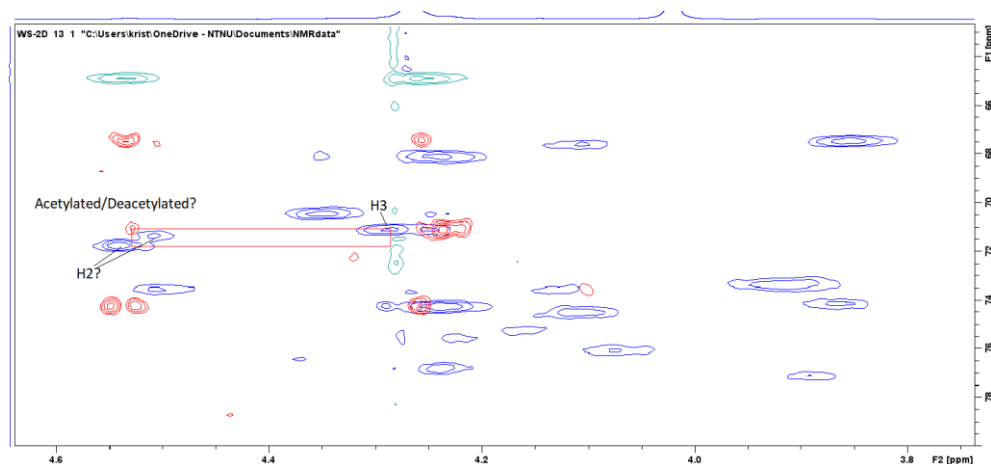
Figure D 10 HSQC + HMBC spectra of WS where the confirmed β-mannose H3 peak correlates with a new unidentified peak suggested to be β-mannose H2. Blue = HSQC CH/CH3 peaks, green = HSQC CH2 peaks and purple = H2BC peaks.
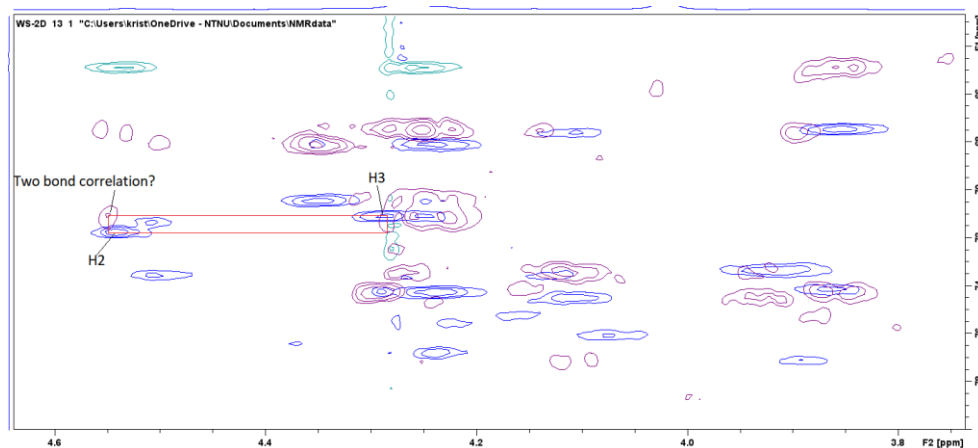
Figure D 11 HSQC + H2BC spectra of WS where the β-mannose H3 peak correlates to the assumed H3 and confirms its identity through a two-bond correlation. Blue = HSQC CH/CH3 peaks, green = HSQC CH2 peaks and purple = H2BC peaks.

From the β-mannose H2-peak, a final HMBC correlation was found and would most likely be a correlation to the anomeric proton, or β-mannose H1-peak as seen in Figure D 12.
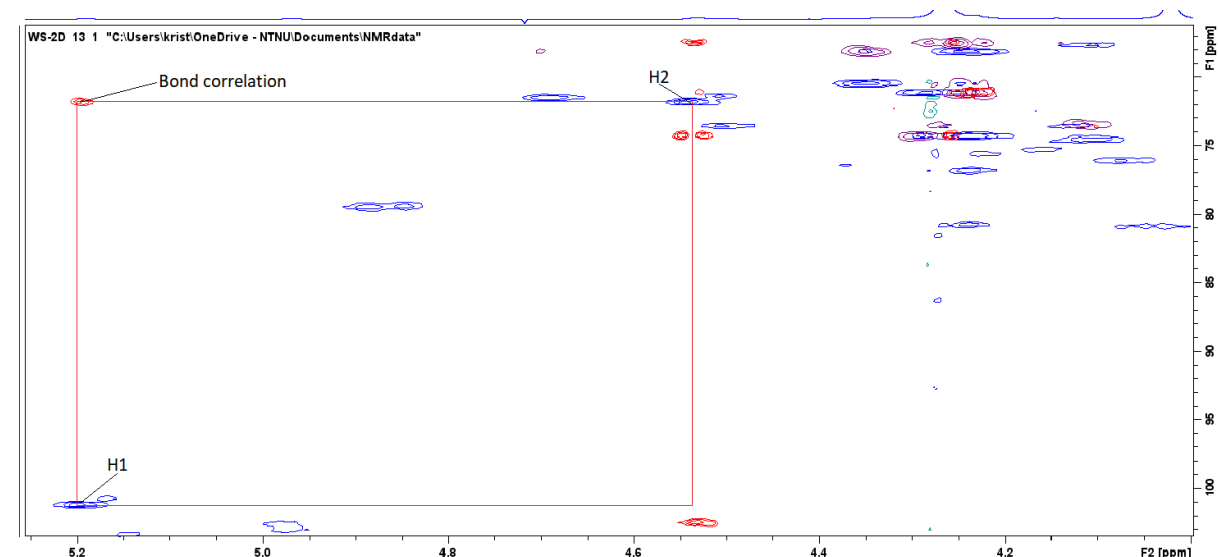
Figure D 12 HSQC + HMBC spectra of WS where the confirmed β-mannose H2 peak correlates with a new unidentified peak suggested to be β-mannose H1. Blue = HSQC CH/CH3 peaks, green = HSQC CH2 peaks and purple = H2BC peaks.

To conclude the assigning of the first spin system, all the peaks were annotated in an HSQC-spectrum in Figure D 13
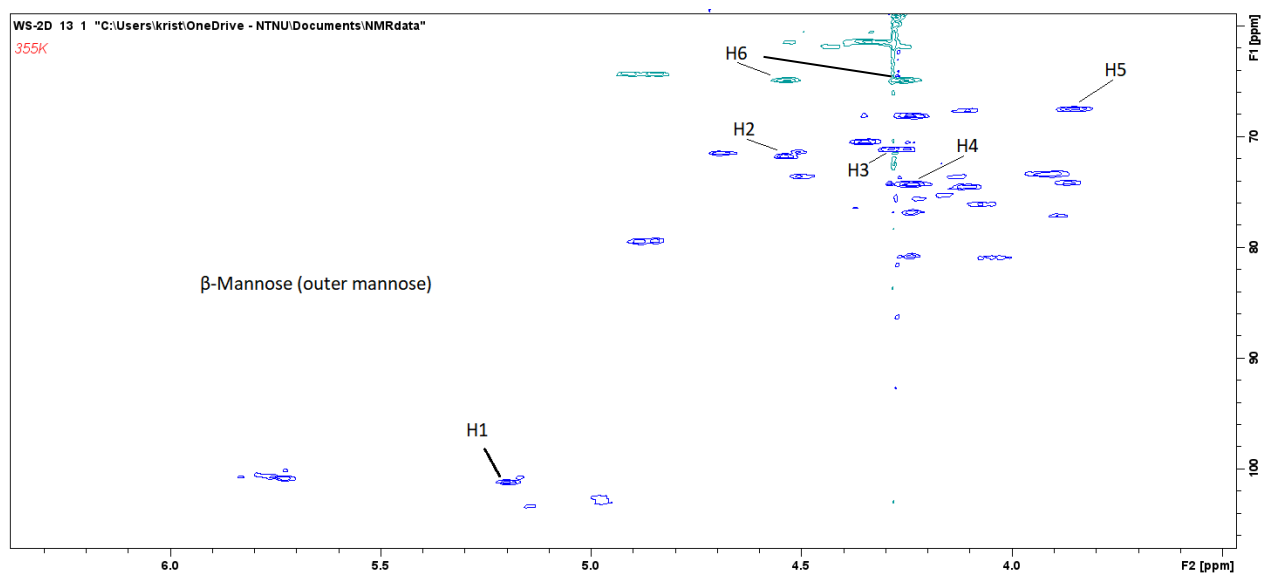
Figure D 13 HSQC-spectrum of WS with the β-mannose peaks assigned and annotated. Blue = HSQC CH/CH3 peaks and green = HSQC CH2 peaks.

E. ¹H-NMR spectra

¹H-NMR spectra of all the samples in the temperature range 298, 313-363 K stacked in a region of interest (anomeric region, approx. 6.0-4.7 δ-¹H ppm). For all figures, the left-most peak is the anomeric proton of the α-mannose which was chosen as the reporter signal.
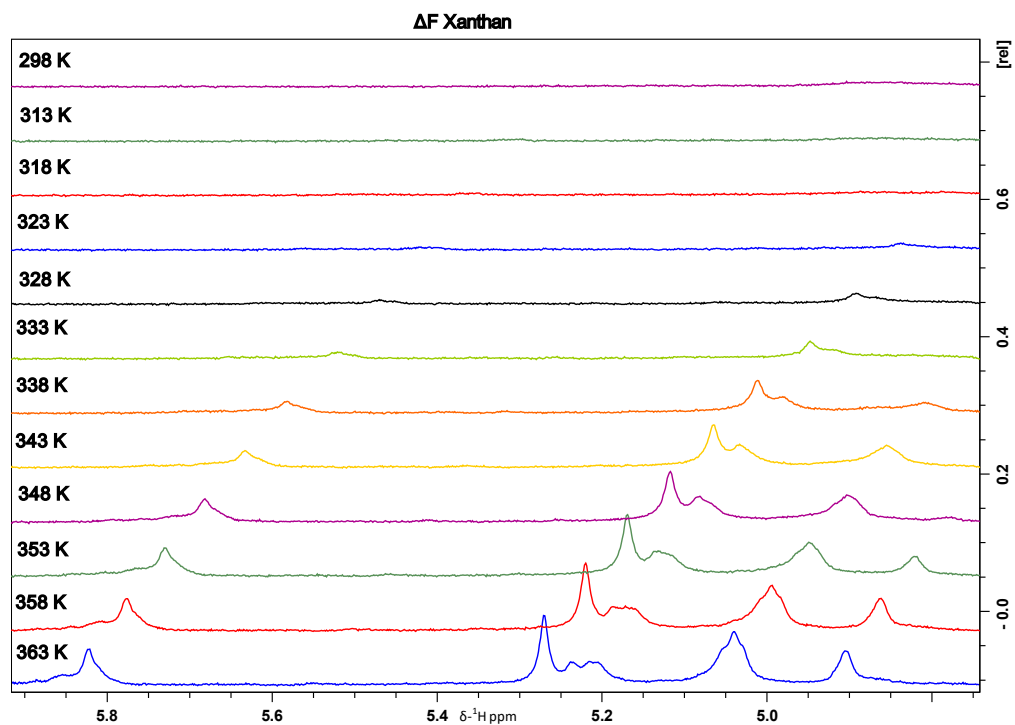
Figure E 1 Stacked view of the anomeric region (6.0-4.7 δ-¹H ppm) ¹H-NMR spectra of ΔF in a range of temperatures (298 K, 313-363 K).
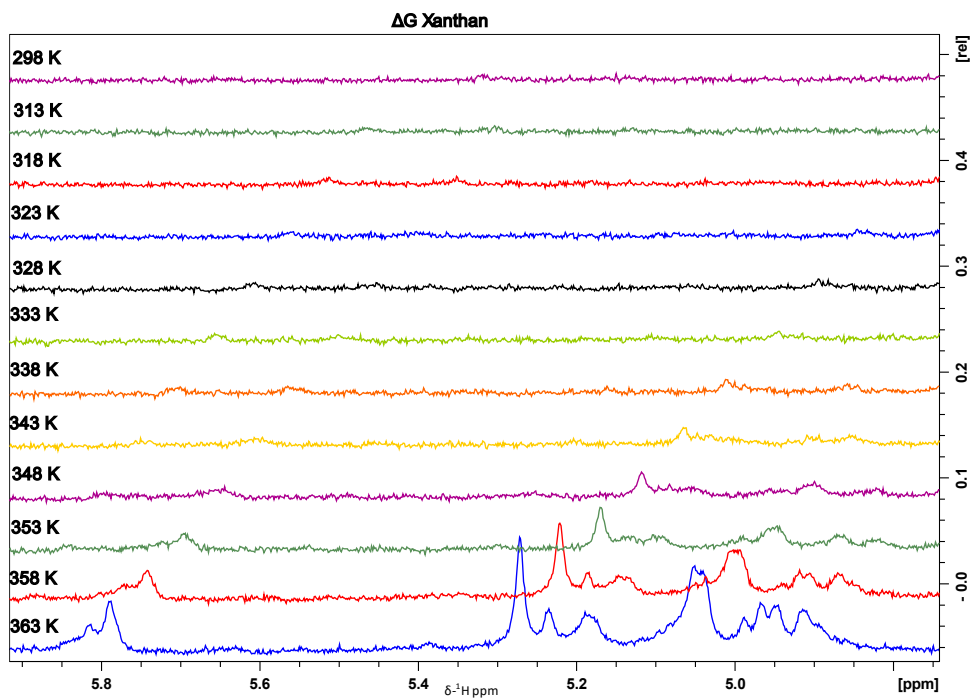
Figure E 2 Stacked view of the anomeric region (6.0-4.7 δ-^{1}H ppm) ^{1}H-NMR spectra of ΔG in a range of temperatures (298 K, 313-363 K).
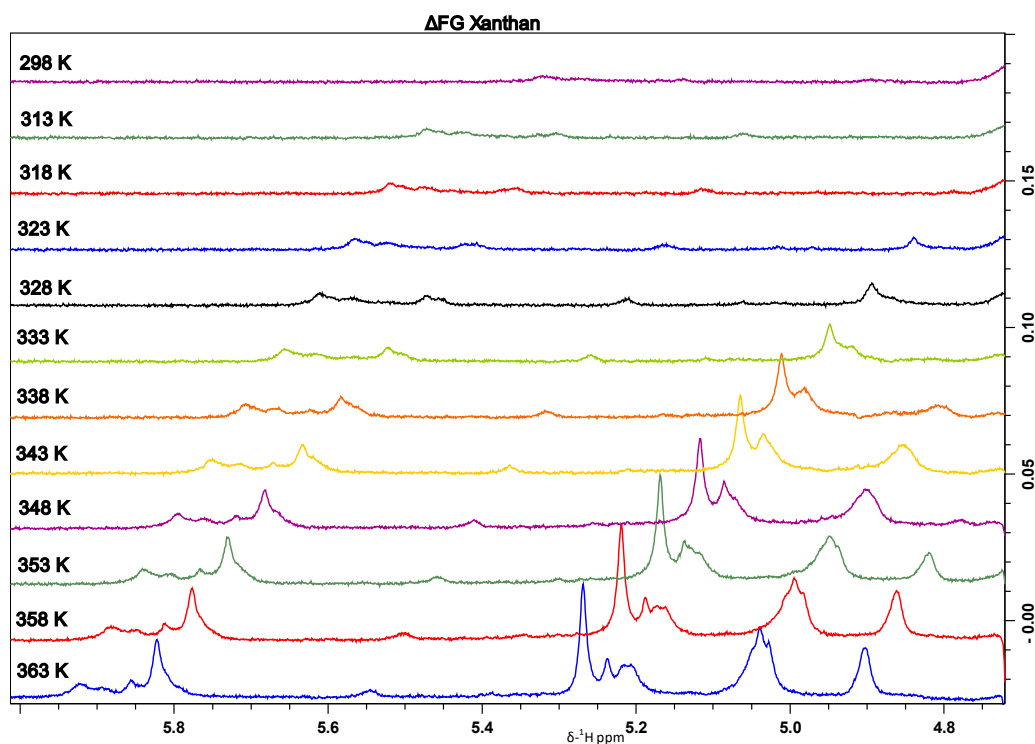
Figure E 3 Stacked view of the anomeric region (6.0-4.7 δ-^{1}H ppm) ^{1}H-NMR spectra of ΔFG in a range of temperatures (298 K, 313-363 K).
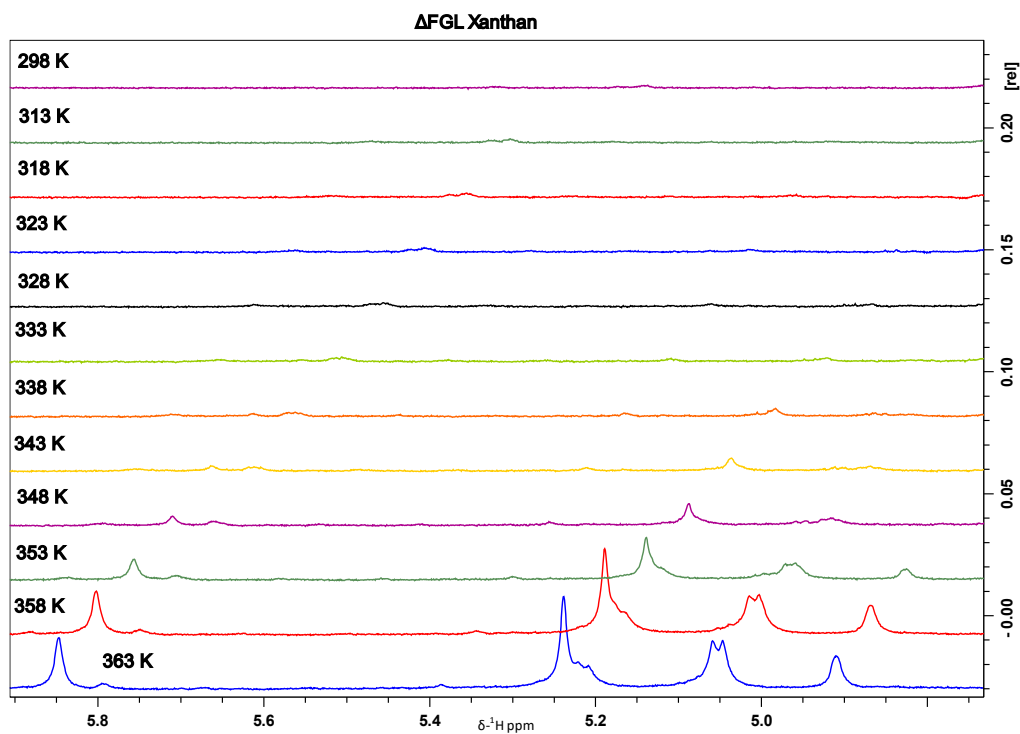
Figure E 4 Stacked view of the anomeric region (6.0-4.7 δ-¹H ppm) ¹H-NMR spectra of ΔFGL in a range of temperatures (298 K, 313-363 K).
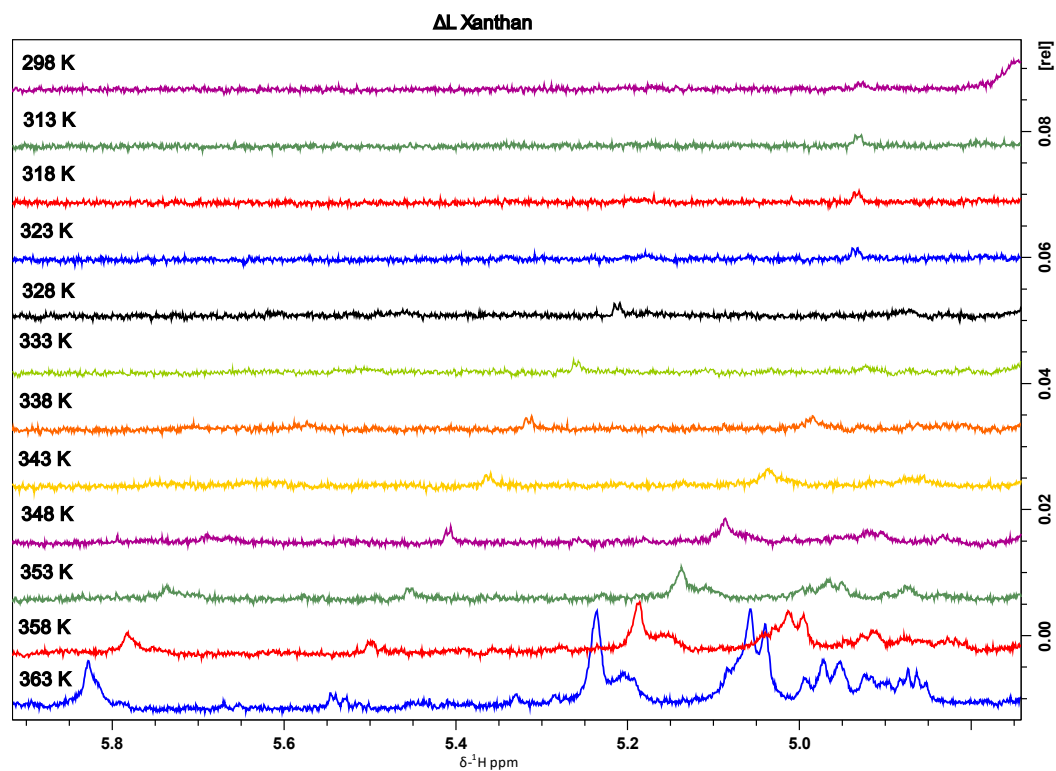
Figure E 5 Stacked view of the anomeric region (6.0-4.7 δ-¹H ppm) ¹H-NMR spectra of ΔL in a range of temperatures (298 K, 313-363 K).
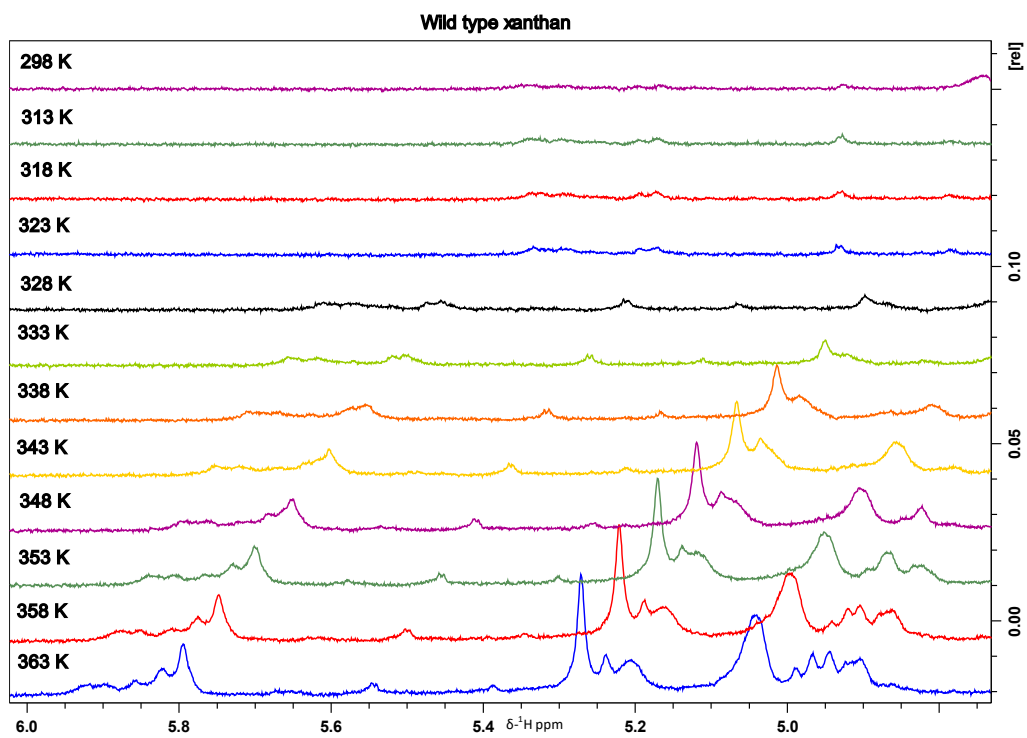
Figure E 6 Stacked view of the anomeric region (6.0-4.7 δ-^{1}H ppm) ^{1}H-NMR spectra of wild type in a range of temperatures (298 K, 313-363 K).

F. 2D spectra

2D-NMR spectra of all samples (HSQC, HMBC and H2BC) as described in chapter 4.2.4.
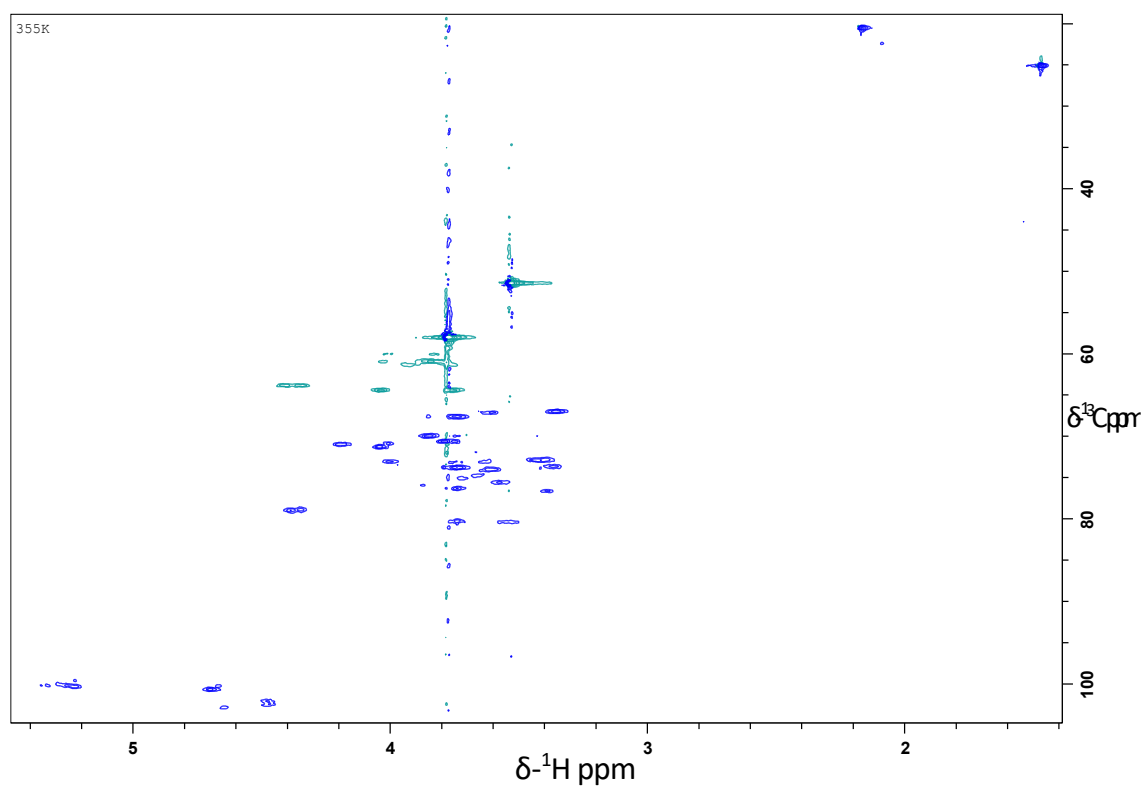
Figure F 1 HSQC spectrum (355 K) of the wild type zoomed into a region of interest (5.4-1.3 δ-¹H ppm, 23.3-108.2 δ-13C ppm). Blue peaks are CH and CH3 and green peaks are CH2.
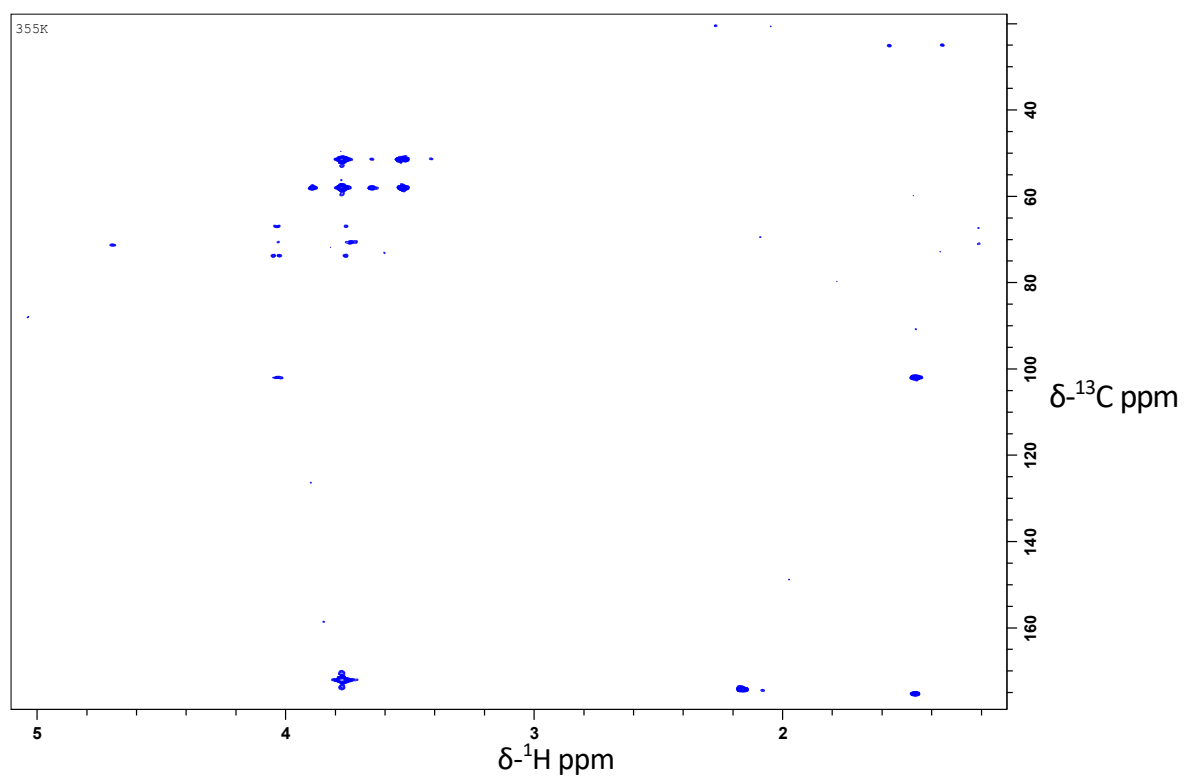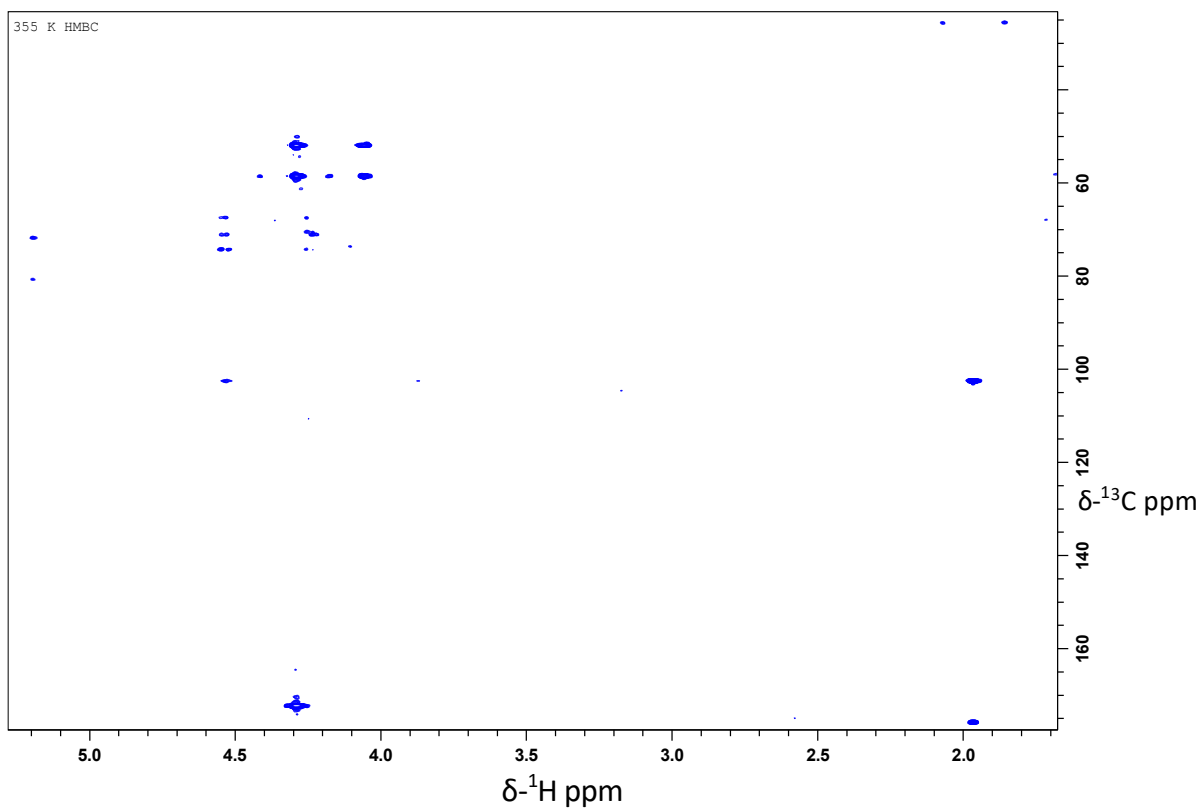
Figure F 2 HMBC spectrum (355 K) of the wildtype zoomed into a region of interest (approx. 5.4-1.3 δ-^{1}H ppm, 23.3-108.2 δ-13C ppm).
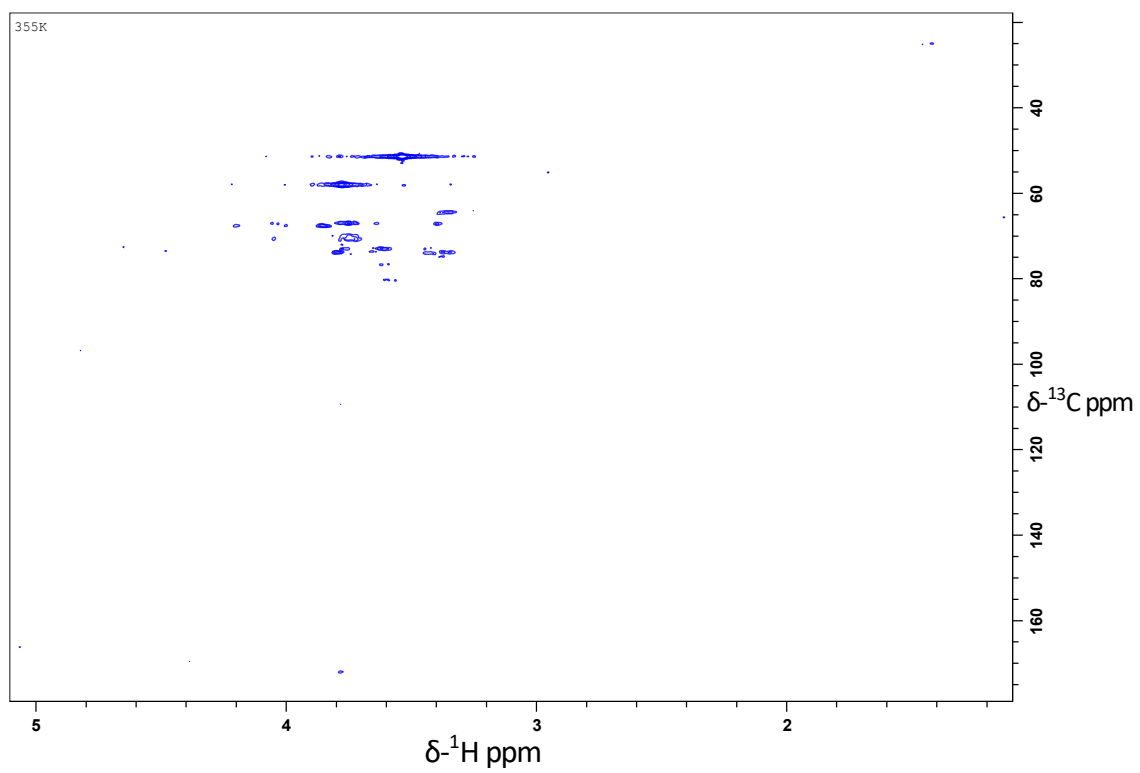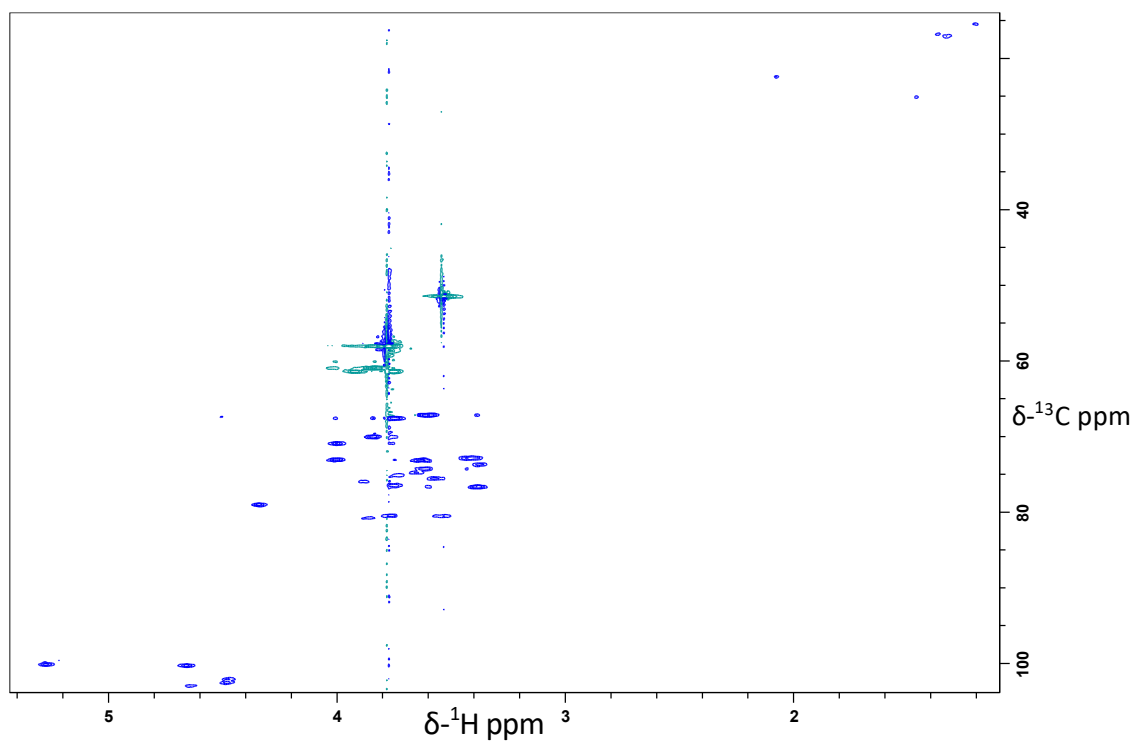
Figure F 3 H2BC spectrum (355 K) of the ΔG zoomed into a region of interest (approx. 5.4-1.3 δ-¹H ppm, 23.3-108.2 δ-13C ppm).
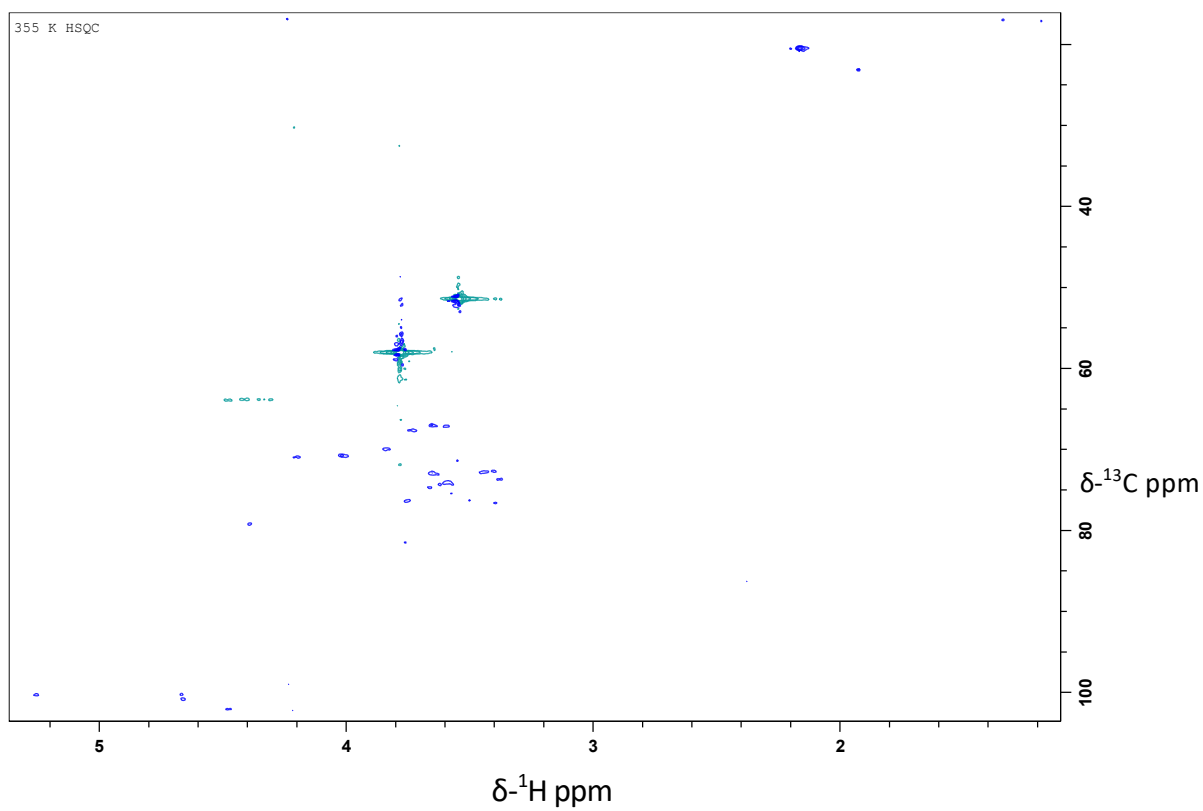
Figure F 4 HSQC spectrum (355 K) of the ΔL zoomed into a region of interest (approx. 5.4-1.3 δ-¹H ppm, 23.3-108.2 δ-13C ppm). Blue peaks are CH and CH3 and green peaks are CH2.
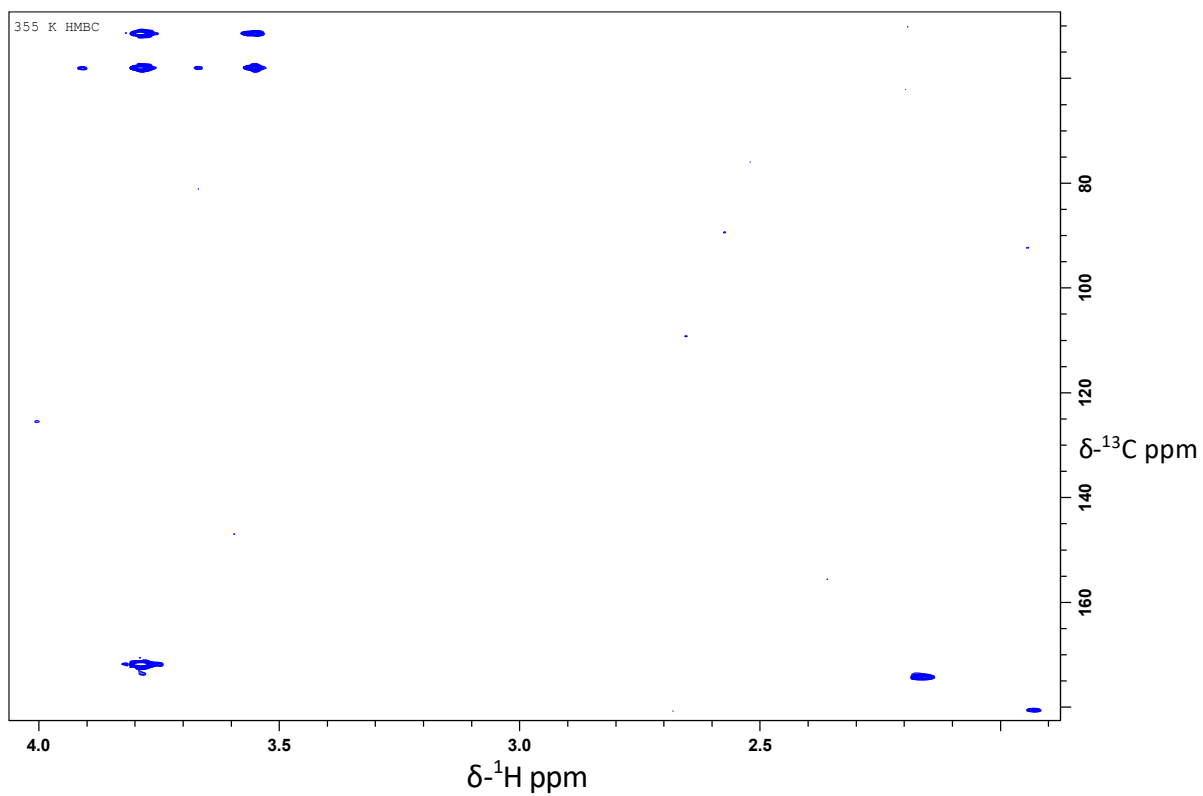
Figure F 5 HMBC spectrum (355 K) of the ΔL zoomed into a region of interest (approx. 5.4-1.3 δ-¹H ppm, 23.3-108.2 δ-13C ppm).
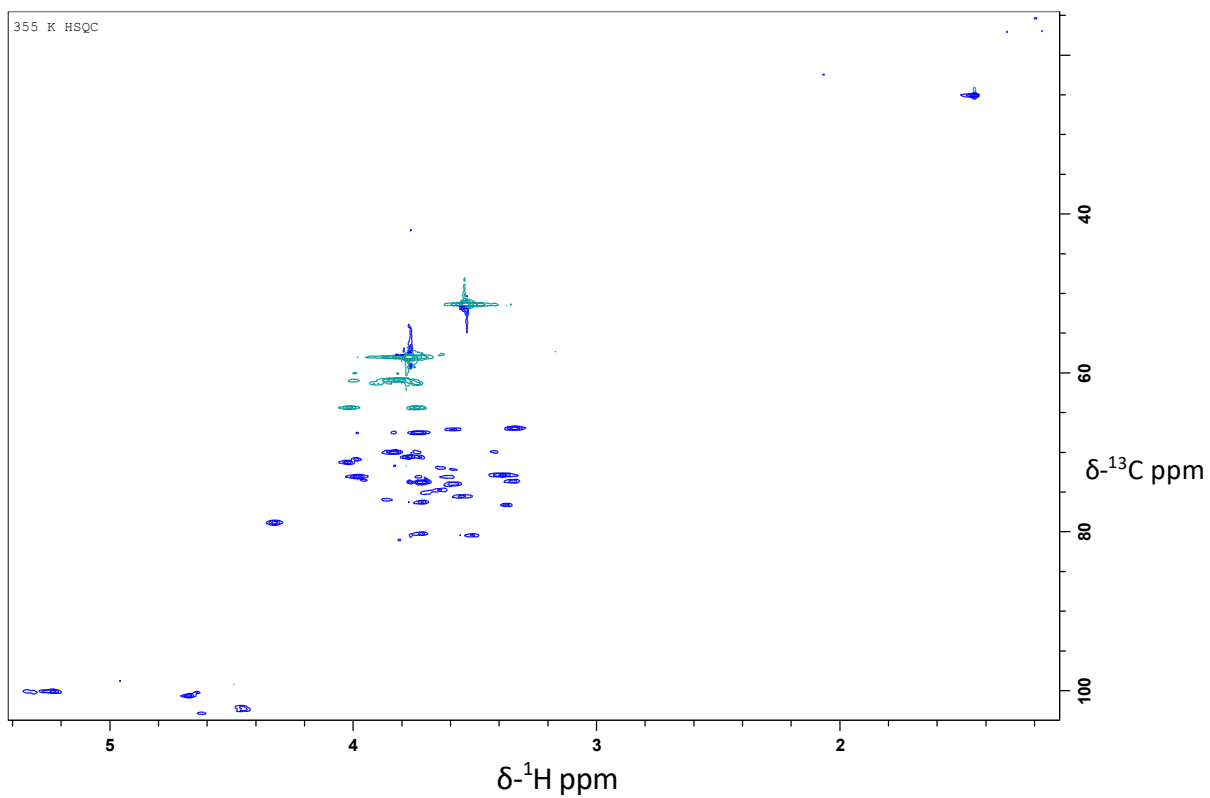
Figure F 6 HSQC spectrum (355 K) of the ΔFG zoomed into a region of interest (approx. 5.4-1.3 δ-^{1}H ppm, 23.3-108.2 δ-13C ppm). Blue peaks are CH and CH3 and green peaks are CH2.

Figure F 7 HMBC spectrum (355 K) of the ΔFG zoomed into a region of interest (approx. 5.4-1.3 δ-¹H ppm, 23.3-108.2 δ-¹³C ppm).

Figure F 8 HSQC spectrum (355 K) of the ΔFGL zoomed into a region of interest (approx. 5.4-1.3 δ-^{1}H ppm, 23.3-108.2 δ-^{13}C ppm). Blue peaks are CH and CH3 and green peaks are CH2.
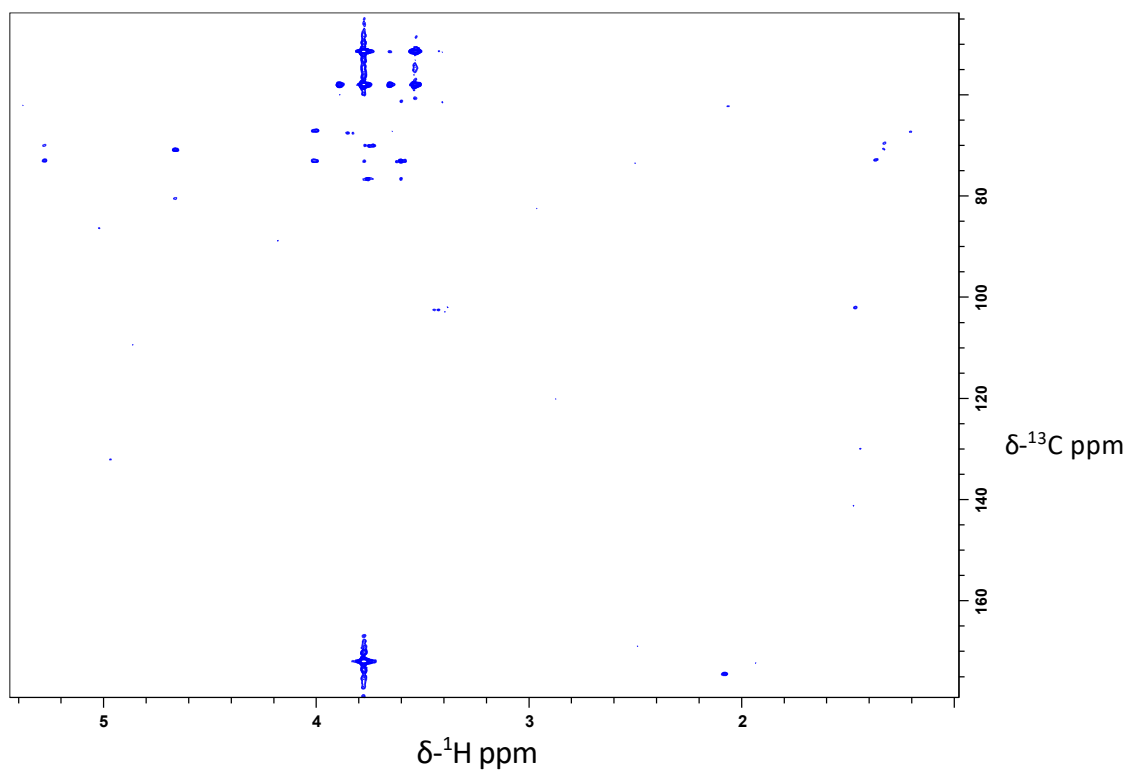
Figure F 9 HMBC spectrum (355 K) of the ΔFGL zoomed into a region of interest (approx. 5.4-1.3 δ-¹H ppm, 23.3-108.2 δ-¹³C ppm).
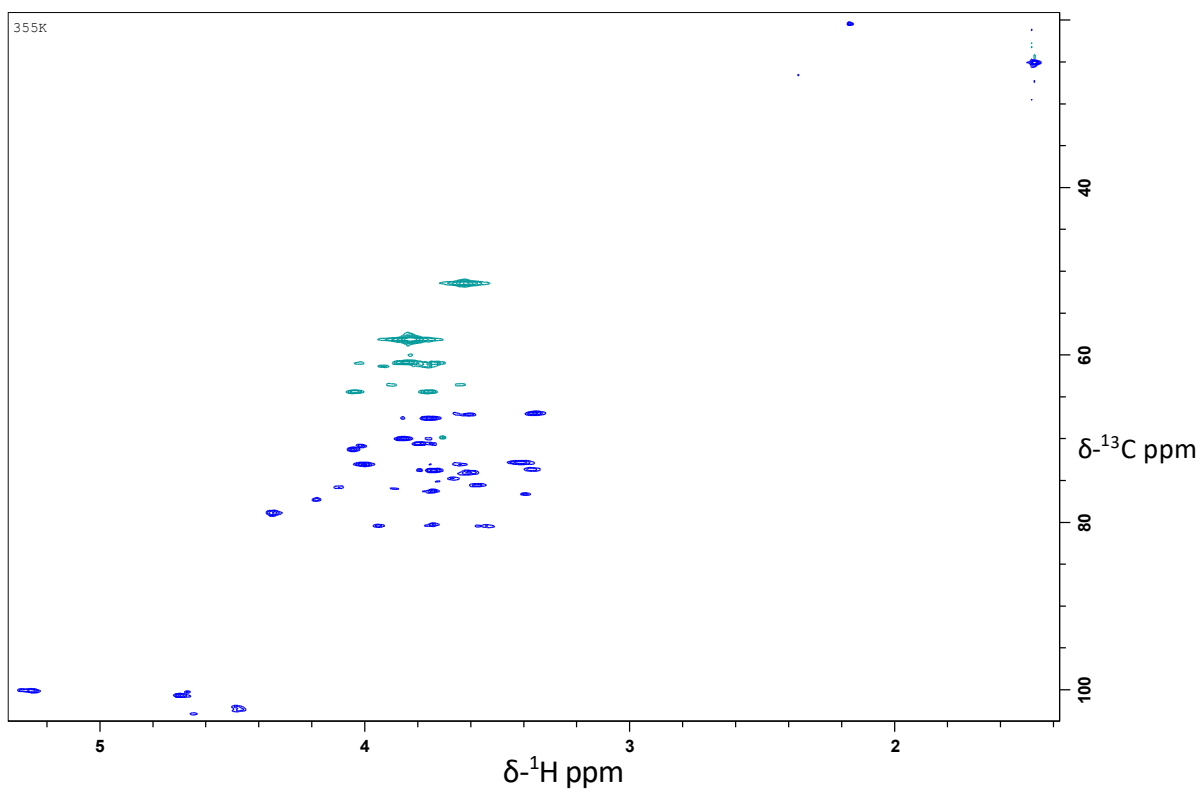
Figure F 10 HSQC spectrum (355 K) of the ΔF zoomed into a region of interest (approx. 5.4-1.3 δ-^{1}H ppm, 23.3-108.2 δ-^{13}C ppm). Blue peaks are CH and CH3 and green peaks are CH2.
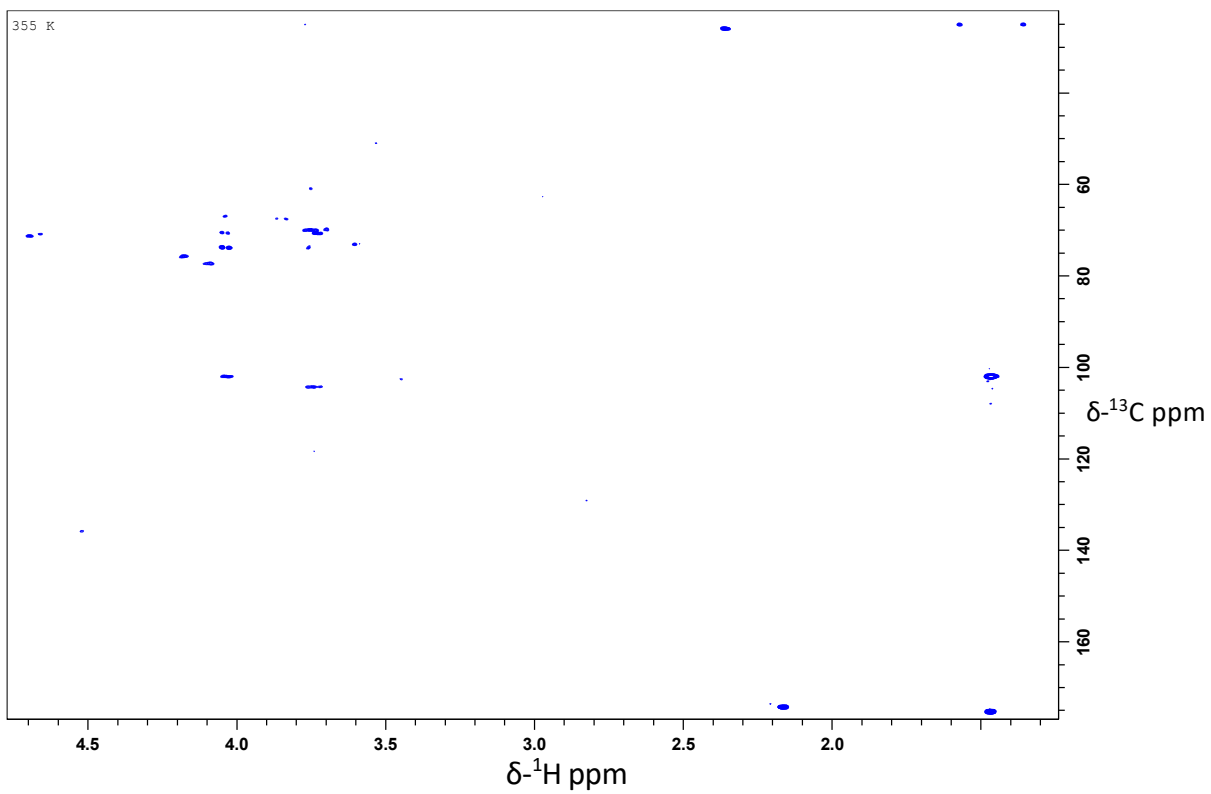
Figure F 11 HMBC spectrum (355 K) of the ΔF zoomed into a region of interest (approx. 5.4-1.3 δ-^{1}H ppm, 23.3-108.2 δ-^{13}C ppm).
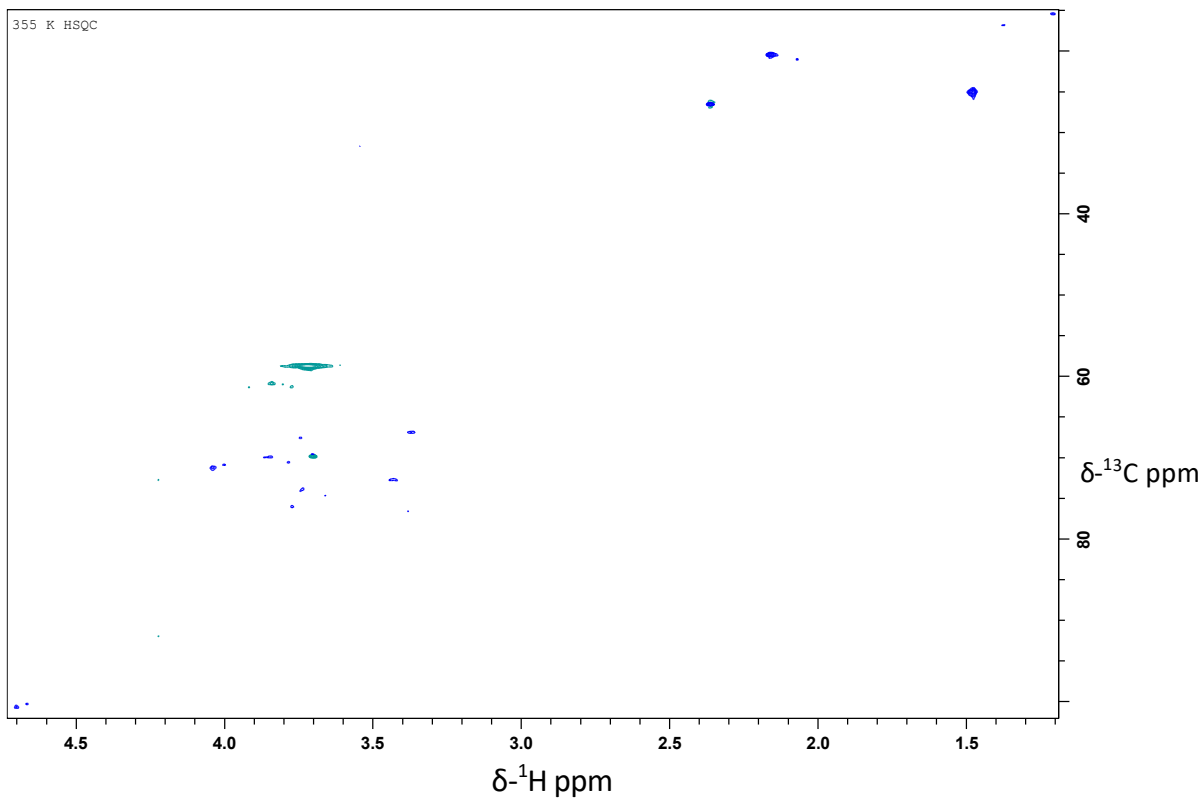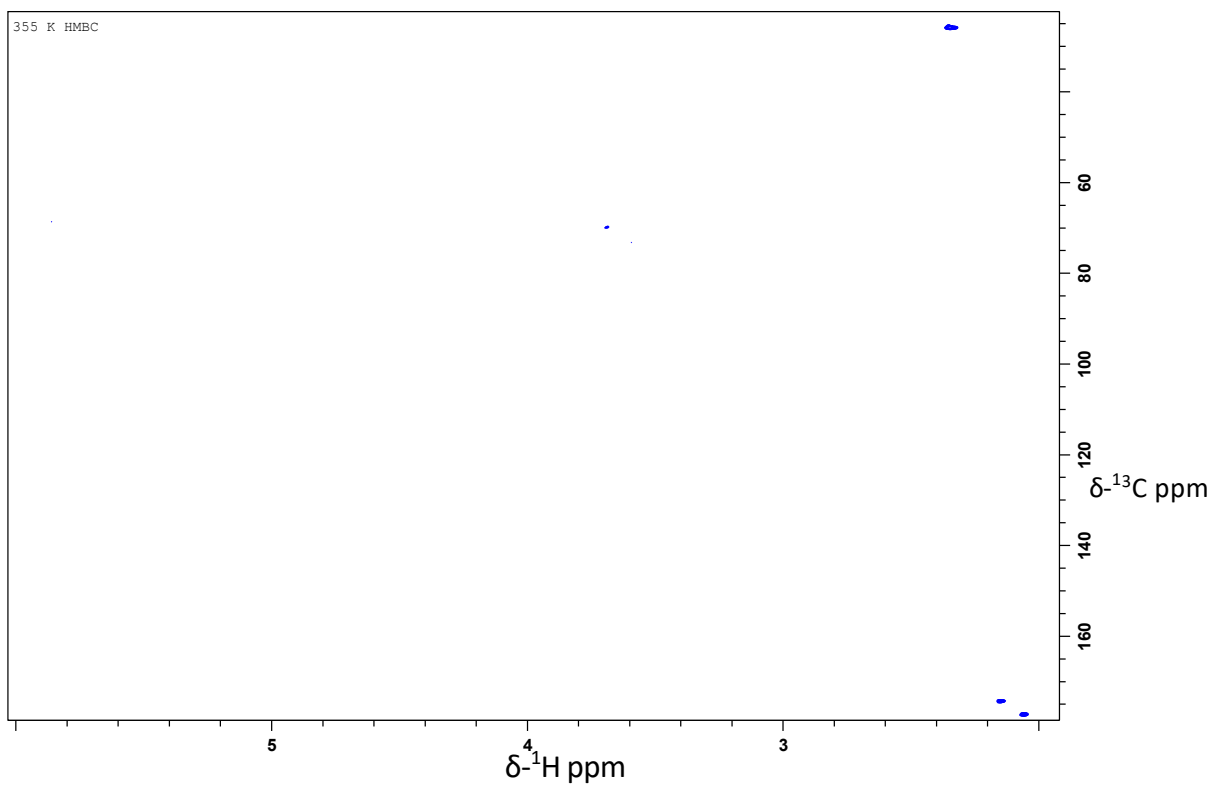
Figure F 12 HSQC spectrum (355 K) of the ΔG zoomed into a region of interest (approx. 5.4-1.3 δ-^{1}H ppm, 23.3-108.2 δ-^{13}C ppm). Blue peaks are CH and CH3 and green peaks are CH2.

Figure F 13 HMBC spectrum (355 K) of the ΔG zoomed into a region of interest (approx. 5.4-1.3 δ-^{1}H ppm, 23.3-108.2 δ-^{13}C ppm).
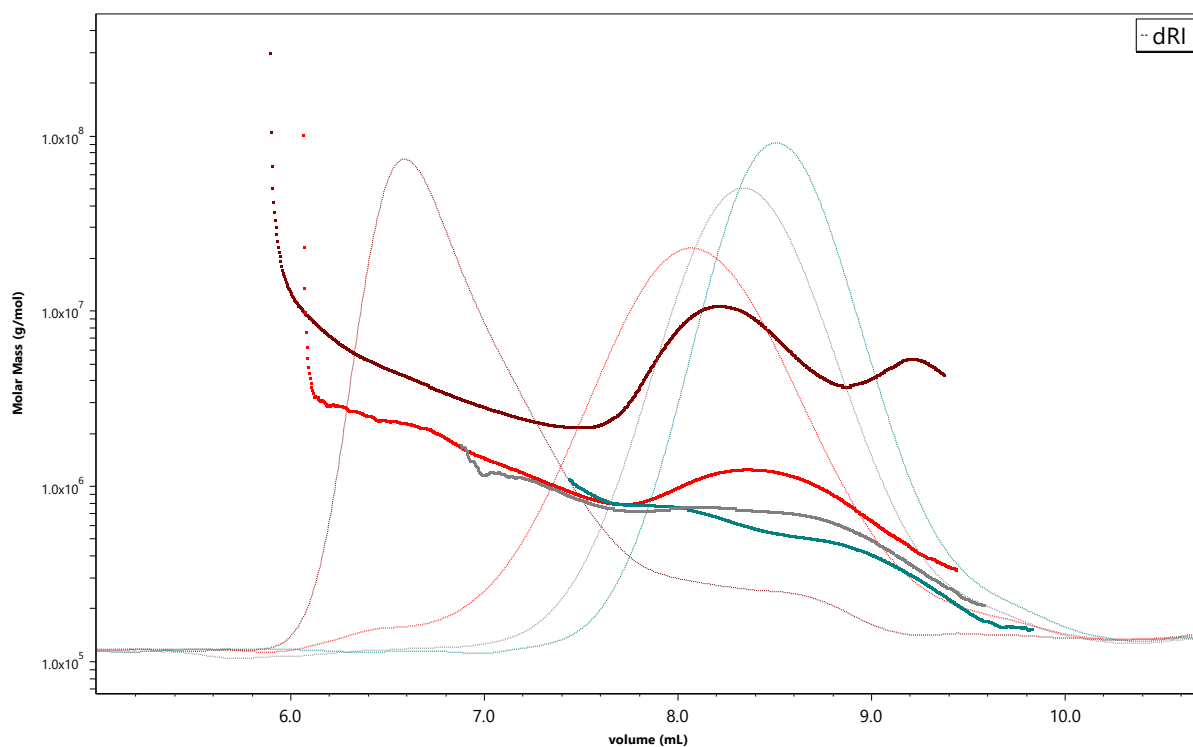
G. SEC-MALS data

Figure G 1 Molar mass distribution and refractive index changes for wildtype as a function of elution volume for zero (brown), two (red), five (grey) and ten (green) cycles in the StarBurst homogenizer. The dashed line is the differential refractive index displaying the weight distribution becoming progressively narrower and moved to a higher elution volume. The denser dashed lines with greater line widths display the calculated weight-average molecular weight getting progressively lower and less disperse.
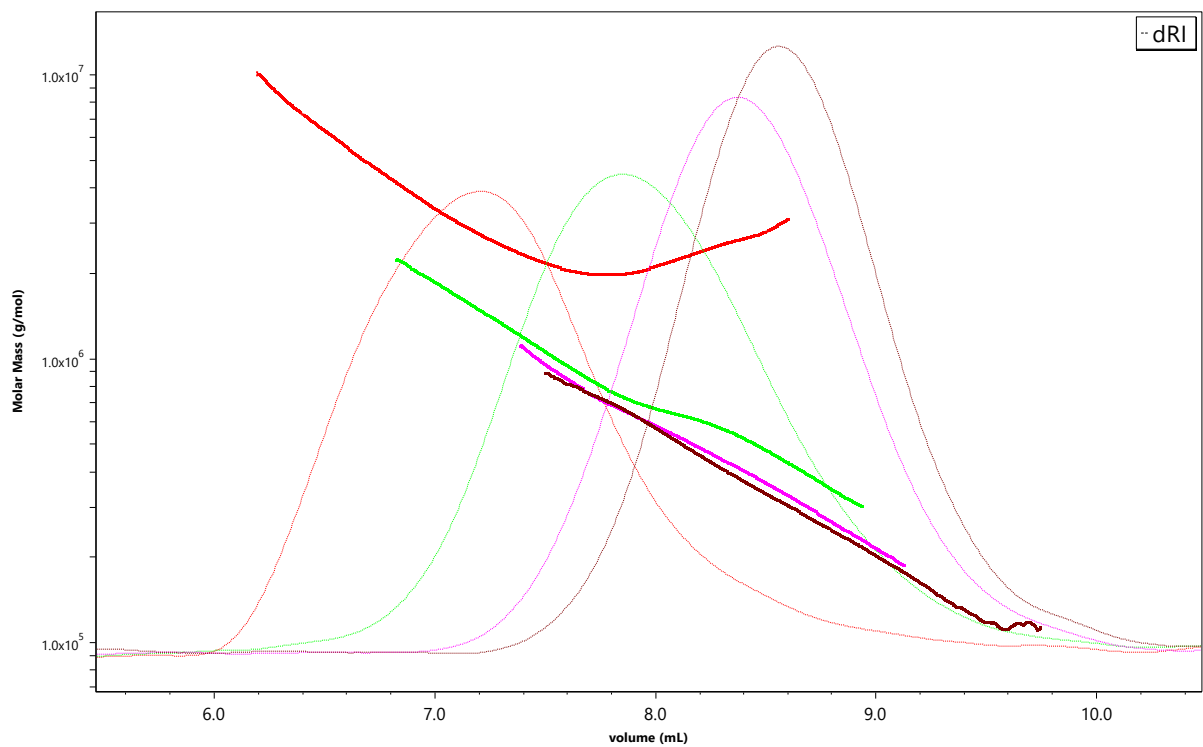
Figure G 2 Molar mass distribution and refractive index changes for ΔL as a function of elution volume for zero (red), one (green), five (purple) and ten (black) cycles in the StarBurst homogenizer. The dashed line is the differential refractive index displaying the weight distribution becoming progressively narrower and moved to a higher elution volume. The denser dashed lines with greater line widths display the calculated weight-average molecular weight getting progressively lower and less disperse.
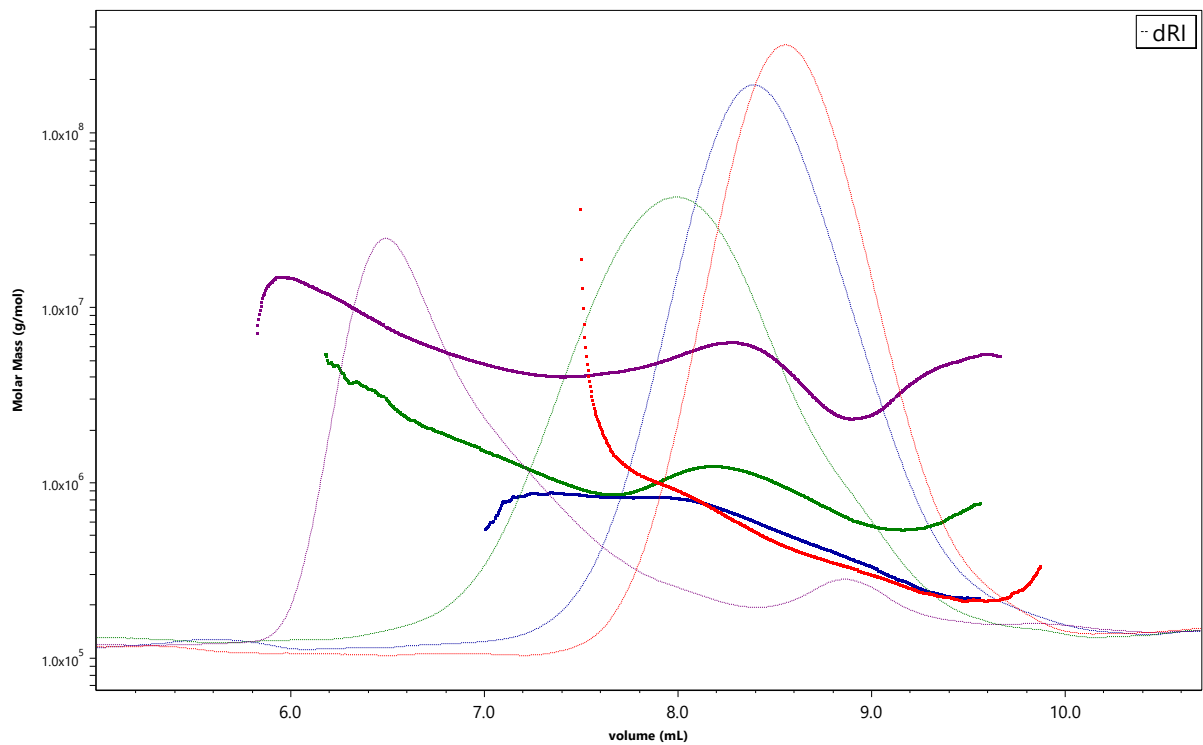
Figure G 3 Molar mass distribution and refractive index changes for ΔFGL as a function of elution volume for zero (purple), one (green), five (blue) and ten (red) cycles in the StarBurst homogenizer. The dashed line is the differential refractive index displaying the weight distribution becoming progressively narrower and moved to a higher elution volume. The denser dashed lines with greater line widths display the calculated weight-average molecular weight getting progressively lower and less disperse.
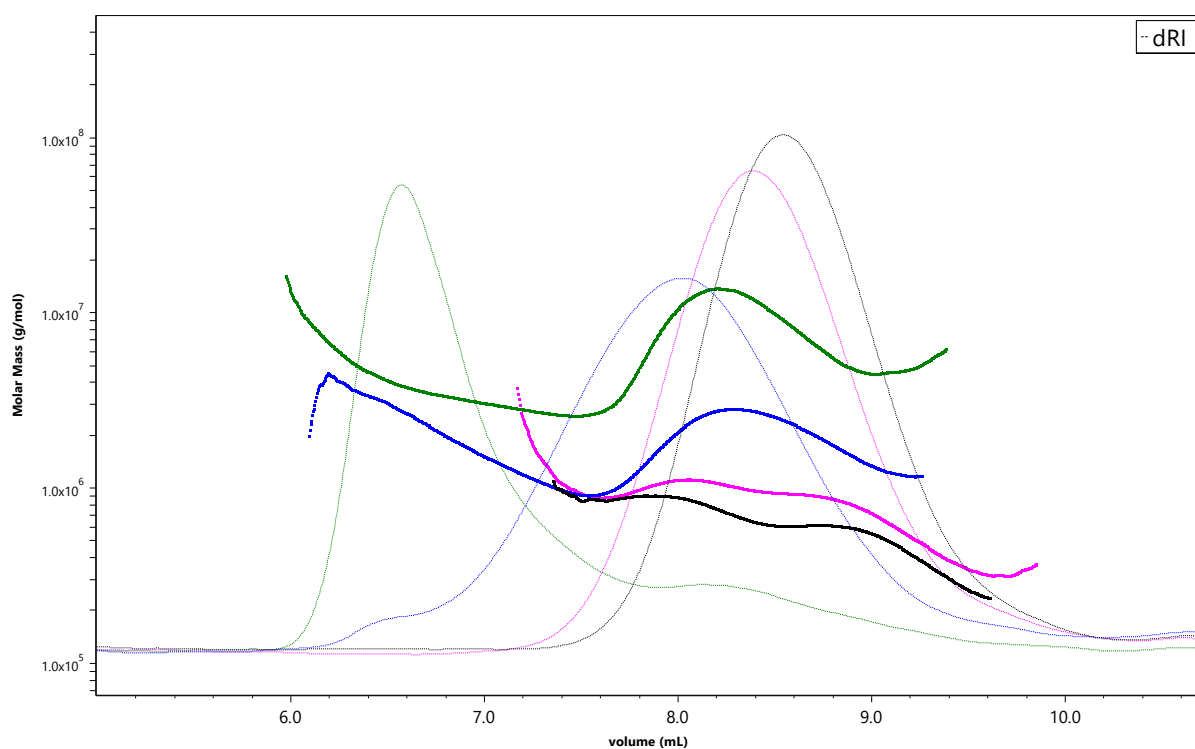
Figure G 4 Molar mass distribution and refractive index changes for ΔL as a function of elution volume for zero (green), one (blue), five (pink) and ten (black) cycles in the StarBurst homogenizer. The dashed line is the differential refractive index displaying the weight distribution becoming progressively narrower and moved to a higher elution volume. The denser dashed lines with greater line widths display the calculated weight-average molecular weight getting progressively lower and less disperse.

H. Contamination experiment

Table H 1 SEC-MALS result from the contamination experiment described in chapter 4.2.2.2

	Mn (kDa)	±	M_w (kDa)	±	Polydispersity (M_w/Mn)	R_w (nm)	±	Calculated mass (µg)
Wild type A.C. (Nine cycles)	487.6	0.3%	496.7	0.4%	1.019	55.9	1.5%	4.76
Wild type (Nine cycles)	382.6	0.6%	431.3	0.4%	1.127	50.2	1.8%	14.47

I. Standard operation procedure for fermentation

SOP FOR FERMENTATION (2L BIOSTAT)

created by Julia Wünsche
last edited 09.02.2021

Day prior to fermentation (before autoclaving)

- □ check, if fermenter is clean and rebuilt
- □ prepare, dissolve and transfer media compounds to the fermenter (do not forget supplementary, but autoclave them separately)
- □ start cooling water system
- □ refill vessel coat
    - ⬚ wait for all bubbles to be removed, check system for leakages
    - ⬚ connect temperature sensor
    - ⬚ conduct pH-calibration (external, RT)
    - ⬚ install pH probe
- □ install DO sensor
- □ prepare fermenter for autoclaving (disconnect connection from the cooling water system to the fermenter **before** you move the fermenter; install clamps, aluminum foil and black safety caps for electrodes, close open tubes; check if all components are fixed properly/tight)
- □ prepare and refill 7 % H_3PO_4 (acid), 2 M NaOH (base) and 1 % anti-foam (+ feed)
- □ prepare overflow bottle and a bottle for supplementary (empty)
- □ start autoclaving process (fermenter, overflow bottle, bottle for supplementary, acid, base, anti-foam, additional media compounds)
- □ start documentation sheet
- □ last chance to start your pre-culture (50 mL)

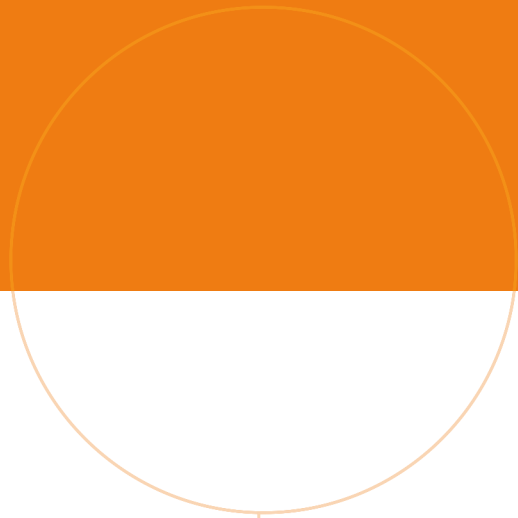### Day prior to fermentation (after autoclaving)

- □ remove aluminum foil from filters
- □ wait until fermenter is cooled down to room temperature
- □ re-connect water cooling system, all sensors, stirrer (check if tightly fixed!), tubes for acid, base, anti-foam (place them in the pumps first))

Start of fermentation

- □ start airflow (1.5 L/min) and connect overflow bottle
- □ start heating (30 °C)
- □ conduct supplementation (use external pump)
- □ set stirrer and gassing parameters to 100 % (600 rpm, 1.5 L/min)
- □ set pumps to auto and start pH regulation (pH 6.8)
- □ wait for final temperature and pH values
    - ▯ start DO calibration
    - ▯ set DO calibration to working parameters (30 %)
- □ reset acid, base and anti-foam values
- □ start anti-foam control
- □ start process documentation (computer)
- □ transfer pre-culture (wait 30 min for first sampling)

- □ check parameters regularly during the fermentation process

End of fermentation

- □ switch off tower, water cooling system, air
- □ disconnect all tubes and sensors
- □ remove pH probes and OD sensors (install black safety caps, autoclave separately)
- □ transfer fermentation broth to a new bucket
- □ refill fermenter with dH_2O (equivalent volume to fermentation broth)
- □ install clamps, cover filters with aluminum foil and close open tubes
- □ start autoclaving process (fermenter, overflow bottle, all buckets with contact to biomass)
- □ discard base

2